Colloidal Quantum Dots Photovoltaics with Low-Dimensional Carbon Nanomaterials



Yujiro Tazawa
St Catherine's College
University of Oxford

A thesis submitted for the degree of
Doctor of Philosophy

Michaelmas 2018

This thesis is dedicated to

my father and my mother

for seeing me regardless of where he is now,

and for raising me with a lot of care and support.

Acknowledgements

I would like to thank Dr. Andrew Watt for his supervision and his encouragement in my journey to pursue the degree of Doctor of Philosophy. He guided me when I lost the direction of my career and also of my research projects.

I am also grateful to Dr. Hazel Assender, Dr. Robin Nicholas, Dr. Moritz Riede, Dr. Lazaro Padilha, Dr. Severin Habisreutinger, Dr. Yuewen Sheng, Mr. Gabriel Nagamine, Ms. Qianyang Zhang for their dedication to our collaborative research projects. Without their advice or help, I could not proceed with my projects.

I would like to thank Dr. Assia Kasdi, Dr. Darren Chi Jin Neo, Dr. Inji Yeom, and Dr. Nina Klein for their encouragement and guidance of my research and my career. Inside and outside of the laboratory, Dr. Nanlin Zhang, Dr. Zhanet Zaharieva, and Mr. Wing Chung Liu have been great friends with their support and some exchange of ideas. I am grateful to Mr. Richard Turner for organizing the laboratory at best. I thank Mr. Daniel Gregory, Ms. Isabel AlDhahir, Ms. Suer Zhou, Ms. Yu Li, Mr. Zheng Zhang, Ms. Varnika Agarwal, and Mr. Yun Xiao for being enthusiastic learners to expand my research and the research group.

In the end, I would like to acknowledge friends in Oxford who gave me a deeper insight into my life. And above all, I would like to thank my family for giving me the opportunity to challenge and for supporting me from their heart.

Statement of Originality

This thesis is an account of work carried out by the author in the Department of Materials, the University of Oxford under the supervision of Dr Andrew Watt. Where the work of others has been drawn upon this is duly acknowledged in the text, and a list of references is presented at the end of each chapter. No part of this thesis has been submitted towards the completion of another degree at the University of Oxford or elsewhere. Parts of the thesis have been submitted to or published in the following scientific journal or conference presentation.

Journal article:

Tazawa, Y.; Habisreutinger, S. N.; Zhang, N.; Gregory, D. A. F.; Nagamine, G.; Kesava, S. V.; Mazzotta, G.; Assender, H. E.; Riede, M.; Padilha, L. A.; *et al.* Carbon Nanotubes for Quantum Dot Photovoltaics with Enhanced Light Management and Charge Transport. *ACS Photonics* **2018**, 5, 4854-4863. doi: 10.1021/acsphotonics.8b00982

Conference presentations:

Tazawa, Y.; Habisreutinger, S. N.; Zhang, N.; Nicholas, R.J.; Watt, A.A.R. p^{++}-p-i-n Heterojunction PbS CQD Solar Cells using Carbon Nanotube/Polymer. In *12th Photovoltaic Science, Application and Technology Conference (PVSAT-12)*, Liverpool, UK, 2016.

Abstract

Colloidal quantum dot (CQD)-based photovoltaics are an emerging low-cost solar cell technology with power conversion efficiencies exceeding 14%, i.e., high enough to be interesting for commercialization. Well-controlled and understood charge carrier transport through the device stack is required to make the next step in efficiency improvements.

In chapter 5, polymer-wrapped single-walled carbon nanotube (SWNT) films embedded in an insulating poly(methyl methacrylate) (PMMA) matrix and capped by a thermally evaporated Au electrode are investigated as a composite hole transport layer and optical spacer. Employing transient absorption spectroscopy this chapter shows that the SWNTs enhance the charge transfer rate from CQD to CQD, ZnO, or SWNT. In order to pinpoint the underlying mechanism for the improvement, the energetics of the junction was investigated by measuring the relative alignment of the band edges, using Kelvin probe and cyclic voltammetry. The measurements of the external quantum efficiency and absorption gave a perspective that the improvement is not mainly from electronic improvements but from enhanced absorption of the CQD absorber. The hypothesis that the transparent PMMA matrix acts as an optical spacer which enhances absorption in the absorber layer, was proven experimentally and theoretically. With these electronic and optical enhancements, the efficiency of the PbS CQD solar cells improved from 4.0% to 6.0%.

In chapter 6, a SWNT-P3HT composite was utilized in a bulk heterojunction structure with a PbS EDT layer. A bulk heterojunction structure is the architectural approach to have better charge transport while thickening the PbS CQD photoactive layer of the photovoltaic devices. Devices with a bulk heterojunction layer of SWNT-P3HT composite and PbS CQD with 1.2-Ethanedithiol (EDT) were compared with control devices which have planar heterojunction structure between PbS-EDT and SWNT-P3HT with varying the thickness of PbS-EDT layer from 60 nm to 240 nm. Among all devices, bulk heterojunction devices with 120 nm PbS-EDT thickness recorded the highest power conversion efficiency of 11.5%. In general, bulk heterojunction devices exhibited better carrier transfer with less monomolecular carrier recombination. As a result, devices with bulk heterojunction structure have demonstrated better fill factor values. By thickening the PbS-EDT layer from 60 nm to 240 nm, both bulk heterojunction devices and planar heterojunction devices showed increases in absorption. The bulk heterojunction devices could increase J_{sc} while the thickness of PbS-EDT layers were thickened up to 240 nm. Contrary to the bulk heterojunction devices, the planar heterojunction devices had a decrease in J_{sc} after the peak of power conversion efficiency with 120 nm thick PbS-EDT layer. The difference in J_{sc} with thicker PbS-EDT layer was examined by IQE analysis and electronic impedance spectroscopy measurements.

In chapter 7, the optimized method to transfer the graphene layer to a PbS CQD thin film has been studied, and the device performance of the PbS CQD solar cells using graphene and the control PbS CQD solar cells were compared. First the effects of annealing and an acetone bath treatment to both graphene stacking and the quality of PbS CQD thin film have been explored. Although the annealing effect did not seem to have a sig-

nificant impact on the stacking of the graphene layer onto PbS CQD thin films, annealing had a detrimental impact to performances of PbS CQD devices. To understand the detrimental effect of those two treatments, FTIR and XPS measurements were done. Both measurements confirmed the removal of ligands coordinating to PbS nanocrystals and the oxidation of PbS nanocrystals which degrade the quality of PbS CQD thin films. The aim of annealing graphene devices is to make the graphene layer stick well to the PbS CQD thin film. However, Raman microscope mapping revealed that the graphene layer without annealing is stuck as well as the layer with annealing treatment with the same defect level. In the latter part of the chapter, side-by-side comparisons of the graphene device and the control device have been made. The graphene devices performed better over control devices in absorption and J_{sc}. Moreover, intensity-dependent V_{oc} measurements and quantum efficiency measurements confirmed that the graphene device has less monomolecular carrier recombination and better IQE which results in a better V_{oc} and FF. The results of electronic impedance spectroscopy further confirmed the better charge transfer with a graphene monolayer in PbS CQD PV devices. Thus the graphene layer has been proven to be a good hole transport layer.

Contents

1 Introduction **1**

1.1 Energy demand and CQD solar cells 1

1.2 Aim of the thesis 3

1.3 Structure of the thesis 4

2 Background **6**

2.1 Basics of solar cells 6

2.1.1 Basics of semiconductors 6

2.1.2 Basics of Schottky junctions 8

2.1.3 Basics of p-n junction solar cells 11

2.1.4 Performance of solar cells 14

2.2 Basics of colloidal quantum dots 17

2.2.1 Physical and chemical properties of quantum dots 17

2.2.2 Synthesis of colloidal quantum dots 19

2.2.3 Functionalization of colloidal quantum dots 20

3 Literature Review **25**

3.1 Structure of the Review 25

3.2 Advancement in synthesis of PbS CQDs 25

3.2.1 Size distribution improvement in CQDs 25

3.2.2 Size control in CQDs 26

3.2.3 Post-synthesis surface passivation 28

3.3 Advancement in functionalization of PbS CQDs 30
3.3.1 Two methods of ligand exchange 30
3.3.2 Different types of ligands 33
3.4 Advancement in PbS CQD PV device architecture 37
3.4.1 Planar heterojunction structure 37
3.4.2 Bulk heterojunction structure 38
3.4.3 Multi-junction structure 40
3.4.4 Band-alignment engineering 42
3.5 Low dimensional carbon materials for electronics 44
3.5.1 Graphene 44
3.5.2 Carbon nanotubes 47
3.6 Conclusions 48

4 Basic Experimental Methods **50**

4.1 Synthesis 50
4.1.1 PbS colloidal quantum dots 50
4.1.2 ZnO nanoparticles 51
4.1.3 SWNT-P3HT solution preparation 51
4.2 Characterization of colloidal quantum dots 52
4.2.1 UV-Vis-NIR spectroscopy 52
4.2.2 X-ray diffraction 52
4.3 Ligand exchange of colloidal quantum dots 53
4.3.1 Solid-state ligand exchange 53
4.3.2 Solution phase ligand exchange 54
4.4 Characterization of semiconductor thin films 55
4.4.1 Fourier-transform infrared spectroscopy (FTIR) 55
4.4.2 X-ray photoelectron spectroscopy (XPS) 55
4.4.3 Scanning Kelvin Probe 56

4.4.4 Transient absorption 56
4.4.5 Transmission electron microscopy (TEM) 57
4.4.6 Optical profilometry 57
4.4.7 Ellipsometry 57
4.4.8 Raman spectroscopy mapping 57
4.5 Device fabrication 58
4.5.1 Etching ITO substrates 58
4.5.2 Substrate cleaning 58
4.5.3 Spin-coating 59
4.5.4 Top electrode deposition 59
4.6 Device characterization 60
4.6.1 Focused ion beam scanning electron microscopy 60
4.6.2 Current and voltage (J-V) characteristics 60
4.6.3 External quantum efficiencies (EQE) 61
4.6.4 Integrating sphere reflectance measurements 62
4.6.5 Electronic impedance spectroscopy measurements 62

5 PbS CQD Solar Cells with SWNT-polymer Composite 63
5.1 Introduction 63
5.2 Results and Discussion 64
5.2.1 Device architecture and performance 64
5.2.2 Charge transfer 69
5.2.3 Optical enhancement 78
5.2.4 Simulation of optics 83
5.2.5 Stability 87
5.3 Conclusions 89

6 Bulk Heterojunction PbS CQD SWNT Solar Cells **90**

6.1 Introduction 90

6.2 Results and Discussion 91

6.2.1 Device architecture and performance 91

6.2.2 Comparison of BHJ and PHJ devices 97

6.3 Conclusions 106

7 PbS CQD Solar Cells with Graphene Electrode **108**

7.1 Introduction 108

7.2 Results and Discussion 109

7.2.1 Device architecture and performance 109

7.2.2 Influence of annealing and acetone bath 114

7.2.3 Comparison of control samples and graphene samples 119

7.3 Conclusions 125

8 Conclusions **127**

8.1 Summary of the thesis 127

8.2 Future work 129

8.2.1 Application of other 1D materials in PMMA matrices 129

8.2.2 Ordered patterning of SWNT in bulk heterojunction structure . 130

8.2.3 Monolithic tandem (multi-junction) solar cell with graphene as an interlayer 130

Bibliography **131**

List of Figures

1.1 Minimum cost of material extraction/Watt for potential inorganic photovoltaic materials.[1] 3

2.1 Schematic diagram indicating the overlap of occupied molecular orbitals which eventually forms the valence band. In the same manner, the overlap of unoccupied molecular orbitals forms the conduction band in both metallic, and semiconductor or insulator materials. As shown in the figure, while metals have an overlap of the conduction band and the valence band, semiconductors and insulators have a gap between them which is called band gap (E_g).[2] 6

2.2 Intrinsic semiconductors (a) schematic band diagram, (b) density of states, (c) Fermi distribution, and (d) carrier concentration.[3] 7

2.3 n-type semiconductors (a) Schematic band diagram, (b) density of states, (c) Fermi distribution, and (d) carrier concentration. For p-type materials with the same concentration of dopant, the position of ED, function F(E), and n(E) and p(E) will be flipped vertically with respect to E_i.[3] . 8

2.4 Schematic diagrams of how semiconductor bands bend at the interface with a conductive metal with respect to materials E_f. Φ_f is the work function of a metal, and Φ_i is the work function of the semiconductor. For an n-type semiconductor, the Schottky contact prevents the electrons flowing to the metal; Ohmic contacts facilitate electrons flowing to metal. 10

2.5 Uniformly doped p-type and n-type semiconductors before the junction is formed. (b) The electric field in the depletion region and the energy band diagram of a p-n junction in thermal equilibrium. 12

2.6 Schematic diagram of a p-n junction showing the process of exciton generation and transportation. qV_{oc} is the difference between the quasi-Fermi level (qE_f) of electrons in the n-type material (Fn) and quasi-Fermi level of holes in the p-type material (Fp) under illumination. The quasi-Fermi level qE_f is the Fermi level of photoactive materials under illumination or biased voltage. The mid-gap states and shallow traps are present in both the p- and the n-type materials. Shallow traps capture and/or release free carriers to the valence/conduction band through thermal activation. Mid-gap states act as catalytic sites for electron and hole recombination.[4] 13

2.7 Black body spectrum, the spectrum of sunlight at the top of the atmosphere (yellow-shaded), and the spectrum of the sun at the sea level after absorption by atmospheric molecules (red-shaded).[5] 14

2.8 J-V curves of a solar cell in the dark (black solid line) and under AM1.5 illumination (red solid line). The area of the orange rectangle represents the maximum power output, the product of the optimally-chosen operating current and voltage.[4] 16

2.9 (a) J-V characteristics of the diode with standard R_{SH} and standard R_S (blue line) and of the diode with standard R_{SH} and higher R_S (green line). (b) J-V characteristics of the diode with standard R_{SH} and standard R_S (blue line) and of the diode with lower R_{SH} and standard R_S (orange line).[6] 17

2.10 The density of states D(E) of low-dimensional semiconductor structures: (a) quantum well (two-dimensional); the broken curve represents the three-dimensional density states, (b) quantum wire (one-dimensional), (c) quantum dot (zero-dimensional).[7] 17

2.11 Schematic illustration of the hot-injection synthesis and Ostwald ripening to form monodisperse nanoparticles.[8] 20

2.12 (a) Schematic diagram of PbS nanocrystal with only organic MPA ligand exchange/passivation (left-hand), and nanocrystal with both MPA and halide ligand exchange/passivation. While the organic-only passivation left some empty trenches on the surface of the nanocrystal, the halide treatment gives finer passivation. (b) Schematic diagram to illustrate how nanocrystals are partially fused from left-hand side rather loosely packed state to right-hand close-packing film.[9] 23

2.13 (a) Surface-bound molecules shift quantum dot energy levels (leading to p- or n-type behavior) by inducing variable surface dipoles.[10] (b) Energy level diagram of PbS CQDs exchanged with different ligands. Each column represents different ligand coordinating PbS CQDs which has E_g of 1.29 eV.[11] 24

3.1 (a) Graph showing the relationship between the size of PbS CQD, its crystalline shape and cation to anion ratio, both simulated and backed by experimental data. (b) Plot revealing the size-dependent stability of PbS CQD to oxidation. The extent of the peak shift represents the amount of oxide shell formed on the PbS CQDs. (a) and (b) are reproduced from[12] 27

3.2 (a) Device performance metrics of Schottky solar cells against the size of the PbS CQDs used. In this study, the optimal band gap is found to be about 1.3 eV. Figure was reproduced from reference.[13] (b) The generalized relationship between band gap and experimental V_{oc}, theoretical V_{oc} (limited by a maximum of J_{sc}) and thermodynamical V_{oc}. This graph and the inserted graph show that it is unwise to gain V_{oc} by increasing the band gap because the gain in V_{oc} is limited while the higher bandgap suffers a loss in J_{sc}. Figure was reproduced from reference.[14] . 28

3.3 (a) Graph indicating better trap passivation by using a hybrid ligand exchange strategy. (b) The effect of different metal cations of metal chloride used in synthesis as a treatment procedure. Better PLQE is an indicator of better trap passivation. (c) Cation-exchanged PbSe (from CdSe) showing remarkable performance and stability and this same strategy was used for PbS solar cells. (a) is obtained from reference,[15] while (b) is from reference[16] and (c) is from reference.[17] 29

3.4 Schematic illustration of the (a) solid-state ligand exchange process, and (b) solution-phase ligand exchange process. 30

3.5 (a) A PbS CQD model depicting iodide ligands passivating the Pb rich PbS CQD surface and the methylammonium counterion balances the overall charge. (b) Absorption curve showing the presence of PbS CQD exciton peak before and after ligand exchange, which excludes any possibility of CQD aggregation during the process of ligand exchange. The slight red shift, however, is due to stronger coupling between CQDs due to closer proximity between CQDs with the smaller sized iodide ligands. (c) The device architecture which incorporates the iodide exchanged PbS CQD.[18] 33

3.6 Carrier mobility showing an exponential dependence on ligand length. Mobility is extracted from Field Effect Transistor studies of PbSe CQD Films. Reproduced from reference.[19] 34

3.7 (a) Cross-sectional illustration of the planar heterojunction PbS CQD solar cell with 300 nm-thick PbS film which is thicker than the charge collection length. (b) Band diagram of the device illustrated in (a). This shows that the charge collection length is not long enough to complete charge transport from a single exciton pair. (c) Cross-sectional illustration of the bulk heterojunction PbS CQD solar cell with 300 nm-thick PbS film with ZnO nanowire arrays to shorten the pathways of electrons flowing from the PbS CQD layer to ZnO. (d) Band diagram of the device illustrated in (c). This shows that the path of electrons flowing from PbS to ZnO is shortened due to ZnO nanowire arrays. These are taken from reference.[20] 40

3.8 (a) Schematic cross-sectional diagram of multi-junction PbS CQD solar cell by Choi *et al.* (b) Band diagram of multi-junction PbS CQD solar cell illustrated in (a). (c) J-V Characteristic of solar cells from Tandem Solar Cells described in (a) of Front (PEDOT:PSS/1.6 eV PbS/ZnO/Al) and Back (PEDOT:PSS/1.0 eV PbS/ZnO/Al).[21] 41

3.9 (a) Band diagram of multi-junction PbS CQD solar cells developed by Wang *et al.* (b) solar spectrum of AM 1.5 with the indication of the Energy absorbed by 1.6 eV PbS CQD absorbing layer (green-shaded) and by 1.0 eV PbS CQD absorbing layer (red-shaded).[22] 42

3.10 (a) Energy levels concerning vacuum for pure PbS-TBAI, pure PbS-EDT and PbS-TBAI films covered with different thicknesses of PbS-EDT layer. UPS determined the Fermi levels (Ef) and valence band edges (blue lines). The conduction band edges (red lines) were calculated by adding the optical bandgap energy of 1.33 eV, as determined from the first exciton absorption peak in the QD thin films. (b) Schematic energy level alignment at PbS-TBAI and PbS-EDT interfaces deduced from UPS, where E_{VAC} is the vacuum energy. (c) Schematic illustration of proposed band bending in ZnO/PbS-TBAI (left) and ZnO/PbS-TBAI/PbS-EDT (right) devices at short-circuiting conditions.[23] 44

46

3.12 Schematic representation of graphene layers in (a) inorganic, (b) organic, and (c) dye-sensitized solar cells, (d) organic light emittting devices, and (e) a photodetector.[24] 47

4.1 Schematic illustration of ITO etching with the 2D dimension of the glass substrates and ITO pattern after etching. 58

5.1 (a) Device structure of PbS CQD solar cells using SWNT/P3HT in PMMA matrix (70 nm) as a hole transport layer between light-harvesting PbS-iodide (270 nm) and Au (100 nm) cathode. (b) FT-IR spectra of colloidal PbS CQDs films on glass substrates before and after solution-phase ligand exchange from oleic acid ligand to methylammonium iodide ligand. Additional N-H peaks at 3500-3300 cm^{-1} and at 1640-1560 cm^{-1} appeared after the solution-phase ligand exchange that corresponds to the N-H bond in a methylammonium ligand. Deviation from the average height of the surface of (c) SWNT-P3HT in PMMA film and (d) pristine PMMA film over an area of 0.546 mm^{-2}. 66

5.2 (a) FIB-SEM micrograph of cross-section of the device with SWNT/P3HT-PMMA. (b) TEM micrograph of spin-coated SWNT/P3HT. 67

5.3 J-V curves for champion PbS CQD PV devices with SWNT/P3HT in PMMA (SWNT: red line with squares), without SWNT/P3HT in PMMA (Control: black line with circles), and with P3HT(P3HT: yellow line with triangles) in both forward bias (broken line), and reverse bias (solid line). 68

5.4 (a) J_{sc}, (b) V_{oc}, (c) FF, and (d) PCE of devices without SWNT/P3HT (Control in figure), devices with SWNT/P3HT (SWNT in figure), and devices with only P3HT at day 2 of storage in the air. Square symbols at the middle of the boxes are mean values. The upper lines, middle lines, lower lines of the boxes are representing 75^{th} percentile, median, and 25^{th} percentile respectively. Sticks cover maximum and minimum values excluding outliers that are outside the upper or lower lines. The reported mean values and percentiles for all parameters were calculated from a sample of 12 devices. 69

5.5 Cross-section illustration of the stacking PbS CQD, PMMA and Au layers. Carbon nanotubes are embedded in PMMA matrix and conduct holes from PbS CQDs to the Au electrode. 70

5.6 (a) a XPS valence band sepctrum of a SWNT-P3HT thin film. (b) UV-Vis-NIR sepctrum of SWNT-P3HT thin film. (c) Conduction band, valence band and Fermi level of materials used in the device stack. The Fermi levels of the semiconductors are represented as dotted lines, and the Fermi levels of conductive electrodes (ITO, and Au) as solid lines. (d) Schematic illustration of band bendings in the planar and bulk heterojunction devices. 72

5.7 Plot of the logarithm of current density *versus* voltage under a light intensity of 1400 Wm^{-2}, 1000 Wm^{-2}, 600 Wm^{-2}, 250 Wm^{-2} and 100 Wm^{-2} for (a) control device and (b) SWNT device. (c) V_{oc} of the control device (without SWNT: red and square symbols) and SWNT device (with SWNT: black and circles symbols) under different illumination intensities. The slope of the linear fitting to V_{oc} *versus* logarithm of light intensity was analysed as the factor to the thermal voltage. 74

5.8 (a) Transient absorption for thin films (270 nm) of PbS CQD capped with oleic acid ligands (OA: open circles, thickness 200 nm), PbS CQD with iodide ligands (Control blue circles), and PbS CQD with iodide ligands with SWNT/P3HT (SWNT red squares). The pump laser for excitation was chosen at 1.55 eV (800 nm) at an estimated photon flux of about 4×10^{14} photon cm^{-2}. The probe was selected to be at the first absorption peak for those samples, 1.30 eV (950 nm). (b)Pump fluence dependence transient absorption for the OA capped sample. The fitting indicates a fast decay of 17±1 ps. 76

5.9 (a) Nyquist plot of impedance spectra of control and SWNT devices under 617 nm wavelength illumination at a bias voltage equivalent to the solar cell open circuit voltage. (b) |Z| *versus* frequency plot and theta *versus* frequency plot corresponding to acquired Nyquist plots. (c) Equivalent RC circuit used to fit the impedance spectra, where R_{ser} is the series resistance, C_{tot} is the total capacitance in the solar cell, and R_{char} is the charge transfer resistance in the solar cell. 78

5.10 (a) Absorbance of control sample (black squares) without both SWNT/P3HT and PMMA, 70 nm (SWNT with 70 nm PMMA matrix) device (red circles), and 200 nm (SWNT with 200 nm PMMA matrix) device (blue triangles). (b) External quantum efficiencies (EQE) for control (black squares), 70 nm (SWNT with 70 nm PMMA matrix) device (red circles), and 200 nm (SWNT with 200 nm PMMA matrix) device (blue triangles) as a function of wavelength from 400 nm to 1200 nm. 80

5.11 Comparison of J_{sc} for control device and SWNT devices. The thickness of PMMA were varied over the range 0 nm, 20 nm, 70 nm, 150 nm, 200 nm, 400 nm, 600 nm for these SWNT devices. 81

5.12 Absorbance of (a) a set of full control stack without both SWNT/P3HT and PMMA, 0 nm (SWNT without PMMA matrix), 20 nm (SWNT with 20 nm PMMA matrix), and 70 nm (SWNT with 70 nm PMMA matrix) device, (b) a set of control, 70 nm device, 150 nm device, and 200 nm device, and (c) a set of control, 200 nm device, 400 nm device, and 600 nm device. EQE of (d) a set of control without both SWNT/P3HT and PMMA, 0 nm (SWNT without PMMA matrix) device, 20 nm (SWNT with 20 nm PMMA matrix) device, and 70 nm (SWNT with 70 nm PMMA matrix), (e) a set of EQE of control, 70 nm device, 150 nm device, and 200 nm device, and (f) a set of EQE of control, 200 nm device, 400 nm device, and 600 nm device. 82

5.13 (a) Shunt resistance, and (b) series resistance of control devices and SWNT devices with different PMMA thickness from 20 nm to 600 nm. For the shunt resistance, the control samples exhibited higher (better) values compared to the SWNT devices regardless of their PMMA thickness. 83

5.14 These two graphs show the modelled absorption of the incident wavelengths in the different layers as a fraction of the total incident light (per wavelength), as well as the wavelength-dependent total reflection of the stack. 84
5.15 The simulation of red-IR absorption of the device stack in the presence of the PMMA layer. Two different simulated models are compared. One is in the absence of the optical spacer (top), and another is in the presence of an optical spacer of 50 nm (bottom). 85
5.16 Excitation generation for device stacks with PMMA layers of different thicknesses. This simulation demonstrates the position in the absorber layer where charges are generated for an incident AM1.5 spectrum. . . 86
5.17 PMMA thickness dependence of the J_{sc} current density on the assumption of 100% IQE. The model stack includes, analogously to the experimental devices, the following layers at a fixed thickness; glass as substrate, a layer of ITO (100 nm), ZnO (200 nm) as n-type layer, the PbS absorber (220 nm) and gold (100 nm). 87
5.18 The variation of photovoltaic performance metrics of devices with and without SWNT/P3HT-PMMA with storage time. (a) J_{sc}, (b) V_{oc}, (c) FF, and (d) PCE. The devices were unencapsulated and were stored in ambient air between each measurement in a dark environment without any humidity control. The standard deviation (error bars) and the average (data point) were calculated from a sample of 12 devices on 4 separate substrates. 88

6.1 Schematic illustrations of (a) PbS CQD solar cell with a planar heterojunction structure, and (b) PbS CQD solar cell with a bulk heterojunction structure. (c) Energy band diagram showing the energy levels of all functional layers in planar and bulk heterojunction devices. (d) Schematic illustration of band bendings in the planar and bulk heterojunction devices. 92

6.2 (a) FIB-SEM cross-sectional image of bulk heterojunction structure PbS CQD solar cell with 240 nm PbS-EDT and with SWNT-P3HT layer. (b) Schematic illustration of the cross-section of carbon nanotubes embedded in the PbS-EDT layer on the PbS-PbI_2/AA and conduct holes to Au electrode. 94

6.3 J-V curves for median bulk heterojunction structure (BHJ: red line with circle symbols), planar heterojunction structure (PHJ: black line with square symbols), and control (Control: blue line with triangular symbols) PbS CQD devices at (a)60 nm, (b) 120 nm, (c) 180 nm, and (d) 240 nm thickness of PbS-EDT. 95

6.4 (a) J_{sc}, (b) V_{oc}, (c) FF,and (d) PCE of PbS CQD bulk heterojunction solar cells (BHJ) and PbS CQD planar heterojunction solar cells (PHJ) at different thickness of PbS-EDT layer under AM1.5 illumination in nitrogen atmosphere at day 1 of storage. The reported mean values and error bars for all parameters were calculated from a sample of 12 devices. 97

6.5 Comparison of V_{oc} values in BHJ and PHJ devices *versus* light intensity in logarithmic scale plots with (a) 60 nm, (b) 120 nm, (c) 180 nm, and (d) 240 nm EDT thickness. 98

6.6 Comparison of BHJ (red solid line with circular symbols) and PHJ (black solid line with square symbols) in external quantum efficiency (EQE) over 350 nm to 1100 nm wavelength with (a) 60 nm, (b) 120 nm, (c) 180 nm, and (d) 240 nm EDT thickness. 100

6.7 Absorbance of (a) BHJ devices and (b) PHJ devices with EDT thicknesses of 60 nm (black solid line), 120 nm (red solid line), 180 nm (blue solid line), 240 nm (green solid line) from 400 nm to 1200 nm. 102

6.8 Comparison of BHJ (red solid line with circular symbols) and PHJ (black solid line with square symbols) in internal quantum efficiency (IQE) with (a) 60 nm, (b) 120 nm, (c) 180 nm, and (d) 240 nm EDT thickness from 350 nm to 1100 nm. 104

6.9 Nypuist plots of impedance spectra of (a) BHJ and (b) PHJ devices under 617 nm wavelength light illumination at a bias voltage equivalent to solar cells open circuit voltage. (c) Equivalent circuit of RC single model which was used to fit the impedance spectra, where R_{ser} is the series resistance, C_{tot} is the total capacitance in the solar cell, and R_{char} is the charge transfer resistance in the solar cell. 105

7.1 Schematic illustration of the graphene transfer process. Graphene layer was sandwiched by the copper substrate and the PMMA film after CVD growth and PMMA shielding. 110

7.2 (a)Schematic illustration of PbS CQD photovoltaic device using graphene between PbS-EDT (120 nm) and Au (100 nm) cathode as a highly-conductive electrode, and PbS CQD photovoltaic device without graphene as a control. (b) Energy band diagram showing the energy levels of all functional layers in graphene devices. (c) Schematic illustration of band bendings in the graphene devices. 112

7.3 (a) J_{sc}, (b) V_{oc}, (c) FF, and (d) PCE of graphene incorporated devices with annealing (Ann. Graphene), of graphene integrated devices without annealing (Graphene), of control devices with annealing and acetone bath (Ann. Bath Control), of control devices soaked in an acetone bath without annealing (Bath Control), of control devices with annealing but without acetone bath (Ann. Control), and of control devices without either annealing and acetone bath (Control) under AM1.5 illumination at day 1 of storage in the air. The reported mean values and error bars for all parameters were calculated from a sample of 12 devices. 113

7.4 FT-IR transmission spectra of (a) PbS EDT layer, and (b) PbS PbI_2/AA layer on glass substrates from wavenumber 3500 cm^{-1} to 1500 cm^{-1}. Both EDT and PbI_2/AA samples have been treated in an acetone bath (Bath in a figure), Annealing (Annealing in a figure), or both annealing and acetone bath (Annealing + Bath in a figure). 115

7.5 X-ray photoelectron spectra of (a) PbS-PbI_2/AA thin film and (b) PbS-EDT thin film samples on glass from 525 eV to 545 eV of binding energy corresponding to the O 1s orbital. The intensity peak of the counts for that energy range is analyzed by Gaussian distributions and illustrated by dashed lines in three different colours (COO in blue, Pb-OH in red, and Pb-O in green). 116

7.6 (a) External quantum efficiency comparison of control (black squares), and graphene device (red circles). (b) External quantum efficiency comparison of annealed graphene device (blue top-pointing triangular symbols), and graphene device (red circles). (c) External quantum efficiency comparison of control samples with annealing and acetone bath (yellow left-pointing triangular symbols), with only an acetone bath treatment (Grey right-pointing triangular symbols), with only annealing treatment (green diamonds), and with no treatment (black squares). 117

7.7 Raman mapping at the boundary of pristine PbS layer and graphene on top of PbS layer with or without annealing. Mapping has been done by taking an integral of the spectra from 1500 cm^{-1} to 1700 cm^{-1} in a raster of 17 $\times$ 38 dots over an area of 16.29 μm$\times$ 36.61 μm at the edge of the graphene strip on PbS CQD thin films. 119

7.8 JV curve comparison of graphene device (a solid red line with red circular symbols), and of control device without an acetone bath treatment (a solid black line with black square symbols) under AM1.5 illumination. . 120

7.9 (a) J_{sc}, (b) V_{oc}, (c) FF and (d) PCE of graphene incorporated devices without annealing (Graphene), of control devices without annealing (Control) under AM1.5 illumination at day 1 of storage in the air. The reported mean values and error bars for all parameters were calculated from a sample of 12 devices. 121

7.10 (a)Absorbance of graphene device (red solid line), and control device (black solid line) from 400 nm to 1200 nm. (b) Comparison of graphene devices (red solid line with square symbols) and control devices (black slid line with circular symbols) in internal quantum efficiency (IQE) from 350 nm to 1100 nm. 122

7.11 Plots of the logarithm of current desnity *versus* voltage under light intensity of 1250 Wm^{-2}, 1000 Wm^{-2}, 750 Wm^{-2}, 500 Wm^{-2}, 250 Wm^{-2}, and 100 Wm^{-2} for (a) control device, and (b) graphene device. (c) V_{oc} of the control device (without graphene: red squares) and graphene device (with graphene: black circles) under different illumination intensities. The slope of the linear fitting to V_{oc} *versus* logarithm of light intensity was analysed as the factor to the thermal voltage. 123

7.12 (a) Nyquist plots of impedance spectra of control and graphene devices under 617 nm wavelength light illumination at bias voltage equivalent to solar cells open circuit voltage. (b) Impedance modulus |Z| *versus* frequency plots corresponding to the acquired Nyquist plots. (c) Phase angle theta *versus* frequency plots corresponding to the acquired Nyquist plots. (d) Equivalent circuit of RC single model which was used to fit the impedance spectra, where R_{ser} is the series resistance, C_{tot} is the total capacitance in the solar cell, and R_{char} is the charge transfer resistance in the solar cell. 124

Chapter 1

Introduction

1.1 Energy demand and CQD solar cells

Humanity requires energy to exist; in 2013 the U.S. Energy Information Administration (EIA) reported that world energy consumption will grow by 56% between 2010 and 2040.[25] That projection reflects the prospective augmentation of the population growth and energy consumption, especially in developing countries. To fulfill the growing demand for energy supply, solar energy has the potential to be an enormous primary energy source for human in the future. According to Perez *et al.*, energy consumption across the globe is estimated to reach 27 TWyr in 2050, and solar illumination to the earth surface is around 23000 TWyr.[26] If devices converting solar energy into secondary energy satisfy economic and environmental requirements, utilizing solar energy could play an important role in the future. According to the World Population Dashboard, the population in Africa or Arab states has recorded over 2% in the average annual rate of population increase from 2010 to 2017.[27] Although there has been a dramatic economic development in Africa, GDP per capita in sub-Saharan Africa is only $3,466.73 compared with the world average of $17,300.[28] Thus, low-cost photovoltaic device technology is required in economically developing regions which requires more energy to match the energy supply to a dramatic population growth.

There are two key factors that make production costs for PV expensive; firstly materials costs and secondly the complexity of the manufacturing process. Photovoltaic

devices can be categorized into three generations, and each generation has different characteristics controlling those two factors affecting the costs. For first generation solar cells (most commonly installed with silicon as a light-harvesting material), the extraction cost of the silicon is the dominant cost. An energy input of 24 kWh/kg is required to produce usable metallurgical-grade silicon from silica which results in a raw material cost per watt to 0.039 ¢/W.[29] For second generation thin film solar cells, expensive rare earth metals are widely used, for example indium for copper indium gallium selenide (CIGS) solar cells for which the raw material cost is 0.023 ¢/W.[1] Fabrication of second generation thin film solar cells is by chemical vapor deposition (CVD) methods. Although CVD can provide highly pure materials with fine structural control, it is difficult to deposit multicomponent materials with well-controlled stoichiometry.[30] Most of these two generations of solar cells have a theoretical limit in efficiency to convert solar energy to electricity which is around 34% (Shockley-Queisser limit). To overcome this limit, there are some emerging third generation solar cells which includes colloidal quantum dots solar cells. Third generation solar cells, such as those based upon PbS colloidal quantum dot (CQD), present the possibility to build robust, low-cost photovoltaic devices using facile solution processing.[31,32] In addition to the simplicity of the production technique, PbS CQD solar cells are expected to have a low cost of material extraction as shown in figure 1.1 cited from Wadia *et al.*.[1] It is explicit that raw material cost of lead sulphide (0.0022 ¢/W) is 18 times smaller than crystalline silicon cost (0.039 ¢/W). Thus, PbS CQD solar cells have a potential to be a great candidate for next-generation low cost photovoltaic devices. However, CQD solar cells need some improvement in their performances, and this thesis addresses to improve their performances through the following aims.

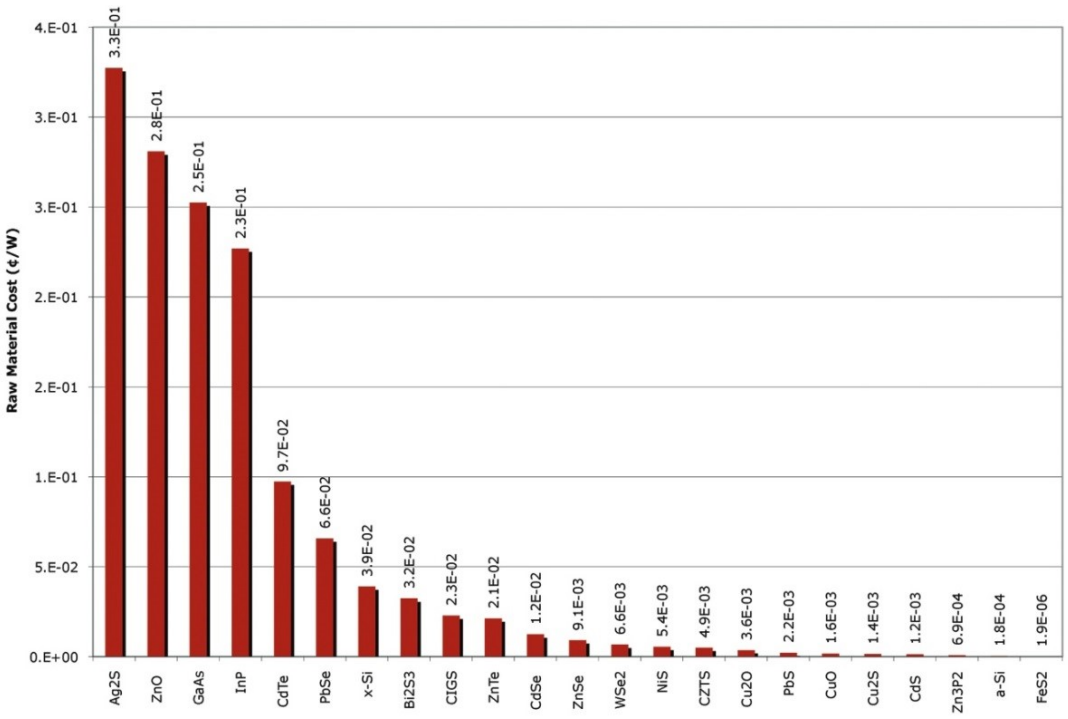


Figure 1.1: Minimum cost of material extraction/Watt for potential inorganic photovoltaic materials.[1]

1.2 Aim of the thesis

This thesis aims to improve the efficiency of colloidal quantum dots solar cell by incorporating low-dimensional carbon nanomaterials in their device architectures. These low-dimensional carbon nanomaterials were utilized as a hole transport layer or a highly-conductive electrode in single-junction photovoltaics.

To realize that, first, the selection of the materials and the method of how to incorporate these materials into photovoltaic were decided regarding the physical and chemical characteristics of the materials. The physical characteristics could be categorized as mechanical strengths, electrical characteristics, and optical responses, while the chemical characteristics include dispersibility and stability to the specific solvent used in the device fabrication process. Regarding those aspects, the lower dimension carbon nanomaterials were employed in PbS CQD photovoltaics in a specific architecture and the processing chosen in this thesis.

Second, the selection of the characteristics to be measured is one of the most critical issues in this thesis to understand which improvements are brought about to the photovoltaic devices and the mechanisms behind those improvements. In addition to that point, the conditions to measure those properties of the photovoltaic devices are also important to acquire relevant data to analyse the mechanisms.

With the care for those aspects, chapter 5, 6, and 7 are aiming to understand the effects of the low-dimensional carbon nanomaterials to the optoelectronic property of CQD photovoltaic devices to enhance their J_{sc}, or fill factor values. In chapter 5, the composite of carbon nanotube and the polymer was utilized as the hole transport layer in CQD photovoltaics. The employment of the hole transport layer in the photovoltaic devices should improve their electric performances to prevent the recombination of carriers generated by the illumination. Based on that expectation, SWNT/P3HT-PMMA was integrated to PbS CQD solar cells to improve their overall efficiency. In chapter 6, carbon nanotubes are then mixed with PbS CQDs to realize the bulk heterojunction structure to achieve better carrier transport while the photoactive PbS CQD layers get thickened. Usually, thickening photoactive layer to aim a high photogenerated current induces the carrier recombination if the thicknesses exceed the tolerant level regarding the how fast and far carriers can diffuse in that layer. The methods how to integrate monolayer graphene as an electrode in the CQD photovoltaics were the main issues in chapter 7. Because there were no previous studies to stuck the graphene layer to CQD layer, conditions in graphene transfer process were the main focus. At the same time, the performances of the photovoltaic devices with or without graphene were compared.

1.3 Structure of the thesis

This thesis contains three different projects, two projects incorporating single-walled carbon nanotubes to colloidal quantum dots photovoltaics, and a project employing graphene as a hole transport layer in a single-junction solar cell.

Chapter 2 provides background knowledge related to the theme of this thesis. Chapter 3 presents state of the art of the colloidal quantum dots and the application of low-dimensional carbon nanomaterials such as carbon nanotubes and graphenes. Chapter 4 describes the detail of the basic experimental methods used in this thesis. In chapter 5, the application of single-walled carbon nanotubes with a polymer composite in PbS colloidal quantum dot solar cells as a planar hole transport layer is described. In chapter 6, a bulk composite of single-walled carbon nanotubes with PbS colloidal quantum dots was studied to maximize the thickness of the photoactive PbS layer. Chapter 7 is about the application of graphene as a highly-conductive electrode layer in PbS CQD single-junction solar cells. Finally, chapter 8 summarizes the insight from those three projects and suggests some future work as a development from those projects.

Chapter 2

Background

2.1 Basics of solar cells

2.1.1 Basics of semiconductors

In molecular orbital theory, when two atoms make a bond there should be a slight splitting of one energy level to two energy levels for bonding. The band is originating from the overlaps of every single molecular orbital in a crystal. The valence band (V.B.) is brought about with the overlaps of occupied molecular orbitals, and the conduction band (C.B.) originates from the overlaps of unoccupied molecular orbitals in crystals.

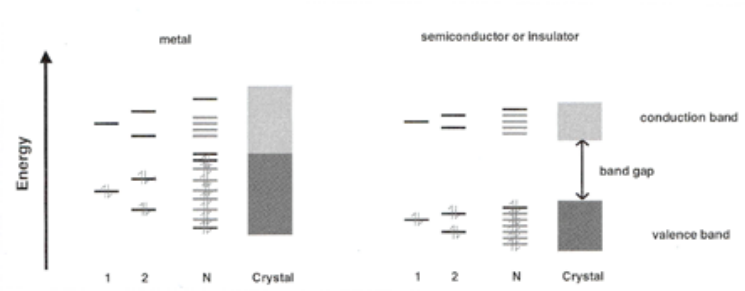


Figure 2.1: Schematic diagram indicating the overlap of occupied molecular orbitals which eventually forms the valence band. In the same manner, the overlap of unoccupied molecular orbitals forms the conduction band in both metallic, and semiconductor or insulator materials. As shown in the figure, while metals have an overlap of the conduction band and the valence band, semiconductors and insulators have a gap between them which is called band gap (E_g).[2]

Semiconductors or insulators have band gaps (Eg) which represent the gaps between their top of the V.B. and bottom of the C.B. while metal crystals have overlaps of

these two bands. If electrons below the V.B. excited to an energy level higher than the C.B., the absence of electrons in the V.B. is treated as the fictional particle as a hole (positively-charged particle) in the V.B.. Figure 2.2 below summarizes the band diagram, the density of states N(E), which varies as $\sqrt{E}$ for a given electron effective mass, the Fermi distribution function and the carrier concentrations for an intrinsic semiconductor, where E is the energy of the electrons. The density of states N(E) is the density of allowed energy states, including electron spin, per energy range per unit volume. The Fermi distribution F(E) is the probability of occupying that energy range, and can be expressed as the Fermi-Dirac distribution function below where k is the Boltzmann constant, T is the absolute temperature in Kelvin, and E_f is the Fermi level (E_f) of a semiconductor. E_f is lying in the band gap at the absolute temperature, and indicates the energy level at which the probability of occupation by an electron is exactly one-half, as indicated in eq(2.1).

$$F(E) = \frac{1}{1 + e^{\frac{E - E_f}{kT}}} \tag{2.1}$$

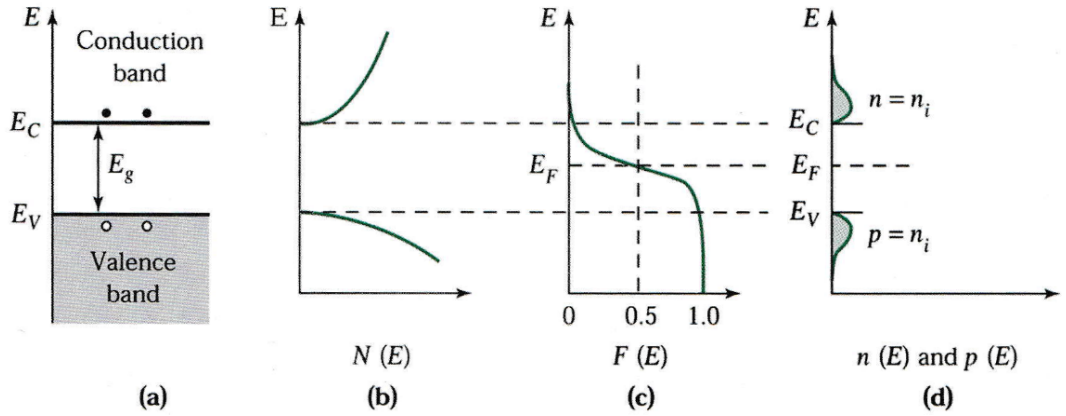


Figure 2.2: Intrinsic semiconductors (a) schematic band diagram, (b) density of states, (c) Fermi distribution, and (d) carrier concentration.[3]

An n-type semiconductor is a semiconductor that has electron donating doping elements, and the majority carriers are electrons. E_f for n-type semiconductor is closer to the C.B than the V.B. while E_f of intrinsic semiconductor lies at the exact middle

point of the C.B. and the V.B. positions. In contrast, a p-type semiconductor is a semiconductor that has electron accepting doping elements, and the majority carriers are holes. E_f for p-type semiconductors closer to the V.B. than the C.B.. Electron density (n), and hole density (h) of semiconductors can be expressed as following, where n_i: intrinsic electron concentration, p_i: intrinsic hole concentration, E_i: intrinsic Fermi level.

$$n = n_i e^{\frac{E_f - E_i}{kT}} \tag{2.2}$$

$$p = p_i e^{\frac{E_i - E_f}{kT}} \tag{2.3}$$

These equations show that there will be a high electron density and a low hole density for an n-type semiconductor, and there will be a low electron density and a high hole density for a p-type semiconductor.

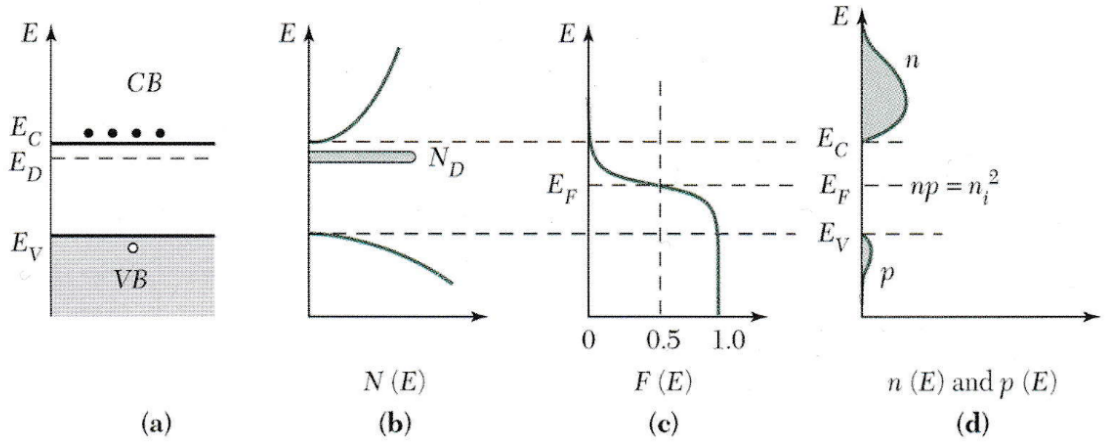


Figure 2.3: n-type semiconductors (a) Schematic band diagram, (b) density of states, (c) Fermi distribution, and (d) carrier concentration. For p-type materials with the same concentration of dopant, the position of ED, function F(E), and n(E) and p(E) will be flipped vertically with respect to E_i.[3]

2.1.2 Basics of Schottky junctions

If a semiconductor has a contact with a metal, its C.B., and V.B. bend up or down with respect to the E_f of the semiconductor and metal. If E_f of the semiconductor is different from E_f of the metal, electrons in a substance with shallower (i.e., nearer to E_{vac}) E_f flow into the other when they make contact with each other. Consequently, there will

be a built-in electric field at the interface between the semiconductor and the metal because of the change in carrier concentration. This equilibrium state is called thermal equilibrium. As shown in figure 2.4, at an interface between an n-type semiconductor and metal, when the work function of the n-type semiconductor is bigger than the one of contacting metal, the interface becomes less resistive regarding majority electron transportation. When the work function of the n-type semiconductor is smaller than the one of contacting metal, the interface becomes much resistive in terms of majority carrier: electron transportation. For a p-type semiconductor and metal, when the work function of the p-type semiconductor is bigger than the one of the contacting metal, the interface becomes resistive regarding majority hole transportation. When the work function of the p-type semiconductor is smaller than the one of the contacting metal, the interface becomes less resistive concerning majority hole transportation.

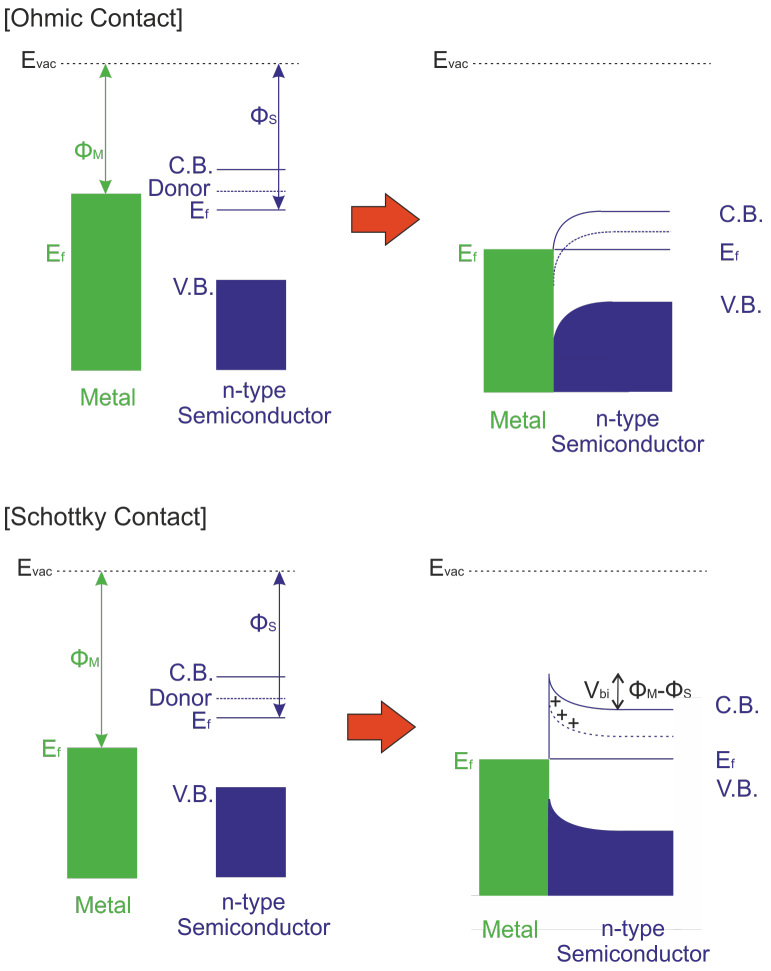


Figure 2.4: Schematic diagrams of how semiconductor bands bend at the interface with a conductive metal with respect to materials E_f. Φ_f is the work function of a metal, and Φ_i is the work function of the semiconductor. For an n-type semiconductor, the Schottky contact prevents the electrons flowing to the metal; Ohmic contacts facilitate electrons flowing to metal.

When an interface between a semiconductor and a metal forms a potential barrier making a resistive characteristic, that combination of semiconductor and metal is called a Schottky junction. In the junction, the region where bands bend with the built-in electric field is called the depletion region (or space-charge region). The reason why it's called depletion region is that the carriers in that region spontaneously move to the opposite layer to compensate the gradient at the interface of the junction and there is no charge there. The built-in bias (V_{bi}) created by this band-bending is determined by the E_f difference between the semiconductor and the metal before they are brought

into contact.

$$V_{bi} = \Phi_M - \Phi_S \tag{2.4}$$

The width of this depleltion region (W) can be expressed as the following equation where ϵ_s is the permittivity of the semiconductor, and N_a is the doping density of the semiconductor.

$$W = \sqrt{\frac{2\epsilon_s V_{bi}}{qN_a}} \tag{2.5}$$

In light-illuminated n-type semiconductor-metal Schottky junctions, the depletion region in the n-type semiconductor accumulates electrons due to the potential barrier with the band bending. As a consequence, Fermi level of a semiconductor rises and is called the quasi-Fermi level (qE_f). The potential difference between the metal's E_f and the semiconductors qE_f corresponds to the photogenerated voltage in a solar cell. The concepts of Schottky and Ohmic contacts are significant in the design of photovoltaic cells regarding carrier transport from the photoactive semiconductor to the metal contact, especially for a selection of interlayer materials of multi-junction solar cells. The careful selection of the interlayer of multi-junction solar cells is important to create and mitigate the potential barrier for target carriers to control the carrier flows to the interlayer. That control gives the ideal carrier recombination between different solar cell junctions.

2.1.3 Basics of p-n junction solar cells

In p-n junction solar cells, a p-type semiconductor and an n-type semiconductor are brought together, and they form a p-n junction as shown in figure 2.5. The formation of this junction is caused by majority carriers in the n-type material diffusing to the p-type, and vice versa. As a result of charge cancelation due to carrier diffusion, a depletion region is formed in both p and n type materials, where an electric field exists.

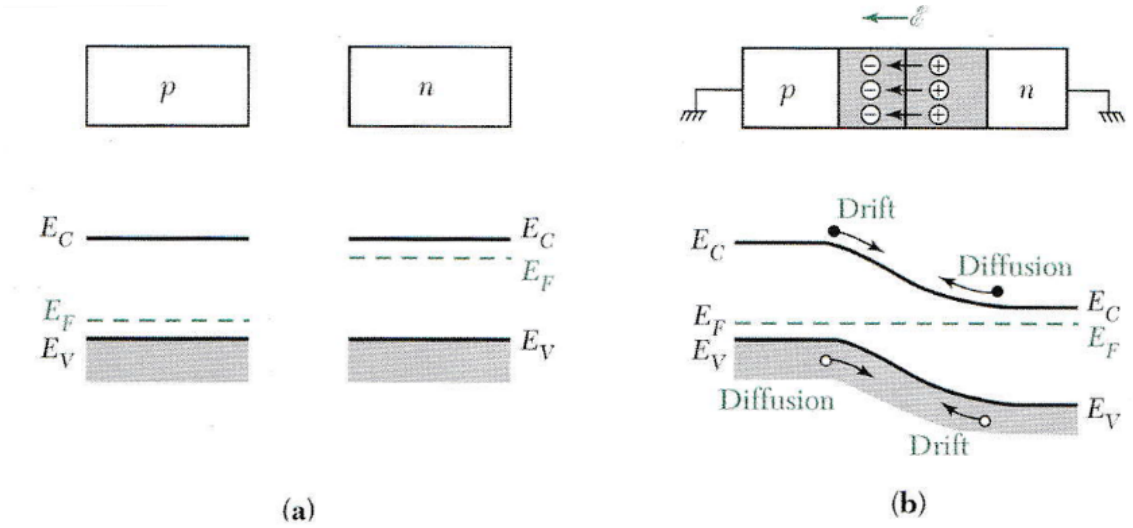


Figure 2.5: Uniformly doped p-type and n-type semiconductors before the junction is formed. (b) The electric field in the depletion region and the energy band diagram of a p-n junction in thermal equilibrium.

There are two fundamental ways for carriers to be transported in semiconductor materials especially with a junction: drift and diffusion. Drift is carrier transport driven by the applied electric field, especially those formed within the depletion region in a metal-semiconductor junction, or a p-n junction. Drift is affected by the mobility of carriers in the sample materials and the magnitude of the electric field applied. Diffusion occurs for majority carriers in a semiconductor (electrons for an n-type semiconductor, and holes for a p-type semiconductor) to minimize the gradient of carrier concentration. As illustrated in figure 2.5b, majority carriers follow the diffusion mechanism, and the minority carriers follow the drift mechanism in the p-n junction.[3]

If there are incident photons, the active absorbing semiconductor layer generates excitons. Next, the generated carriers flow in the semiconductor layer with diffusion and drift mechanisms. Eventually, those moving electrons and holes are separated from each other by the interface if the potential differences at the p-n junction are larger than the exciton binding energy. In the depletion region, electrons and holes are transported by the drift driven by the electric field at the interface. In the quasi-neutral region, carriers are moved towards electrodes by diffusion driven by the concentration

gradient. After dissociation of the excitons, the free carriers migrate to the conductive contacts under the influence of the built-in electric field in solar cells.

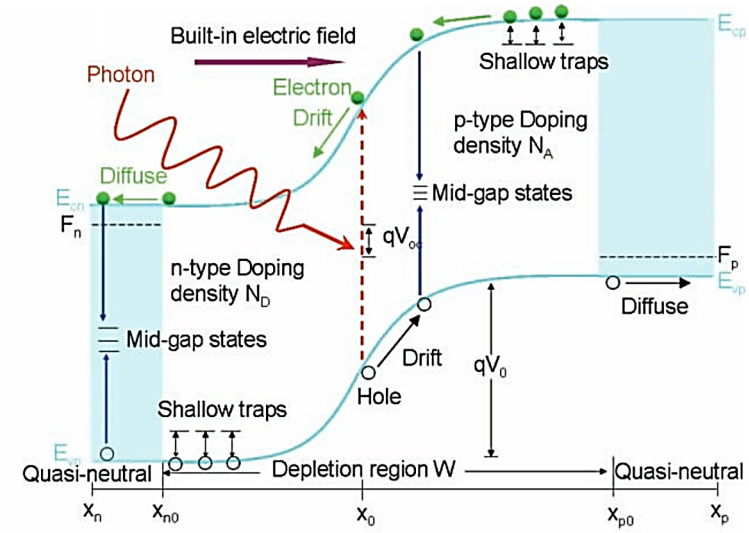


Figure 2.6: Schematic diagram of a p-n junction showing the process of exciton generation and transportation. qV_{oc} is the difference between the quasi-Fermi level (qE_f) of electrons in the n-type material (Fn) and quasi-Fermi level of holes in the p-type material (Fp) under illumination. The quasi-Fermi level qE_f is the Fermi level of photoactive materials under illumination or biased voltage. The mid-gap states and shallow traps are present in both the p- and the n-type materials. Shallow traps capture and/or release free carriers to the valence/conduction band through thermal activation. Mid-gap states act as catalytic sites for electron and hole recombination. [4]

As illustrated in figure 2.7, the solar spectral irradiance is peaked in the visible region (wavelengths: 390-700 nm), and there is still a large integrated intensity in the near-infrared spectral region as well. For solar cell research, the solar radiation is standardized with Air Mass 1.5 (AM 1.5) which is defined by the American Society for Testing and Materials (ASTM), and International Electrotechnical Commission (IEC). The air mass factor is defined as the ratio of optical path length after attenuation by the atmosphere to the optical path length when the sunlight reaches to the ground point vertically. Therefore, AM 1.5 is the solar radiation when the sun is at an angle of elevation of 42°, and its power density is 1000 W/m^2.

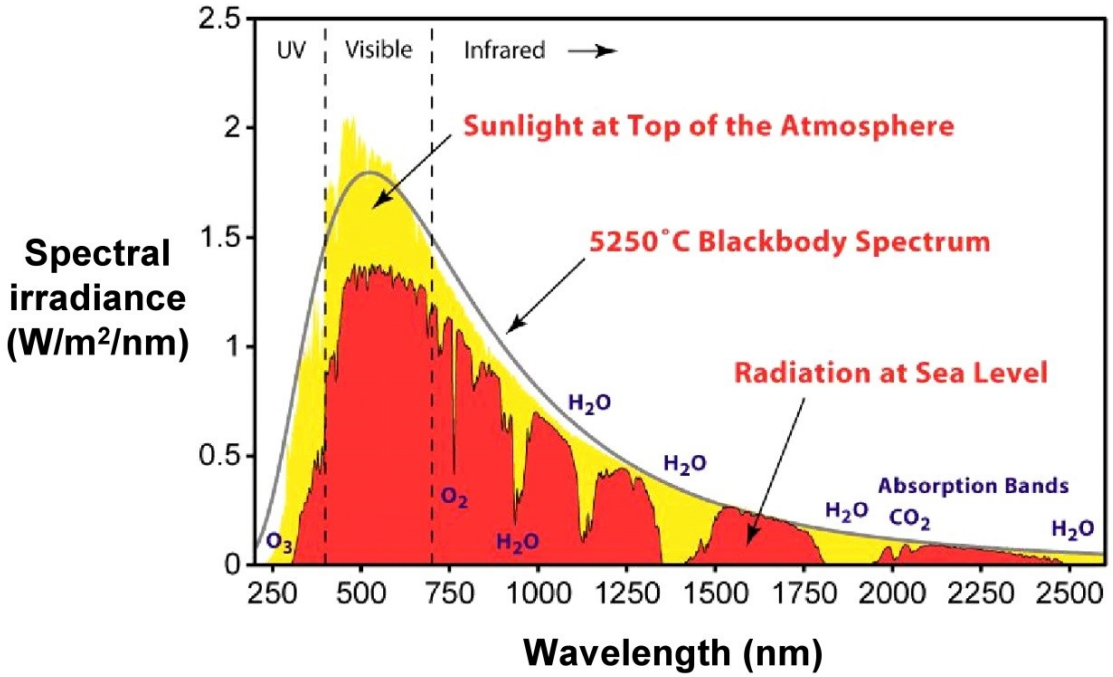


Figure 2.7: Black body spectrum, the spectrum of sunlight at the top of the atmosphere (yellow-shaded), and the spectrum of the sun at the sea level after absorption by atmospheric molecules (red-shaded).[5]

2.1.4 Performance of solar cells

The ability of a solar cell to absorb photons, generate charges and extract them to the external circuit is described by the term quantum efficiency (QE). QE is the probability of an electron being extracted to the external circuit by an incident photon of energy E. The current density generated by the solar cell under short circuit condition is given by equation 2.6, where $b_s(E)$ is the number of photons of energy in the range of E to E + dE incident on unit area in unit time, and q is the electronic charge.

$$J_{sc} = q \int b_s(E) QE(E) dE \tag{2.6}$$

When a load is present in a circuit with an illuminated device, the overall current is decreased, and a potential is developed between the terminals. The overall current can be regarded as the superposition of the short circuit current generated by photon absorption and a reverse current caused by the potential built-up under load. The

reverse current is the current flowing through a cell in the dark under bias. According to the single-diode model, the dark current density is given by equation 2.7, where J_0 is the reverse saturation current density which is a measure of recombination in a diode, V is the voltage between the cell terminals, n is the ideality factor, k is the Boltzmann constant and T is temperature.

$$J_{dark}(V) = J_0(e^{\frac{qV}{nkT}} - 1) \tag{2.7}$$

The value of ideality factor is dependent upon the recombination type. n=1 if recombination occurs in the neutral region, and n=2 if it occurs in the depletion region. The open circuit voltage V_{oc} reflects the potential difference between the quasi-Fermi level of electrons (Fn) in the n-type material and the quasi-Fermi level of holes (Fp) in the p-type material (see figure 2.6). The quasi-Fermi level of the semiconductor originates from the introduction of excess carriers under illumination. Such an illumination makes electron and hole concentrations higher than those in an equilibrium state, such that $pn > n_i^2$, where p is the hole density, n is the electron density, and n_i is the intrinsic carrier density. The net current density of a solar cell under illumination is given by equation 2.8.

$$J(V) = J_{sc} - J_{dark}(V) = J_{sc} - J_0(e^{\frac{qV}{nkT}} - 1) \tag{2.8}$$

In open circuit, the net current is zero i.e.,$J(V) = 0$, as all carriers recombine. The open circuit voltage can be expressed as equation 2.9.

$$V_{oc} = \frac{nkT}{q} ln(\frac{J_{sc}}{J_0} + 1) \tag{2.9}$$

Figure 2.8 shows the J-V characteristic of a solar cell in the dark and under incident photons. The dark current indicates the essence of the diode nature of solar cells. Under illumination, photo-generated carriers shift the J-V curve downward into the fourth quadrant. The power conversion efficiency η is given by the equation 2.10, where V_{max} is the voltage at the maximum power point, J_{max} is the current density at the maximum

power point, P_{inc} is the incident light intensity, V_{oc} is the open circuit voltage, J_{sc} is the short circuit current density, and FF is the fill factor ($FF = \frac{J_{max}V_{max}}{J_{sc}V_{oc}}$).

$$\eta = \frac{J_{max}V_{max}}{P_{inc}} = \frac{J_{sc}V_{oc}FF}{P_{inc}} \tag{2.10}$$

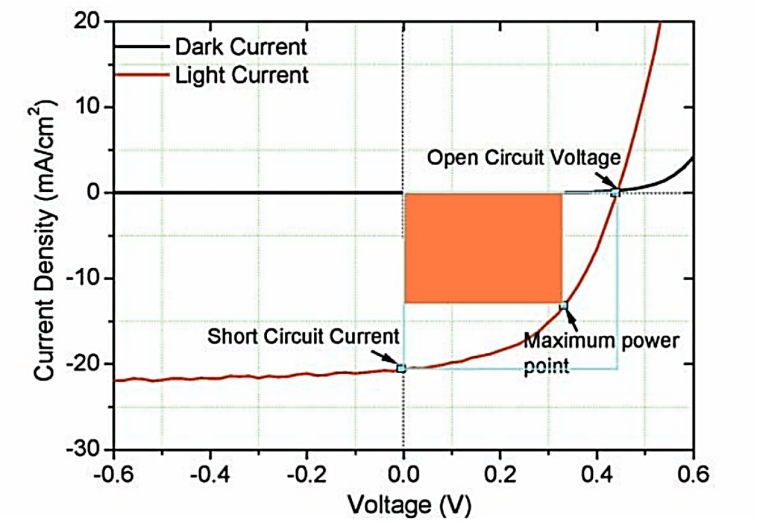


Figure 2.8: J-V curves of a solar cell in the dark (black solid line) and under AM1.5 illumination (red solid line). The area of the orange rectangle represents the maximum power output, the product of the optimally-chosen operating current and voltage.[4]

The fill factor (FF) represents the quality of the J-V characteristics and is affected by carrier recombination. Carrier recombination can be quantified by the series resistance R_s which is a resistance in the device architecture that prevents carrier transportation, and the shunt resistance R_{sh} which represents a resistance to avoid leakage currents. In order to get higher FF values, R_s can be reduced by minimizing contact resistance in the device, also R_{sh} can be increased by preventing leakage currents. To mitigate contact resistance, the morphology at the interface of the devices can be improved. To prevent the leakage currents, the complete separation between the p-type layer and the anode or the n-type layer and the cathode is ideal.

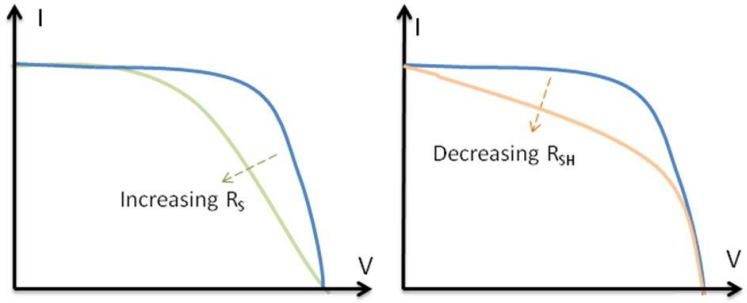


Figure 2.9: (a) J-V characteristics of the diode with standard R_{SH} and standard R_S (blue line) and of the diode with standard R_{SH} and higher R_S (green line). (b) J-V characteristics of the diode with standard R_{SH} and standard R_S (blue line) and of the diode with lower R_{SH} and standard R_S (orange line).[6]

2.2 Basics of colloidal quantum dots

2.2.1 Physical and chemical properties of quantum dots

A quantum dot is a nanocrystal exhibiting a quantum confinement effect, so the size is generally smaller than 20 nm. This quantum confinement effect is the effect of limiting the carriers' freedom in position to the nano scale. This extreme limitation makes the bandgap of the material wider than in the bulk. Moreover, the quantum confinement generates discrete energy levels as the degree of freedom in carriers is limited. If the diameter of the nanocrystals gets smaller than 10 nm, the quantum confinement effect would be more prominent, and the dependency of the bandgap would vary with the size of the nanocrystals.[33]

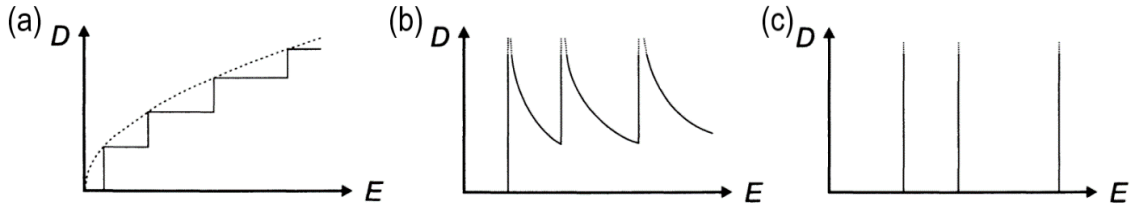


Figure 2.10: The density of states D(E) of low-dimensional semiconductor structures: (a) quantum well (two-dimensional); the broken curve represents the three-dimensional density states, (b) quantum wire (one-dimensional), (c) quantum dot (zero-dimensional).[7]

To get a strong quantum confinement effect, the radius of nanocrystals R should be far smaller than exciton Bohr radius α_{ex} (i.e., R/α_{ex}). For PbS, the exciton Bohr radius is 20 nm[34] corresponding to the bandgap of 0.5 eV.[35] The nanocrystal radius R must also be far smaller than the Bohr radius of an electron (α_e) and the Bohr radius of a hole (α_h).[36] In general, the exciton Bohr radius of a particle (α_B) is defined by the equation below, where α_0 is the Bohr radius of the semiconductor, m is the mass of the particle, m^* is the reduced mass, and ϵ_r is the size-dependent dielectric constant (relative permittivity).[37]

$$\alpha_B = \epsilon_r \frac{m}{m^*} \alpha_0 \tag{2.11}$$

What makes lead chalcogenide quantum dots intriguing is their small hole masses which leads to a large Bohr radius for holes. The band gap of quantum dots can also be widened by decreasing their size.[38–40] Thus, lead chalcogenide quantum dots satisfy conditions to exhibit strong quantum confinement characteristics and good tunability of the Eg.

Quantum dots also show the intriguing feature to generate multiple excitons with single photon radiation, which is called multiple-exciton generation (MEG). There has been much discussion about the mechanisms of MEG. The first possible mechanism causing MEG is impact ionization. In a p-n junction of a bulk semiconductor, MEG has been observed in Si, Ge, PbS, PbSe, PbTe, and InSb.[41–43] However, the extra energy of near-UV photons is not utilized fully in bulk semiconductor films owing to non-radiative thermal relaxation of photogenerated hot electrons and holes. This thermal relaxation makes the MEG mechanism in bulk semiconductors less efficient; the threshold photon energy required for MEG is far more than the available energy in the solar spectrum.[42] In quantum dots, however, the generation of multiple pairs of electrons and holes from a single photon becomes very efficient, and the threshold photon energy for the process to generate two electron-hole pairs per photon can approach values as low as twice the threshold energy for absorption (the absolute minimum to satisfy energy conservation).

This effect allows the threshold to occur in the visible or near-IR spectral region of AM 1.5.[42,44,45] Hence, quantum confinement effects enhance the possibility of more effective utilization of hot carriers that are generated by irradiation of a photon which energy higher than Eg of the semiconductor. One of the most promising aspects of CQD photovoltaics is that they have the potential to break the Shockley-Queissier limit through multi-exciton generation.[41,46]

2.2.2 Synthesis of colloidal quantum dots

Colloidal quantum dots are quantum dots capped with long-chain organic surfactant ligands (e.g., oleate ligands) so that they can be dispersed in an organic solvent. This dispersibility of quantum dots with stabilizing ligands enables quantum dots to be deposited on substrates by a solution process such as spin-coating, dip-coating,[32,47,48] spray-coating,[31] or ink-jet printing.[49–51] There are several ways to synthesize CQDs. For optoelectronic applications, the monodispersity of the CQD (size-distribution of the nanocrystals less than 5%) is one of the most significant factors. The thermal decomposition method is a low-cost and high-quality size-controlled synthesis method including the separation of nucleation and growth steps.[52–54] Thermal decomposition can be achieved by either the hot-injection or the heat-up method.[55]

The hot-injection synthesis method for CQDs by Hines *et al.* consists of two steps; rapid nucleation of organometallic precursors, and slow growth of nanocrystals.[56] The hot-injection method rapidly injects precursor(s) into a hot, high boiling point surfactant. The injection temperature significantly controls the decomposition of the precursors. Right after the injection, nucleation is initiated due to induced supersaturation and terminated by a rapid decrease of the reaction temperature with room-temperature injected precursors. Following nucleation, nanocrystal growth begins with the molecular addition of the monomeric precursor(s) remaining in solution. There are two mechanisms to obtain monodisperse CQD solutions during the growth stage. One

factor affecting size distribution is the lowering growth rates for bigger particles. According to Reiss, larger particles grow more slowly than smaller particles because the particle growth rate is inversely proportional to its radius.[57] On the other hand, there is an effect of Ostwald ripening which is a phenomena where smaller particles dissolve while bigger particles grow.[58] The majority of established CQD synthetic routes have used surfactant molecules with a hydrocarbon tail and a polar head (e.g., oleic acid, oleylamine, trioctylphosphine oxide, or dodecanethiol).[59] They can modify the reactivity of the precursors, and consequently control the nucleation and the growth rates.[60] After synthesis, the washing process is crucial for a better carrier transfer when CQDs are applied to an electronic device as an excess amount of surfactant prevents carrier transportation by making an excessive insulating layer and making the distance between CQDs wider.

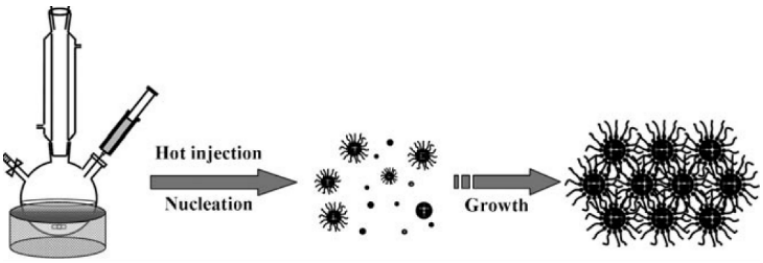


Figure 2.11: Schematic illustration of the hot-injection synthesis and Ostwald ripening to form monodisperse nanoparticles.[8]

2.2.3 Functionalization of colloidal quantum dots

To maintain colloidal stability in organic solvents, CQDs are capped with very long, insulating aliphatic ligands (e.g. oleate ligand, or oleylamine ligand). However, these are detrimental in terms of electronic transport in quantum dot solids because they increase the space between CQDs and cause low film density.[61]

To overcome such a problem, CQDs can be functionalized through the solid-state ligand exchange method or the solution-phase ligand exchange method. In the layer-by-layer solid-state ligand exchange method, depositions of a thin (approximately 10

nm thickness) layer of CQDs are followed by the exchange of ligands. Ligands are exchanged from the capping long-chain organic ligands to functional organic, inorganic halide, pseudohalide, halometallate ligands,[62] or organic-inorganic hybrid ligands[63] corresponding to the choice for the best one for each device structure. This process of deposition and ligand exchange is repeated until the desired thickness is achieved. Another way to exchange long insulating organic ligands to chemically and electronically functionalized ligands is the solution-phase ligand exchange method.[64,65]

Since the last decade, the ligands surrounding nanocrystals have been explored extensively to reduce the defect states, and to increase carrier diffusion lengths on the surface of the nanocrystals to enhance both J_{sc} and V_{oc}. Diffusion length is a significant factor in a semiconductor film as it determines the carrier transport in the diffusion region of actively biased solar cells. This diffusion length (l) can be expressed as below, and it is dependent on the carrier lifetime (τ) and minority carrier mobility (μ) where D is the diffusion coefficient, k is the Boltzmann constant, T is the temperature, and q is the electrical charge of the carriers.

$$l = \sqrt{D\tau} \tag{2.12}$$

$$D = \frac{\mu kT}{q} \tag{2.13}$$

The carrier lifetime is short when the trap density of the film is high,[66] so reducing the trap density brings about the longer diffusion length. Trap states are caused by surface defects on the nanocrystals which trigger the trap states to reduce V_{oc}, and behave as the non-radiative recombination centers.[67,68] Therefore, reducing or protecting the surface defects of the nanocrystals has been one of the areas of greatest interest for improving the physical properties of CQDs.

To passivate the surface defects of the nanocrystals, a selection of ligands have been employed for lowering the trap density and for obtaining longer diffusion lengths. Without any treatment with ligands, PbS CQDs have a trap density of $1 \times 10^{17} cm^{-3} eV^{-1}$

according to Ip *et al.*,[15] and a diffusion length of 30 nm. The trap density increases to $1.8 \times 10^{17} cm^{-3} eV^{-1}$ with EDT treatment.[69] Other organic ligands with thiol moiety, for example 1,4- benzenedithiol (BDT) and 3-mercaptopropinoic acid (MPA), have been also used to passivate PbS nanocrystals. The hole mobility of those bidentate thiol ligands are in the range of 1.0×10^{-4} (EDT) 1.0×10^{-3} (MPA) $cm^2 V^{-1} s^{-1}$.[70–72] However, it is known that the thiol moiety shows good bonding to surface Pb but poor coordination with S atom, which induces unpassivated site for S atoms on PbS nanocrystals. To solve this problem, research on inorganic passivating ligands has been initiated. The first inorganic ligands applied to CQDs were metal chalcogenide complexes (MCCs).[73] To passivate defect on the nanocrystals, passivating ligands should be small enough considering the steric effect of ligands coordinating to PbS nanocrystals. To gain effective passivation, a hybrid halide atomic ligand treatment was employed to reduce trap state density in PbS CQD films.[34] With iodide ligand surface passivation, the trap state density decreased to $2 \times 10^{16} cm^{-3} eV^{-1}$, and diffusion length increased to 70 nm.[64] In 2015, a new approach was announced by Carey *et al.*, and resulted in an exceptional diffusion length that recorded 230 nm.[9] The strategy in that study is to react each nanocrystal chemically to passivate themselves with other contiguous nanocrystals in addition to passivation by $CdCl_2$ and MPA.

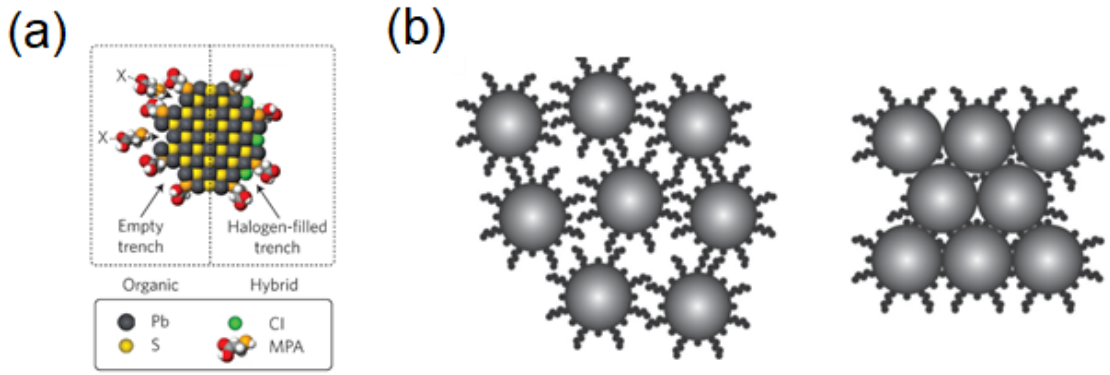


Figure 2.12: (a) Schematic diagram of PbS nanocrystal with only organic MPA ligand exchange/passivation (left-hand), and nanocrystal with both MPA and halide ligand exchange/passivation. While the organic-only passivation left some empty trenches on the surface of the nanocrystal, the halide treatment gives finer passivation. (b) Schematic diagram to illustrate how nanocrystals are partially fused from left-hand side rather loosely packed state to right-hand close-packing film.[9]

Although there are some exceptions, in general, shorter ligands facilitate better mobility of carriers in CQD thin films. This is observed for close-packing CQD thin film bifunctionalized with dithiols[19,74] such as 1,4-ethanedithiol (EDT) ligand and mercaptocarboxylic acid.[4] Not only the length but also the electronic characteristics of the ligands coordinating to CQDs change if QD behaves as an n-type or p-type semiconductor.[11,18,65,75,76] A surface dipole and the ability of ligands to withdraw electrons or to donate electrons make a drastic alteration of the band energy level of CQDs.[77] If the ligand has an electron donating dipole, both C.B. and V.B become shallower, and the film shows p-type behavior.[10] In contrast, if the ligand has an electron withdrawing dipole, both C.B. and V.B become deeper, and the film shows n-type behavior.

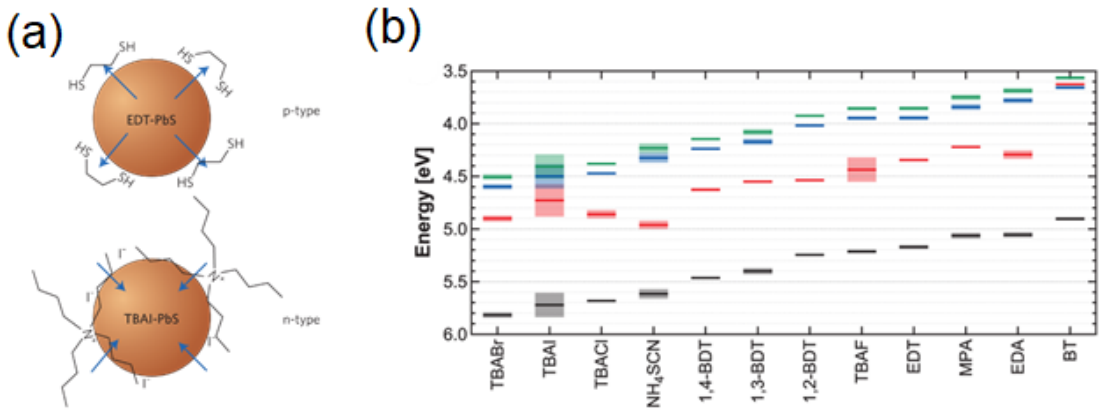


Figure 2.13: (a) Surface-bound molecules shift quantum dot energy levels (leading to p- or n-type behavior) by inducing variable surface dipoles.[10] (b) Energy level diagram of PbS CQDs exchanged with different ligands. Each column represents different ligand coordinating PbS CQDs which has E_g of 1.29 eV.[11]

Chapter 3

Literature Review

3.1 Structure of the Review

The first section of this chapter is focused on the synthetic methods and post-synthetic treatments of CQDs and their influences on the electronic characteristics of CQDs. Next, the state-of-the-art functionalizations of the CQDs by exchanging stabilizing ligands to shorter ligands would be introduced. This functionalization majorly rules the electric conductance energy levels of CQDs, and defect passivation. Finally, the architectural approaches explored to improve CQD PV efficiencies are summarized. Lastly, there would be a conclusion summarizing the highlight in the recent advancement of CQD PV technology.

3.2 Advancement in synthesis of PbS CQDs

3.2.1 Size distribution improvement in CQDs

Although the hot-injection method could synthesize monodisperse CQDs at a laboratory scale as described in section 2.2.2, Pan *et al.* have recently demonstrated that it is possible to modify this procedure to a dual stage batch process which accommodates large scale PbS CQD production without any compromise on quality.[78] Other research efforts have been geared towards avoiding the highly reactive and potentially dangerous sulfur precursor, bis(trimethylsilyl) sulfide ($(TMS)_2S$), and instead relied on elemental sulfur.[79–81]

Nevertheless, despite the high level of monodispersity achieved, to date, the V_{oc} of PbS CQD devices is limited to below half its band gap value.[82] Zhitomirsky *et al.* argued that V_{oc} improvement from monodispersity would only be significant if the PbS surface defect/trap density is reduced.[75] This highlights the importance of surface passivation for better device performance.

3.2.2 Size control in CQDs

On another front, there was a better understanding of the size effect on PbS CQD chemical stability. Intriguingly, PbS CQDs stability has been found to vary with its size.[83,84] While often portrayed as solid spheres, nanocrystals have a highly faceted structure dictated by their crystal structure. Small PbS CQDs have been reported to have a higher Pb:S ratio compared with the more faceted large PbS CQDs. In contrast, large PbS CQDs are more faceted, and they show exposed {111} facets consisting of sulfur anions not protected by common ligands like thiol and carboxyl-terminated ligands. Therefore, oxygen and other reactive species can easily attack these vulnerable {111} surfaces. The study of such a surface reaction is made possible by X-ray Photoelectron Spectroscopy (XPS), which shows the distinction between large and small PbS CQDs $PbSO_3$ is the primary oxidation product for small PbS CQDs, which gives a shallow trap state of 0.1 eV,[71,85] while that of large PbS CQDs is $PbSO_4$, constituting a deeper midgap state responsible for performance degradation.[83] Choi *et al.* further confirmed these observations as they synthesized batches of PbS CQD with diameters ranging from 1.5 nm to 7.5 nm and studied their composition, stability against oxidation, and shape evolution as size decreases (figure 3.1a).[12] Furthermore, the stability of CQDs was characterized by the extent of blue-shifts of the PbS excitonic absorption peaks, which was attributed to surface oxidation,[86,87] and this was shown to increase with decreasing PbS CQD size (figure 3.1b).

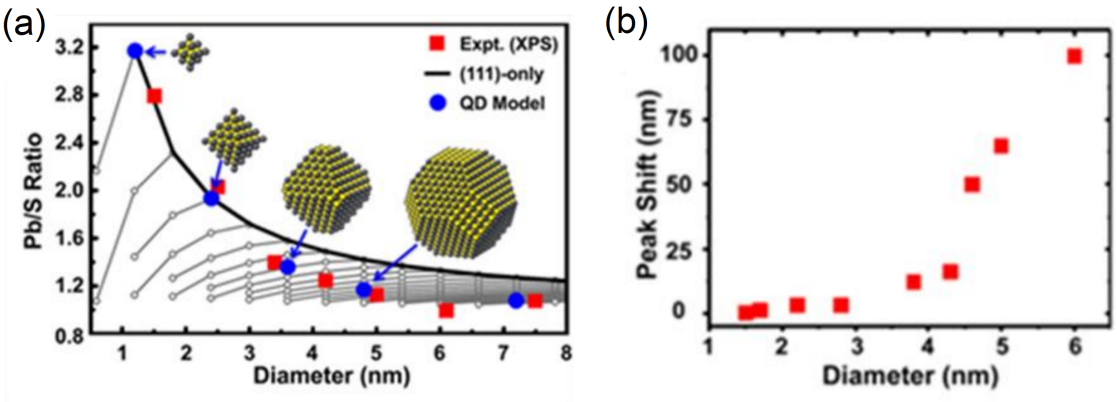


Figure 3.1: (a) Graph showing the relationship between the size of PbS CQD, its crystalline shape and cation to anion ratio, both simulated and backed by experimental data. (b) Plot revealing the size-dependent stability of PbS CQD to oxidation. The extent of the peak shift represents the amount of oxide shell formed on the PbS CQDs. (a) and (b) are reproduced from [12]

Therefore, the stability of a CQD and its surface passivation could be managed with materials engineering. The crystal facets vulnerable to oxiddation could potentially be avoided by synthesizing smaller PbS CQD, or even by developing a passivating strategy that binds to both cations and anions on the surface of the CQDs. However, the route of using smaller PbS CQD was shown to be counterproductive (see figure 3.2). [86] Some research groups have shown that Schottky solar cell devices with smaller PbS CQDs give higher V_{oc} due to the increasing band gap. [13,14] However, with increasing band gap (or decreasing PbS CQD size) the J_{sc} decreases because less light would be absorbed, and a higher series resistance was also reported due to more significant number of inter-QD hops that carrier has to make to travel across the same QD film thickness. Choi *et al.* evaluated that the stability towards oxidation only becomes apparent when the PbS CQD size is 3 nm (which equates to about 1.3 eV) or below. [12] Therefore, PbS CQDs should optimally be around this size to reap the benefit of both oxidative stability and a band gap size to capture a reasonable portion of the sunlight.

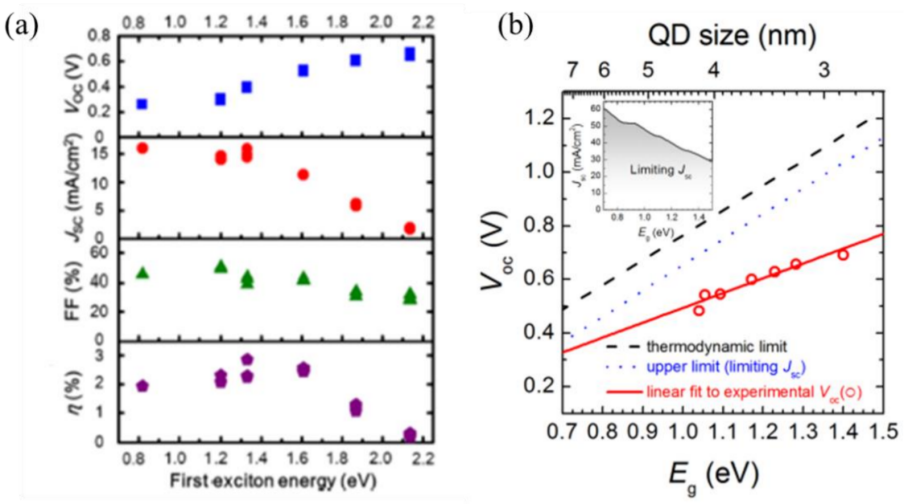


Figure 3.2: (a) Device performance metrics of Schottky solar cells against the size of the PbS CQDs used. In this study, the optimal band gap is found to be about 1.3 eV. Figure was reproduced from reference.[13] (b) The generalized relationship between band gap and experimental V_{oc}, theoretical V_{oc} (limited by a maximum of J_{sc}) and thermodynamical V_{oc}. This graph and the inserted graph show that it is unwise to gain V_{oc} by increasing the band gap because the gain in V_{oc} is limited while the higher bandgap suffers a loss in J_{sc}. Figure was reproduced from reference.[14]

3.2.3 Post-synthesis surface passivation

Another less common PbS CQD synthesis method is one that utilizes a lead chloride source, and Cademartiri and Ozin first developed this technique.[79] Moreels *et al.* later showed that this method could be adapted to produce a PbS size range widens that the hot-injection method is capable of.[81] A further step was taken by the effect of using different lead halides for synthesis, and they showed that the halide atoms are incorporated onto the synthesized PbS CQD.[62] Especially for the case of chlorides, the PbS product gave higher PL yield. They further report integrating the as-synthesised PbS CQDs into devices, which provided better device performance and higher stability as compared to controls. This treatment was understood as a way to treat and protect the surface of PbS CQD during the synthesis stage. Another unique approach is the use of metal chloride treatment during synthesis. First reported by Ip *et al.*, where cadmium chloride was introduced during the growth stage of the synthesis process,

it was shown as a method to ensure extensive trap mitigation as the small size of the halide atom is able reach trap sites that are not easily reached by bulkier organic ligands (figure 3.3a).[15] This was later generalized as a metal chloride treatment, where this time different metal cations have been studied (figure 3.3b) and it was found that the metal cation is essential in influencing the final energy states of PbS CQD and therefore influencing trap passivation.[16,88,89] Recent works from Zhang *et al.* followed by Crisp *et al.* showed the benefit of using both cation and anionic passivation by using lead chloride for a cadmium sulfide to lead sulfide (and also cadmium selenide to lead selenide) cation exchange synthesis procedure.[17,88] It was hypothesized that the cation exchange process leaves behind a certain amount of cadmium and chloride in the resultant PbS (and PbSe) CQD and devices made from the as-synthesized CQD showed better device performance and stability (figure 3.3c). In the following section, the techniques to passivate CQDs with ligand exchange during device fabrication are discussed .

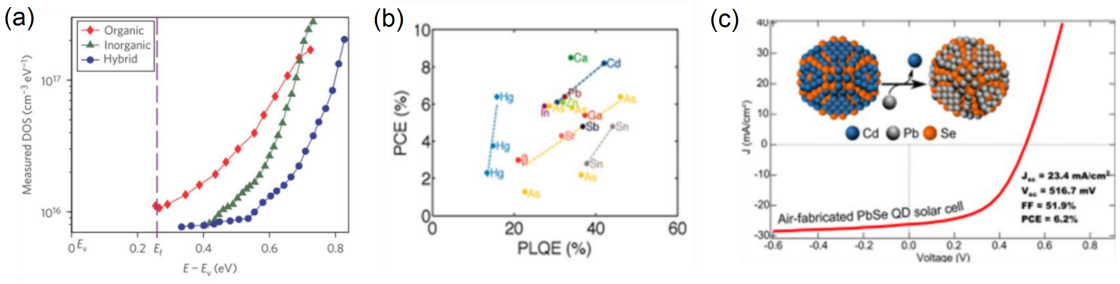


Figure 3.3: (a) Graph indicating better trap passivation by using a hybrid ligand exchange strategy. (b) The effect of different metal cations of metal chloride used in synthesis as a treatment procedure. Better PLQE is an indicator of better trap passivation. (c) Cation-exchanged PbSe (from CdSe) showing remarkable performance and stability and this same strategy was used for PbS solar cells. (a) is obtained from reference,[15] while (b) is from reference[16] and (c) is from reference.[17]

3.3 Advancement in functionalization of PbS CQDs

3.3.1 Two methods of ligand exchange

As stated in the previous section, the surfaces of CQDs should be passivated to protect them from oxidative attack and the aggregation of nanocrystals. However, to make PbS CQDs useful as an active photovoltaic material, long ligands attached to the CQD after synthesis needs to be replaced by smaller ones to increase the conductivity of the CQD film.[14] There are two general approaches in which ligands can be substituted, and they are pictorially illustrated in figure 3.4. The first approach (figure 3.4a) is termed solid-state ligand exchange and involves replacing the native ligands only after casting the CQD film. The second approach (figure 3.4b) is termed solution-phase ligand exchange, and it involves swapping the long native ligands for shorter ones while the CQDs are still suspended in a solution.

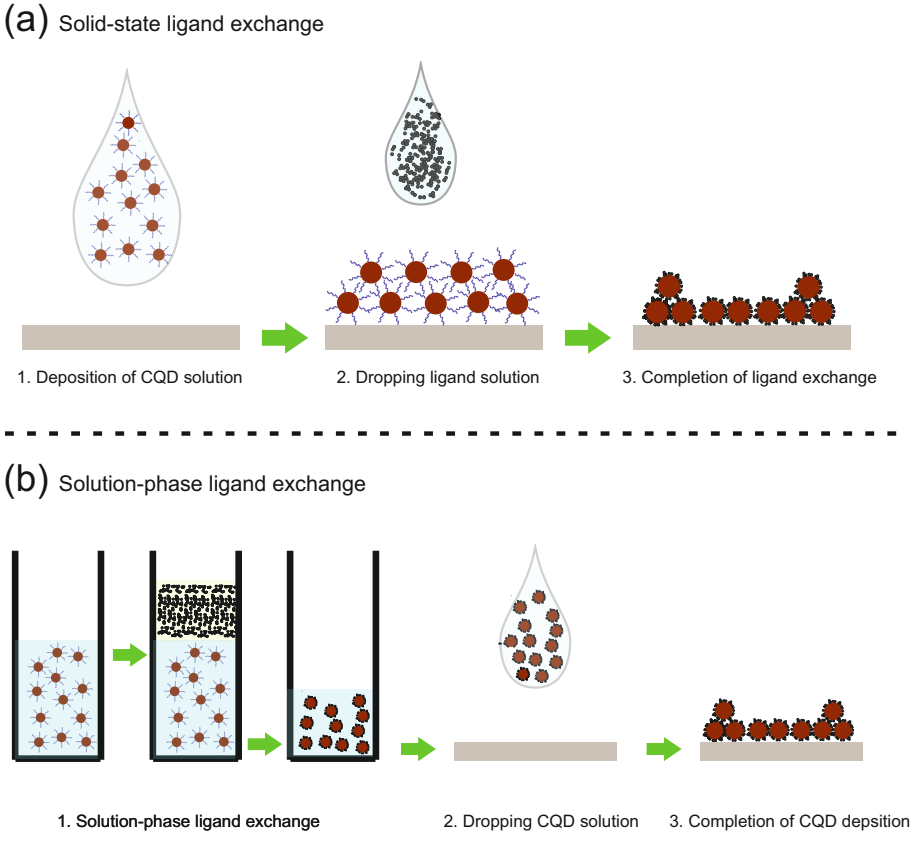


Figure 3.4: Schematic illustration of the (a) solid-state ligand exchange process, and (b) solution-phase ligand exchange process.

Solid-state ligand exchange is a more established method, and is usually integrated into the device fabrication process for example by spin coating or dip coating. The crux of the technique is the formation of a thin film of CQD on a substrate, followed by the introduction of the replacement ligands and the washing away of excess and exchanged ligands. However, because the replacement ligand is much shorter than the native one, the entire film would experience significant volume shrinkage, resulting in macro defects such as cracks and voids. This is remedied by using a layer-by-layer approach to the process of film deposition so ligand exchange is repeated several times until the desired thickness is achieved, with each new layer filling in the voids of the previous layers. This layer-by-layer casting and ligand exchange approach is still the most established method, and it is used to make the best devices reported in recent times.[23,90] While this technique seems attractive, it is dependent on exchange kinetics, and in some instances the exchange rate is slow. As an example from Tang *et al.*, the ligand cetyltrimethylammonium bromide (CTAB) exchanges slowly with oleic acid.[84] By putting a copious amount of ligand solution over the film and allowing the solution to stand for a minute before washing it off, and then by repeating the procedure twice more, they showed that this would ensure complete exchange before the next layer of CQD is deposited.[34] Although this technique is relatively reproducible under laboratory conditions, its scalability is questionable. For example, in a roll-to-roll production line, a layer-by-layer approach would be time-consuming and costly.

The second approach is conceptually more ideal, as a solution phase ligand exchange ensures adequate time for complete and thorough exchange of ligands. The number of deposition cycles of CQD layers could be reduced as voids would less likely be formed, and this would lead to less material wastage compared to a layer-by-layer procedure. Unfortunately, this procedure has its fair share of limitations when forming solar cell devices. First, the replacement ligands are smaller and so do not stabilize the colloidal state of the solution very well. Extra care must be taken with solution purity, the

inertness of the environment and temperature, especially with long exchange times, to avoid unwanted oxidation or contamination. Also, these small ligands are labile and might be lost during the coating process, forming new defects and energetic disorder. One of the first few examples of using this approach is work done by Johnston *et al.*, in which oleic acid was swapped for butylamine in PbS CQD.[91] The exchanged PbS CQD is re-dispersed in toluene and used to fabricate a Schottky junction solar cell. The device gave an AM1.5 efficiency of 1.8% and a monochromatic efficiency on 4.2% at 975 nm with a 12 mW cm^{-2} intensity.[15] However, it was reported that the devices were stable for only 4 hours and were utterly degraded when left out in ambient air for a day. There have been various solution-phase ligand exchange procedures reported since then, with metal chalcogenide complexes, chalcogenides, metal halides, and even pseudohalides as the exchanging ligands, but these studies have no reports of using the exchanged PbS CQD for solar cell devices. A significant milestone was reached when Fischer *et al.* reported the use of thioglycerol as a ligand.[92] PbS CQDs were successfully transferred from the octane phase to dimethyl sulphoxide (DMSO) phase and then was separated and used for solar cell device fabrication. However, due to the low volatility of DMSO, a non-conventional CQD film casting method was used, and it requires mild heating under a low-pressure condition for hours. Furthermore, device efficiency is at best 2.1%. Even though the results are not remarkable, this work serves as a proof of concept that a direct one-step deposited PbS could result in a working solar cell device. Tremendous progress was made recently, where iodine was used as a passivating ligand. Introduced as methylammonium iodide, PbS CQDs were transferred into dimethylformamide (DMF) solvent as stabilized by the iodide ligand.[18] This exchanged-PbS was cleaned and then re-dissolved in butylamine to give a highly concentrated volatile colloid which could be deposited by spin coating. Device fabrication was not only simplified, but devices were air-stable, and the best devices reported gave a power conversion efficiency of 6.1% (figure 3.5a-c).

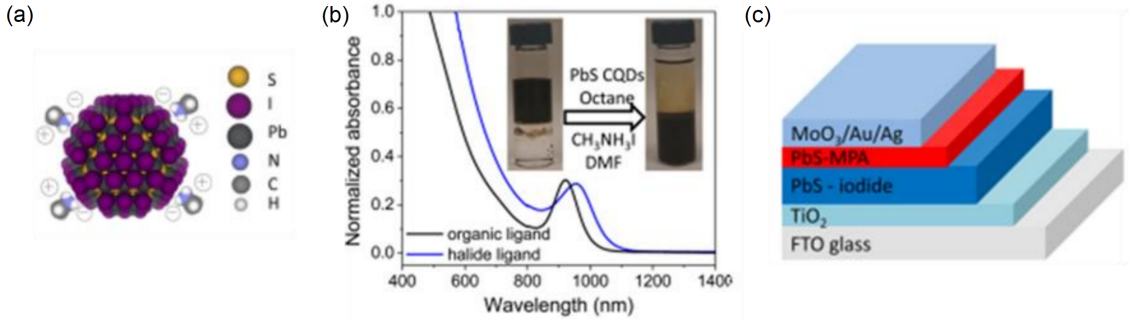


Figure 3.5: (a) A PbS CQD model depicting iodide ligands passivating the Pb rich PbS CQD surface and the methylammonium counterion balances the overall charge. (b) Absorption curve showing the presence of PbS CQD exciton peak before and after ligand exchange, which excludes any possibility of CQD aggregation during the process of ligand exchange. The slight red shift, however, is due to stronger coupling between CQDs due to closer proximity between CQDs with the smaller sized iodide ligands. (c) The device architecture which incorporates the iodide exchanged PbS CQD.[18]

3.3.2 Different types of ligands

The most obvious reason for employing ligand exchange is to decrease the inter CQD distances, thereby improving charge mobility. Talapin *et al.* investigated the effect of swapping oleic acid ligands for hydrazine on PbSe CQD films, showing experimental evidence for the reduction of interparticle spacing and a 10-fold increase in conductance, measured from field effect transistor (FET) experiments.[93] Similarly, Yu *et al.* showed that by replacing trioctylphosphine oxide ligands with 1,4-phenylenediamine, cadmium selenide CQDs conductivity by three orders of magnitude.[39] Furthermore, Liu *et al.* demonstrated a direct experimental observation of ligand length to carrier mobility in lead selenide (PbSe) nanocrystal solids,[19] and this is illustrated in figure 3.6.

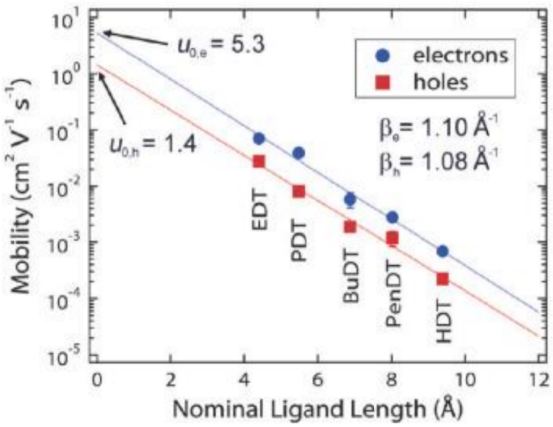


Figure 3.6: Carrier mobility showing an exponential dependence on ligand length. Mobility is extracted from Field Effect Transistor studies of PbSe CQD Films. Reproduced from reference.[19]

Bidentate ligands are one of the top choices for ligand replacement when it comes to device fabrication. These organic molecules could bind to one CQD and also a neighboring CQD, which effectively reduces interparticle spacing, making a very compact CQD film. The downside is that they could only be used in a solid state exchange process because applying them in solution causes the CQDs to aggregate. Also, the process generates voids in the film as the exchange of long ligands for shorter ones creates huge volume shrinkage, thus necessitating a layer-by-layer film formation approach. Nevertheless, their usage is quintessential for most of the current best performing PbS CQD solar cell devices.[23,90]

Ligand length is not the only consideration for ligand choice but also the passivating role of ligands, and in this case the chemical structure of the ligand (especially the attaching functional group) is crucial. Although organic ligands afford tunability due to the wide variety of structures available, another direction of development that is on the rise is the use of metal complexes as ligands. The methodology for incorporating them in CQD films was developed by Talapin and co-workers.[73,94,95] These inorganic ligands are small in nature and they are electrically charged. While traditional bulky organic chain-ligands render colloidal stability to CQDs in solutions via

steric hindrance, metal complexes, being electrically charged, confer CQD stability through electrostatic repulsion. This is a distinct advantage over other small inorganic ligands which do not provide the same stability in solution. After ligand exchange, the CQDs are very densely packed and FET measurements show that high carrier mobilities can be achieved. Perhaps the most fascinating feature is that when the CQD films with metal complex ligands are annealed, a unique heterostructure of a continuous metal chalcogenide matrix with CQDs embedded is formed.[73] Despite their promising attributes, metal complex-capped PbS CQDs were not used as active materials of solar cell devices until only very recently, where the first such PbS solar cell was reported, fabricated with a lead iodide perovskite complex.[96]

The last class of ligand studied comprises of small molecules or even atoms. Before halide ligands became popular, there was very little mentioned on the use of other small molecule ligands in PbS solar cell device fabrication apart from OH^-, administered as tetramethyl ammonium hydroxide, which was found to increase the p-type character of PbS[97] but notably increase trap density.[65] Recent work has shown the use of the thiocyanate ligand but it does not show any improvement over conventional cross linking ligands like MPA or EDT.[88] The advent of using halides as ligands came towards the end of 2011 in a notable work published by Tang *et al.*, which involves using bromine atoms as surface ligands on PbS.[34] The bromide ligand exchange not only improves mobility but was also shown to provide better passivation than organic ligands. Then solar cells made from PbS CQD with bromine ligand exchange gave the highest efficiency recorded for CQD solar cells at the time of publication. Attention then spread across the other halogens and most notably the use of iodine. Iodine ligand exchange has led to the formation of n-type PbS films, imparted remarkable air stability and is responsible for some of the highest efficiencies recorded for PbS solar cells at the time of publication.[23,65] Due to increased attention on halogen ligands, there was an increased effort towards understanding the effect of passivating ligands

on the properties of PbS CQD films.

As a ligand binds to the nanocrystal, surface energy states are altered, and the aim is to ensure that mid-gap states are eliminated. Other than passivating the surface, the ligand alters the optoelectronic properties of a quantum dot. Even with similar size/length, different atoms/molecular groups may induce different properties - ligands affect the charge transport properties of the CQD film in two crucial aspects: mobility and lifetime. As was discussed in section 2.2.3, improved CQD coupling would greatly enhance mobility. As for lifetime, it is correlated to trap state density and recombination rate, and the extent of passivation offered by the ligand affects this. Other than charge transport, ligands change the overall composition of the quantum dot,[98] and therefore they would affect the resultant distribution of energy levels and might affect the doping levels of the quantum dot.[99,100] Incorporating other elemental species into PbS, for example, different halides (Cl, Br, I) as ligands, gave a different extent of doping, as reflected by the PbS CQD film carrier concentration.[64,65] The notion that PbS CQD film is p-type has always been widely accepted till reports of the use of halide ligands on PbS CQD were made. FET measurement of halide exchanged-PbS CQD films[64,101] and successful fabrication of PbS p-n junction devices[97,101,102] both gave evidence of PbS CQD films displaying n-type characteristics.

To date, two major hypotheses have been proposed to explain such a phenomenon. The first is a simple argument on stoichiometry balance in a quantum dot. For exact PbS stoichiometry, complete filling of the valence orbitals resembles a closed electronic shell configuration and results in an intrinsic material. For the off-stoichiometry case, an excess of electrons populates the conduction band and results in n-type doping, while a lack of electrons and incomplete filling of the valence band results in p-type doping. As an example, in PbS when iodine substitutes for sulfur, to maintain charge neutrality this corresponds to an extra electron in the conduction band, that is, n-type doping. This framework was dubbed as charge-orbital balance and was formalized by

Voznyy *et al.* as a method to predict doping in colloidal quantum dots.[103] The second hypothesis involves surface-induced dipoles of the ligand species on the quantum dot, therefore invoking a change in absolute energy levels of the quantum dot. Brown *et al.* used a range of ligands with different dipole moments and then showed using ultraviolet photoelectron spectroscopy (UPS) a systematic shift of the PbS valence, conduction bands and Fermi levels with ligands of increasing dipole moments.[11] This set of experiments is crucial in showing that PbS energy levels are easily modified either by size, which influences the band gap, or by ligands, which affect the position of the band and Fermi levels. Also, shifting the Fermi level relative to valence or conduction band edges implies a change in doping level. While it is still inconclusive as to which hypothesis is more appropriate to describe the action of ligands on PbS CQD doping or energy levels, it is fair to say that there is a considerable improvement in the understanding of the surface chemistry of PbS CQD since the advent of CQD film processing. In the next part of this chapter, the advancement in device architectures to improve device performance will be discussed.

3.4 Advancement in PbS CQD PV device architecture

3.4.1 Planar heterojunction structure

Despite the advantages of Schottky junction PbS CQD solar cells, such as the simple fabrication process with a limited number of interfaces, they show limited device performance. Fermi-pinning places a limit to the upper bound for the open-circuit voltage regarding the bandgap of PbS CQD films. Also, the illuminated side of PbS CQD film is the opposite side of the film to the Schottky junction where the separation of excitons is more favorable. Therefore, the heterojunction architecture has been studied since 2009 for lead chalcogenide CQD solar cells,[104,105] and has recorded power conversion efficiency (PCE) of 3%. In 2010, the PCE of heterojunction PbS CQD photovoltaic de-

vice exceeded 5% with TiO_2/PbS or ZnO/PbS bilayer p-n junction architecture.[106,107] In these devices, the n-type semiconductor was deposited onto a transparent electrode and covered by p-type PbS CQD film by spin-coating. In that device structure, electrons are collected from the n-type semiconductor to a transparent electrode, and holes are collected from a p-type PbS film to a metal contact which has deep E_f to make Ohmic contacts. One of these devices was named as depleted-heterojunction solar cells, as the depletion region is illuminated in that device structure.[106] This device structure is remarkably better in terms of the utilization of the drift mechanism for the separation of excitons generated in the light-absorbing layer. Brown *et al.* inserted MoO_3 in between a p-type PbS CQD thin film and Au to mitigate the Schottky barrier between Au and PbS, in addition to the electron-blocking character of MoO_3.[107] Currently, a champion device structure for planar heterojunction PbS CQD solar cells is FTO/TiO_2/PbS/MoO_3/Au/Ag, which employed hybrid passivation with MPA, and $CdCl_2$, and recorded 7.0% PCE. This advancement is mainly owing to better passivation by organic-inorganic hybrid passivation reducing the trap state density of the PbS CQD thin films and giving longer carrier lifetime.[15] One detrimental point about the planar heterojunction device architecture is that the photoactive PbS CQD layer cannot thicken due to the limitation of its charge collection length. Charge collection length is the length that minority carrier generated by illumination at depletion region can be collected to the external circuit. It is governed by the depletion region width and the diffusion length of the CQD layer. The depletion region is where the built-in electric field drifts carriers, and the diffusion length is the length that charge carrier can migrate in a semiconductor without the assist by the electric field.

3.4.2 Bulk heterojunction structure

To thicken the photoactive layer to give better absorption, bulk heterojunction solar cells have been developed with several approaches. All approaches are aiming to increase the surface area of the heterojunction interface. This is expected to enhance

the charge collection length of junction with PbS CQDs. If charge collection length increases, charges can migrate to the contact even if the thickness of PbS CQD increases. The first approach is the use of mesoporous TiO_2 for the n-type semiconductor that has been developed by research on bulk heterojunction organic solar cells to form a three-dimensional interpenetrating network of donor and acceptor.[108] In that method, large TiO_2 particles (150-200 nm) were deposited on top of a thin TiO_2 layer with smaller TiO_2 particles (10-30 nm). With that mesoporous structure, improved absorption, EQE, and photocurrent at infrared wavelengths have been observed.[109] The second approach is to utilize lithographically defined nanopillar arrays,[110] porous templated wells,[111] or nanowire arrays[20] of the wide-bandgap n-type semiconductor to make directional transport. One advantage of the use of templated wires or wells is to design the spatial distance between each array. This attempt is to realize the optimized distance of photoactive layer in terms of charge collection length by maximizing the volume of that layer. However, there are some drawbacks of the bulk heterojunction structure. They may induce increased bimolecular recombination at the interface,[109] lower built-in voltage related to back recombination with the increased interface area, and the careful treatment to prevent leakage current in devices without an elaborate choice of processing and combination of the materials.[20]

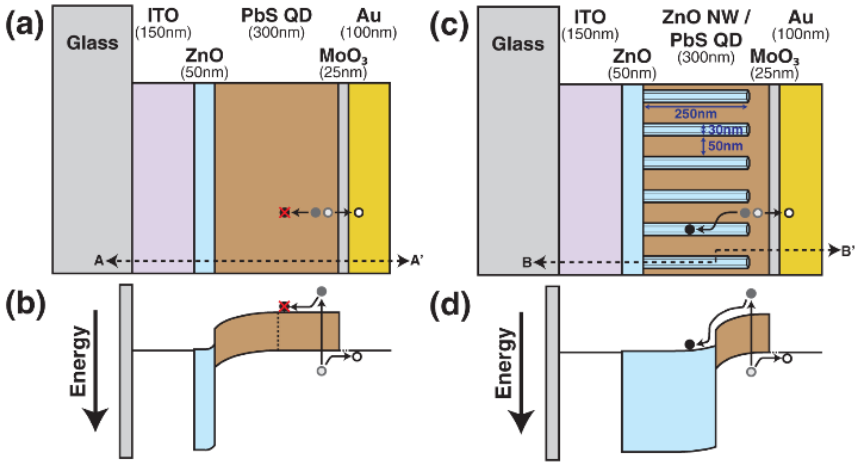


Figure 3.7: (a) Cross-sectional illustration of the planar heterojunction PbS CQD solar cell with 300 nm-thick PbS film which is thicker than the charge collection length. (b) Band diagram of the device illustrated in (a). This shows that the charge collection length is not long enough to complete charge transport from a single exciton pair. (c) Cross-sectional illustration of the bulk heterojunction PbS CQD solar cell with 300 nm-thick PbS film with ZnO nanowire arrays to shorten the pathways of electrons flowing from the PbS CQD layer to ZnO. (d) Band diagram of the device illustrated in (c). This shows that the path of electrons flowing from PbS to ZnO is shortened due to ZnO nanowire arrays. These are taken from reference.[20]

3.4.3 Multi-junction structure

Solar cell materials with different band gaps can be stacked and connected through ideal recombination interlayers betweeen different junctions to absorb more of the solar spectrum and exceed the Shockley-Queisser single-junction efficiency limit. The most sensitive part of the design of the structure is to find the right combination of the materials which fit each other according to band alignment engineering. For example, any interlayer that is in between two junctions should have an Ohmic contact for one layer to transport holes and for another layer to transport electrons. As discussed in section 2.1.2 and section 2.1.3, alignment with respect to the Fermi level is a significant factor. However, compared to multi-junction solar cells utilizing III-V materials, lattice-matching is not a decisive factor for PbS CQD photovoltaic cells.[112] Also, the quantum size effect of CQDs gives multi-junction solar cells with much sim-

pler choice of photoactive materials as size-tuning can be done by the alteration of the reaction temperature and the molar ratio of precursors. In 2011, Choi *et al.* reported multi-junction PbS CQD solar cells using ZnO and PEDOT:PSS with 1 nm Au for an interlayer.[21] Although inserting a thin metal layer helps to mitigate the potential difference between PEDOT:PSS as reported for organic multi-junction solar cells,[113,114] there is a considerable potential barrier made by the difference between the Fermi level of ZnO (approximately 4.3 eV) and Au (approximately 5.1 eV). This potential barrier makes an impedance to electron flow from the front junction (1.6 eV PbS) into the interlayer to recombine with holes flowing from the back junction (1.0 eV PbS). Considering that point, Wang *et al.* developed the graded interlayer with MoO_3, ITO, AZO, and TiO_2 for mitigating the potential offsets from PbS CQDs to interlayer as shown in figure 3.8a.[22]

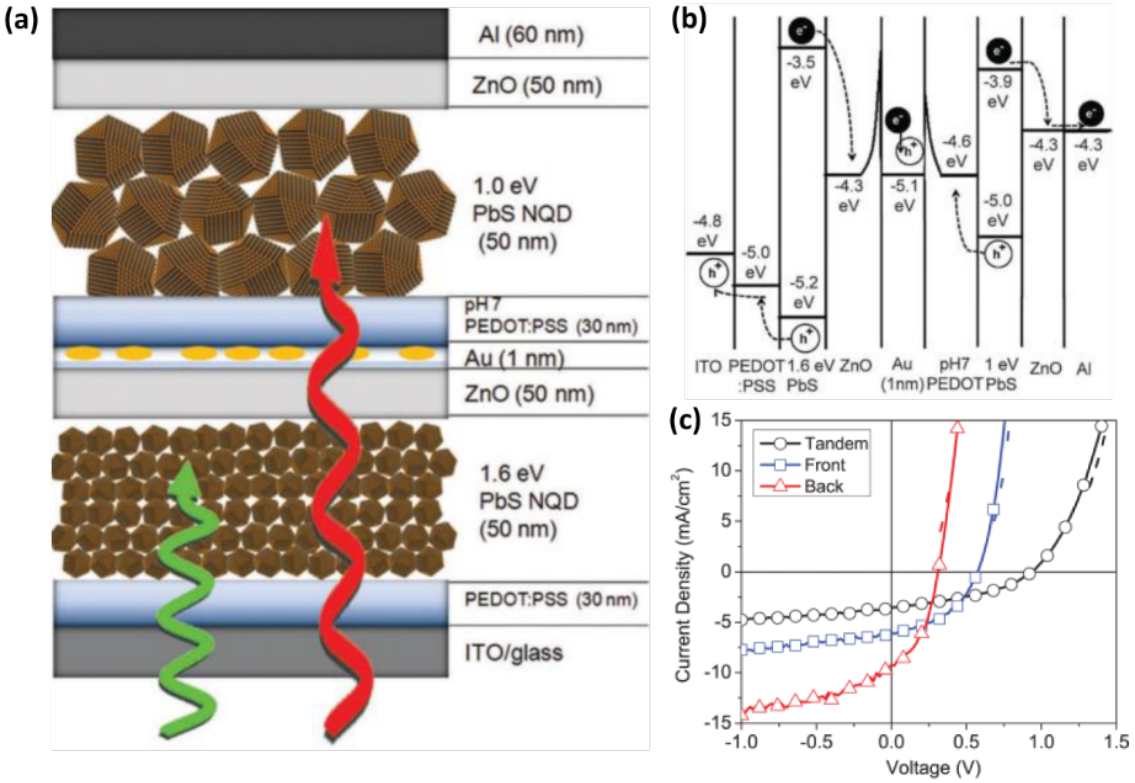


Figure 3.8: (a) Schematic cross-sectional diagram of multi-junction PbS CQD solar cell by Choi *et al.* (b) Band diagram of multi-junction PbS CQD solar cell illustrated in (a). (c) J-V Characteristic of solar cells from Tandem Solar Cells described in (a) of Front (PEDOT:PSS/1.6 eV PbS/ZnO/Al) and Back (PEDOT:PSS/1.0 eV PbS/ZnO/Al).[21]

Both approaches tried to optimize the performance of both front and back junctions in addition to the band energy modification, and they got an appropriate summation of V_{oc} in two junctions to the multi-junction structure. Overall, investigating the suitable combination of materials for interlayer is a pivotal part of the study on multi-junction PbS CQD solar cells.

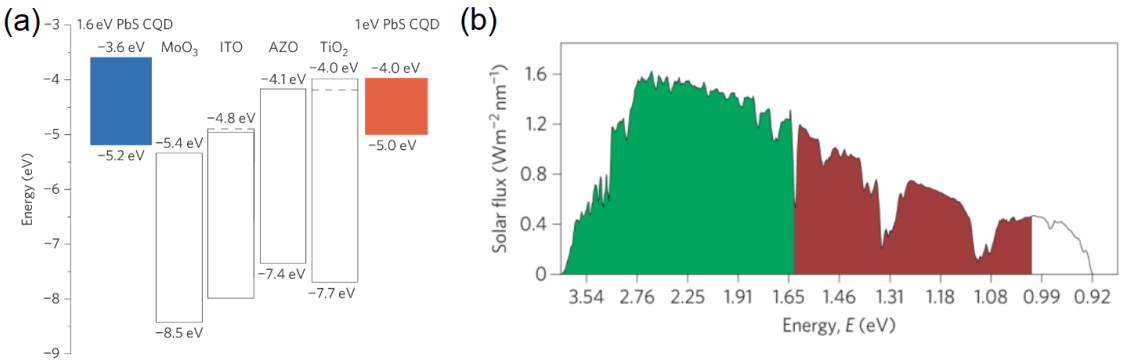


Figure 3.9: (a) Band diagram of multi-junction PbS CQD solar cells developed by Wang *et al.* (b) solar spectrum of AM 1.5 with the indication of the Energy absorbed by 1.6 eV PbS CQD absorbing layer (green-shaded) and by 1.0 eV PbS CQD absorbing layer (red-shaded).[22]

3.4.4 Band-alignment engineering

Ligand exchange is a significant process not only for improving the electronic properties of CQDs but also modifying C.B., V.B., and Fermi level of the nanocrystals as introduced in section 2.2.3 and section 3.2.2. Using various types of ligands, graded band alignment engineering has been studied to enhance the qE_f to have higher voltage via realizing graded p^+-p-n PbS-only junction solar cells,[101] p^+-p-n heterojunction solar cells,[115] and p-i-n heterojunction solar cells.[116] A p^+-p-n PbS-only junction solar cell consists of a thin and highly doped ($10^{19} cm^{-3}$) p-type PbS CQD layer with tetramethylammonium hydroxide ligand, a lightly doped ($10^{16} cm^{-3}$) n-type PbS CQD layer with a smaller amount of tetrabutylammonium bromide ligand, and a highly doped ($10^{17} cm^{-3}$) n-type PbS CQD layer with more substantial amount of tetrabutylammonium bromide ligand. Carrier extraction is supported by introduction of an enhanced

electric field due to the insertion of the lightly doped n-type layer which contributes to a more extended and graded depletion region. Consequently, the device could reach 7.4% PCE with better carrier extraction with high V_{oc} owing to the use of highly doped materials with a smooth and long depletion region.

In ZnO/PbS heterojunction solar cells, elaborate ligand treatments established a high PCE record of 8.55% in 2014.[23] To make an n-type PbS CQD thin film, tetrabutylammonium iodide (TBAI) was used (PbS-TBAI). Also, EDT was used for forming a p-type PbS CQD thin film (PbS-EDT). Utilizing the band bending due to the different band positions for both layers of PbS-TBAI and PbS-EDT, selective carrier transportation was achieved. PbS EDT has shallower C.B. and V.B. than PbS-TBAI, and therefore this band arrangement prevents the electrons flowing into the PbS-EDT and favored holes flowing into the PbS-TBAI. This selective carrier transport raises the fill factor to 0.6.

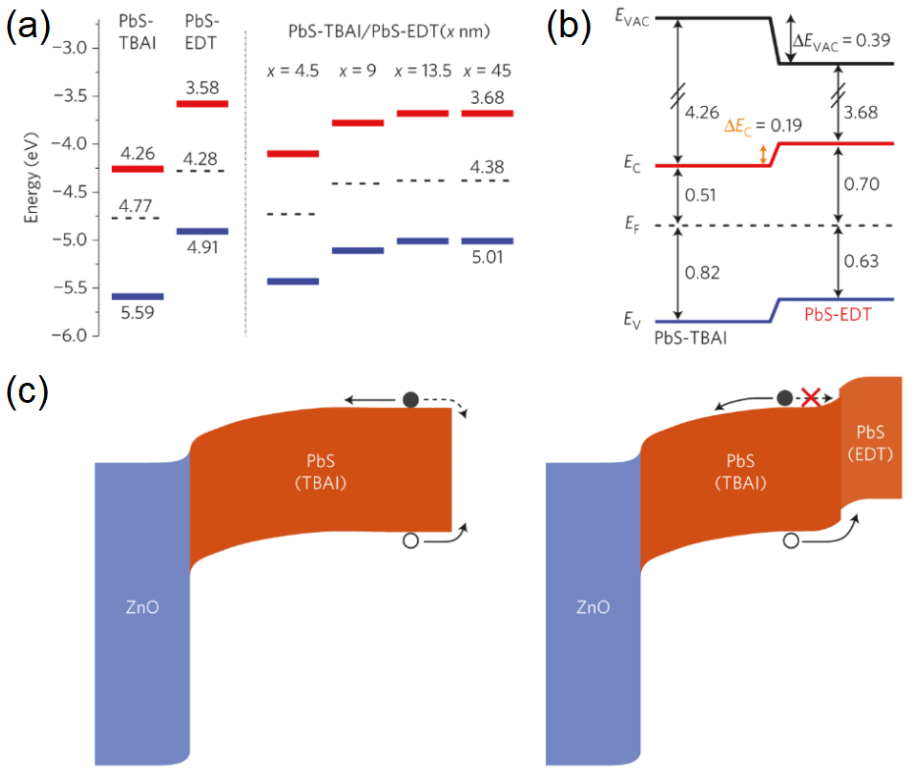


Figure 3.10: (a) Energy levels concerning vacuum for pure PbS-TBAI, pure PbS-EDT and PbS-TBAI films covered with different thicknesses of PbS-EDT layer. UPS determined the Fermi levels (Ef) and valence band edges (blue lines). The conduction band edges (red lines) were calculated by adding the optical bandgap energy of 1.33 eV, as determined from the first exciton absorption peak in the QD thin films. (b) Schematic energy level alignment at PbS-TBAI and PbS-EDT interfaces deduced from UPS, where E_{VAC} is the vacuum energy. (c) Schematic illustration of proposed band bending in ZnO/PbS-TBAI (left) and ZnO/PbS-TBAI/PbS-EDT (right) devices at short-circuiting conditions.[23]

3.5 Low dimensional carbon materials for electronics

3.5.1 Graphene

Graphene is categorized as a semimetal with its unique electronic characteristics thanks to its minute overlap between the valence band and the conduction band. That band energy feature in graphene is brought about by the peculiar allotropic form of carbon with sp^2-hybridization in the layer.[117] Carbon has an electron configuration $1s^2$, $2s^2$, $2p^2$. $2p^2$ can be interpreted as both $2p_x{}^1$ and $2p_y{}^1$ orbitals have an electron each,

and the p_z orbital is empty. To make a π-bonds to the other carbon atoms, the 2s orbital and two of 2p orbitals hybridize. As a result, there are three sp^2 orbitals and one 2p orbital with an electron in each. Those sp^2 orbitals are oriented perpendicular to the remaining 2p orbital (suppose that it is along the Z-axis), so sp^2 orbitals form symmetrical angles of 120° with each other in the X-Y plane. Those sp^2 orbitals becomes σ-bonds and remaining 2p orbital behaves as a π-orbital.[118,119] Regarding the bonding between carbon atoms in graphene, the σ-bonds takes an important role, and the σ-bonds in graphene layers are known to be stronger (615 kJ mol^{-1}) than sp^3-hybridized diamond (345 kJ mol^{-1}).[120] In terms of electronic conduction, an electron in a π-orbital has a strong influence, and bonding and anti-bonding states of that orbital dictate the electronic properties of the graphene layer.[121]

In reciprocal space, the graphene unit cell can be described by two basis vectors $\vec{a_1}$ and $\vec{a_2}$ as shown in figure 3.11a. Starting from these basis vectors and using the tight binding approximation, the band structure can be described using equation 3.1 where a_0 is the lattice constant, k_x and k_y are reciprocal lattice vectors, and γ_0 is the nearest neighbor hopping energy (generally in the range of 2.6-3.1 eV).

$$E(\vec{k}) = \pm\gamma_0\sqrt{1 + 4cos\frac{\sqrt{3}k_x a_0}{2}cos\frac{k_y a_0}{2} + 4cos^2\frac{k_y a_0}{2}} \tag{3.1}$$

The conduction and valence bands touch each other at the six corners of the hexagonal 1st Brillouin zone, known as the K points as shown in figure 3.11b. Near K points, the dispersion relation for graphene becomes linear ($E = \hbar v_F k$). The Fermi energy (E_F) of graphene is given by equation 3.2 where $n_{g,\,2D}$ is the carrier concentration in the two-dimensional graphene sheet, v_F is the Fermi velocity ($\approx 1 \times 10^6 ms^{-1}$).

$$E_F = \hbar v_F k_F = \hbar v_F \sqrt{\pi n_{g,2D}} \tag{3.2}$$

This linear dispersion implies that charge carriers in graphene behave as massless Dirac fermions.[117] This contributes to high carrier mobility in graphene layers.

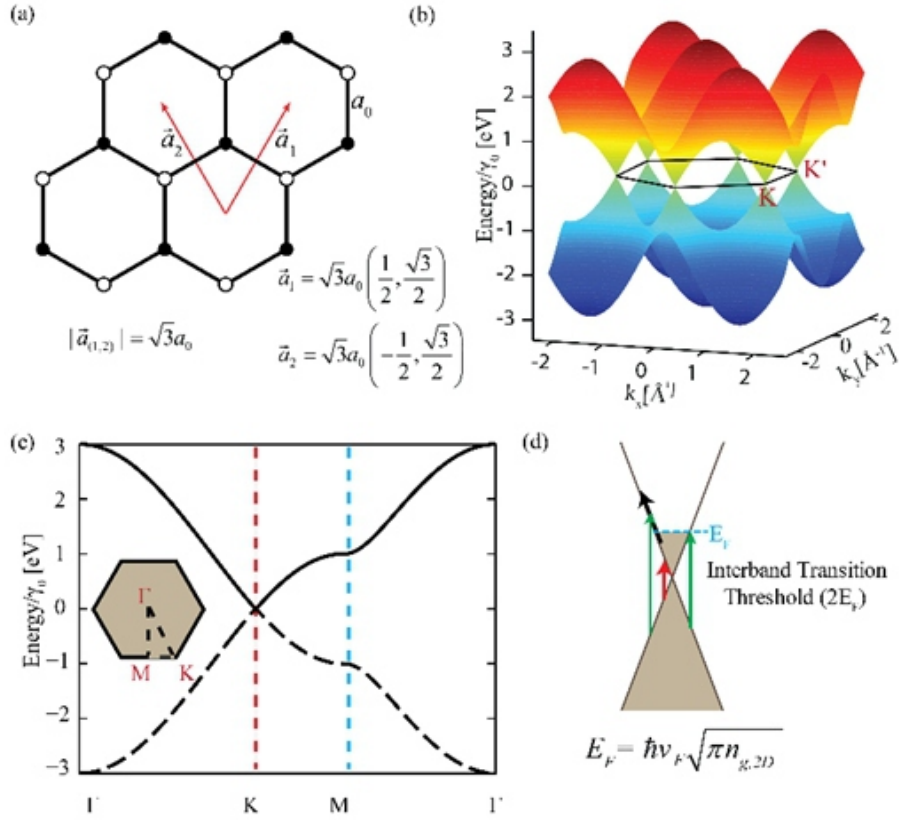


Figure 3.11: Electronic band structure of graphene: (a) Unit cell in reciprocal space showing the basis vectors $\vec{a_1}$ and $\vec{a_2}$ in terms of real space lattice constant a_0. (b) The E-K diagram for graphene calculated using the tight-binding approximation. The conduction and valence bands meet at the six corners of the hexagon in reciprocal space (known as Dirac or K points). The energy scale is normalized to nearest-neighbor hopping energy which is typically in the range 2.6 3.1 eV. (c) The simplified representation of the band structure of graphene using cut-lines along high symmetry directions. The band structure is linear close to K points giving rise to many unique properties of graphene. (d) Intraband and interband transitions in graphene, photons with energies above $2E_F$ will be absorbed due to transitions into the unoccupied states above the Fermi level.[122]

The optical transparency and conductivity of graphene can be exploited for many photonic devices. For example, liquid-crystal devices with electrodes made of graphene show excellent performance with a high contrast ratio.[123] Conducting films of graphene for solar cell applications can also be prepared by a bottom-up approach.[124] Polymer photovoltaic cells based on solution-processable graphene have been reported.[125] Also, graphene has been used as an electrode for water-splitting system, which suggests it

can be used as an electrode for fuel cells.[126] Because of its unique electronic structure, graphene shows useful photonic properties such as absorption of a significant fraction of incident white light[127] and strong, tunable interband transitions.[128] Above 0.5 eV, the absorbance of graphene is additive, resulting in strong graphene light interactions. This has made possible fabrication of FETs for ultrafast photodetection.[129–131] Solution-processed thin films prepared using graphene oxide enable easy material processing and mechanical flexibility, making them useful candidates for use in large-area devices. Figure 3.12 presents the schematic illustration of how graphene is incorporated in various electronic devices, including solar cells.

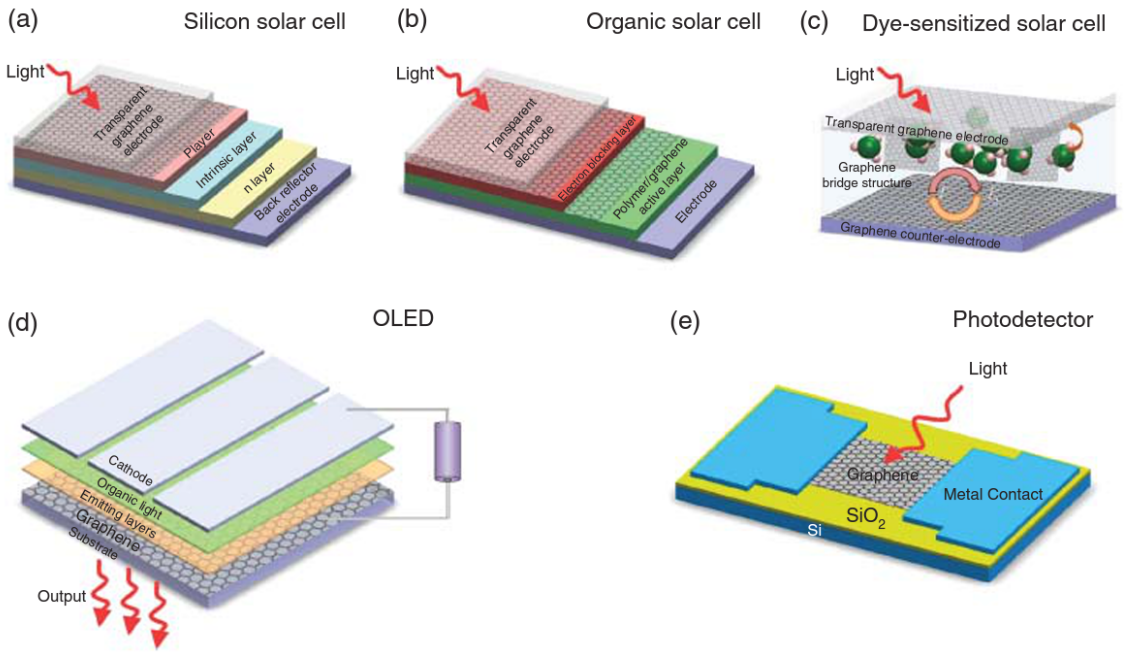


Figure 3.12: Schematic representation of graphene layers in (a) inorganic, (b) organic, and (c) dye-sensitized solar cells, (d) organic light emittting devices, and (e) a photodetector.[24]

3.5.2 Carbon nanotubes

SWNTs are graphene sheets rolled into a cylindrical shape with a nanometre-sized diameter,[132,133] and were found in the early 1990s.[134,135] SWNTs can exhibit either metallic or semiconducting characteristics depending on how sheets are rolled to tube

structures (i.e., how the allowed momentum states compare with the preferred directions for conduction).[136] Not only their excellent mechanical strength,[137] surface wettability, and thermal properties, but also their useful electrical properties make them intriguing for application in numerous electrical systems or devices.

Since the first electrical measurements on individual tubes in 1997-1998,[138] research has revealed that SWNTs have an extraordinarily high carrier mobility even over long lengths. For instance, Durkop *et al.* reported a field-effect mobility of 79000 $cm^2V^{-1}s^{-1}$ for a 325 μm length semiconducting SWNTs in 2004.[139] Javey *et al.* reported a high mobility of $4 \times 10^4 cm^2V^{-1}s^{-1}$ was measured in a 3 μm length of semiconducting SWNTs, and a 300 nm length semiconducting SWNT revealed ballistic conduction in 2003.[140] Ballistic conduction is the conduction of carriers when they are not scattered by lattice vibrations or impurities in a system. This conductive state is realized when the carrier mean free path (L_m) becomes longer than the tube length (L). L_m is the average distance carriers travel before their momentum is randomized by elastic scattering. In a non-ballistic state ($L > L_m$), transport will be diffusive if L_m does not substantially exceed the carrier phase relaxation length (L_ϕ). L_ϕ is the average distance that an electron travels before it experiences inelastic scattering which destroys its original coherent state. This length scale is an essential indicator of the transport properties of a nanotube.[141] With such intriguing electronic characteristics,[142] carbon nanotubes have been utilized for various electronic devices such as polymer solar cells,[143,144] perovskite solar cells,[145–147] and FETs[138,148] due to its very high carrier mobility.

3.6 Conclusions

In conclusion, this chapter has reviewed the research progress in PbS CQD photovoltaics, taking into account the understanding of how the synthetic and surface chemistry of PbS CQDs and the modification of the device architecture influence the performance of CQD photovoltaics. The significant findings from this review are:

(1) Synthetic approaches to obtain monodisperse PbS CQDs are essential, but advancements to have more monodisperse CQDs are less significant than reducing the surface defects on the PbS CQDs.

(2) Passivation of the PbS CQD surface is important to make the CQD thin films without trap states. Those trap states cause carrier recombination which degrades photovoltaic performance of PbS CQD solar cells.

(3) Ligand exchange processes to exchange stabilizing oleic acid ligands coordinated to PbS nanocrystals by shorter organic, inorganic, or hybrid ligands are important. This ligand exchange is has been the primary concern for lots of research to passivate the nanocrystal surface. Optimized ligand exchange also gives CQD thin films better charge transport performance.

(4) Finally, device architecture is very important to improve photovoltaic device performance. The limitation in terms of the diffusion length of CQD films can be dealt with different approaches in the device architecture. For example, the insertion of a hole transport layer, or a bulk heterojunction structure could be beneficial to strike the right balance of high absorption and improved carrier transportation.

(5) Low-dimensional carbon materials such as graphene or single-walled carbon nanotube perform superbly in electronic conduction due to their specific band structures. There are some electronic devices using those materials as an electrode or hole-transport layers.

Therefore, in this thesis, low-dimensional carbon materials were used as a hole-transport layer with various device architectures. First, the device utilizing a SWNT-P3HT composite in PMMA matrix was adopted as a hole transport layer in a PbS CQD solar cell. Next, a SWNT-P3HT composite was used as one component of a bulk heterojunction structure in a PbS CQD solar cell to improve carrier extraction with increasing PbS CQD film thickness. Last, monolayer graphene was employed as a hole transport layer in CQD photovoltaics.

Chapter 4

Basic Experimental Methods

4.1 Synthesis

4.1.1 PbS colloidal quantum dots

Synthesis of lead sulfide (PbS) colloidal quantum dots was carried out with the hot-injection method. In that method, the sulfur precursor hexamethyldisilathiane in a relatively cool solvent is injected to a hot solvent with a lead precursor lead oleate to bring about sudden nucleation followed by the growth regime in a gradual cooling process after the injection. To obtain a lead precursor solution, 2.1 mmol lead (II) oxide (99.0% from Sigma-Aldrich), and 5.7 mmol of oleic acid (technical grade 90% from Sigma-Aldrich) were stirred with a magnetic stir bar in 10 g of 1-octadecene (technical grade 90% from Sigma-Aldrich) for at least 2 hours at 90 °C in a flask under vacuum to obtain lead oleate complexes as lead precursors. After the lead oleate solution temperature was set to the desired level (typically 80 °C to 140 °C) regarding the targetted particle size of CQDs, 1 mmol hexamethyldisilathiane in 5 g 1-octadecene was injected to the flask under argon followed by ambient air cooling to room temperature for 1 hour. CQDs were purified by adding acetone, followed by centrifugation. The extracted CQDs were treated by twice of being re-dispersed in hexane and being precipitated by methanol, and then they were finally dispersed in octane with a concentration of 50 mg mL^{-1}.

4.1.2 ZnO nanoparticles

ZnO nanocrystals were synthesized by using the method according to Womelsdorf *et al.*.[149] 13.4 mmol of zinc acetate dihydrate was dissolved in 125 mL of methanol, and 26.9 mmol of potassium hydroxide was dissolved in 65 mL of methanol with stirring at 60 °C. Then, potassium hydroxide solution was added dropwise to the zinc acetate solution, and the solution mixture was stirred at 60 °C for 2.5 hours. The ZnO nanoparticles were treated by purification in methanol with centrifugation and decantation, twice. Finally, a mixture of 5 mL of chloroform and 5 mL of methanol was added to dissolve the precipitation.

4.1.3 SWNT-P3HT solution preparation

Single-walled carbon nanotubes(SWNT) wrapped by Poly(3-hexylthiophene-2,5-diyl) (P3HT) in a chloroform solution were prepared as a part of collaborative work by Dr. Severin Habisreutinger who was previously in the Department of Physics, the University of Oxford and currently in the National Renewable Energy Laboratory. The single-walled carbon nanotubes (SWNTs) used are SWeNT CG200 from Sigma Aldrich with a diameter range from 0.7-1.4 nm and relative purity of 90% as the percentage of carbon that is present as SWNTs. 3.0 mg of rr-P3HT (Rieke Metals Inc., weight-average molecular weight, Mw = 50000 g mol^{-1} and regioregularity = 95%) was dissolved in 5.00 mL of chlorobenzene and sonicated in a bath sonicator for 60 min. 2.5 mg of SWNTs was added, as purchased, to the dissolved polymer solution and treated with an ultrasonic probe for 10 min. The mixture was subsequently centrifuged for 8 min at 10000 g to remove nonfunctionalized SWNTs and other carbonaceous particles. The precipitates were discarded while the supernatant was recovered. To remove the excess polymer according to the solvent extraction technique detailed by Schuettforth *et al.*,[150] 15 mL of toluene was added. The mixture was then mildly heated for 60 min to induce aggregation of the functionalized SWNTs. The aggregates were precipitated

by centrifugation (4 min at 16000 g). After the centrifugation, the supernatant containing excess polymer was discarded, and the precipitate was recovered and dispersed in 5 mL of toluene. This mixture was then sonicated for 15 min in the ultrasonic bath to fully dissolve non-wrapped polymers. After the sonication, the mixture was mildly heated for 15 min to induce aggregation and then centrifuged for 4 min at 16000g. The supernatant with non-wrapped polymers was discarded. This procedure from bath sonication to centrifugation was repeated three times to remove all excess polymer resulting in the final supernatant being fully transparent. The final pellet consists of 2.0-2.2 mg of functionalized nanotubes was dispersed in 16 mL of chloroform. Immediately before spin-coating, the chloroform dispersion was sonicated with an ultrasonic probe for 2 min at low intensity (10% of amplitude) to break up clusters and bundles.

4.2 Characterization of colloidal quantum dots

4.2.1 UV-Vis-NIR spectroscopy

The bandgap of synthesized PbS CQDs was characterized by absorption measurements with a Varian Cary 5000 UV-visible-NIR spectrometer. The solution was distilled to 0.5 mg mL^{-1} with a solvent used to disperse the PbS CQDs in a quartz cuvette with 10 mm pathlength. The measurement has been done from 400 nm to 1200 nm after baseline and 0% calibration. The first excitation peak found in the absorbance spectra of PbS CQD was selected and converting the peak wavelength to energy in eV to calculate the bandgap of the PbS CQDs. The bandgap of other semiconductors, for example, SWNT-P3HT, were characterized from the Tauc plot from the absorption spectra.

4.2.2 X-ray diffraction

The crystal structure of PbS nanocrystals' surface was analyzed by a Rigaku Miniflex X-ray diffraction (XRD) setup. FIrst, PbS CQD film samples for XRD were prepared

by drop-casting on glass substrates. After confirming that the films were dried completely, measurements were taken. Diffracted X-rays are collected by the detector which sweeps through a range of angle and measuring the intensity or counts of the collected X-rays. The diffractogram of intensity versus angle gives information about the sample such as the identity of the phases present, composition and even the approximate size of the crystals.

4.3 Ligand exchange of colloidal quantum dots

4.3.1 Solid-state ligand exchange

Ligand exchange of colloidal quantum dots is the method to functionalize CQDs by exchanging long aliphatic oleate ligands by shorter organic ligands or inorganic halide ligands. Specifically, solid-state ligand exchange is done after drying a deposited layer of CQDs on a substrate to prevent CQDs' aggregation while removing the oleate ligands. In this thesis, all solid-state ligand exchange processes for PbS CQDs were done in the spin-coating method in ambient conditions with light. To exchange the oleate ligands of PbS CQDs to 1,2-Ethanedithiol (EDT) ligands, first 10 μL 1,2-Ethanedithiol ($\geq$98% from Sigma-Aldrich) was dissolved in 10 mL of acetonitrile from Fisher (HPLC for Gradient Analysis) to obtain a 0.1 vol.% solution of EDT in acetonitrile. Spin-coating was done at the spin speed of 2500 rpm. First, 10 μL of PbS CQDs in octane solution (50 mg mL^{-1}) was dropped on to the spinning substrate, and left to spin for 15 sec. Then 10 μL of EDT in acetonitrile solution of 0.1 vol.% was dropped on to the spinning substrate to exchange the oleate ligands by EDT ligands, followed by a rinsing step with 15 μL of acetonitrile to remove the remaining oleate ligands and excess EDT. This spin-coating process was repeated until the desired thickness of functionalized PbS was achieved.

4.3.2 Solution phase ligand exchange

Contrary to the solid-state ligand exchange process, solution phase ligand exchange is done in a liquid phase before depositing PbS CQDs onto substrates to dry. This was enabled without the aggregation by carrying out the ligand exchange reaction at the interface of two phases of different organic solvents. To exchange oleic acid lignads coordinating to PbS nanocrystals by methylammonium iodide, 0.8 mL of 50 mg mL^{-1} PbS CQD in octane solution was diluted in 4 mL of 10 mg mL^{-1} solution. The diluted solution was vigorously mixed with 5mL of 0.063 M methylammonium iodide (from Dyesol) solution in N, N-dimethylformamide (DMF) (99.8% from Sigma-Aldrich). After the PbS nanocrystals moved from the octane phase to the DMF phase, the solution was washed with octane three times. After decantation, 0.2 mL of toluene was added to precipitate CQDs. After 6000 rpm centrifugation for 10 mins, the supernatant was decanted and precipitates were dried under N_2 atmosphere. Precipitated PbS CQDs were dissolved in 160 μL butylamine. To exchange oleic acid ligands coordinating PbS nanocrystals by lead iodide and ammonium acetate ligands, 1 mL of 50 mg mL^{-1} PbS CQD in octane solution was diluted in 5 mL of 10 mg mL^{-1} solution. The diluted solution was vigorously mixed with 5mL of 0.10 M lead iodide (99.9% from Sigma-Aldrich) and 0.005 M ammonium acetate (98% from Sigma-Aldrich) solution in N, N-dimethylformamide (DMF) (99.8% from Sigma-Aldrich). After PbS nanocrystals moved from the octane phase to the DMF phase, the solution was washed with octane three times. After decantation, 0.2 mL of toluene was added to precipitate CQDs. After 6000 rpm centrifugation for 10 mins, the supernatant was decanted and precipitates were dried under N_2 atmosphere. Precipitated PbS CQDs were dissolved in 160 μL butylamine.

4.4 Characterization of semiconductor thin films

4.4.1 Fourier-transform infrared spectroscopy (FTIR)

For FT-IR measurements in this thesis, a Varian Excalibur FTS 3500 FTIR was used, and samples were scanned 64 times. All data in this thesis was taken in reflectance mode with an Excalibur FTS 3500 FTIR. Samples were prepared by drop-casting or spin-coating onto cleaned glass substrates to have a minimum thickness of 200 nm. This characterization was mainly done for confirming the effects of the ligand exchange process on colloidal quantum dots.

4.4.2 X-ray photoelectron spectroscopy (XPS)

X-ray photoelectron spectroscopy (XPS) is a surface-sensitive chemical analysis tool to identify the presence of a particular element and its bonding state (and oxidation state). It also can be used to extract quantitative data. The XPS spectrum is obtained by irradiating a sample with X-rays and then detecting and measuring the number and the kinetic energy of photoelectrons ejected from the sample due to X-ray excitation. These electrons are core electrons that have energies that are element specific, which enables elemental identification. The limitation of this technique is that it is surface specific; ejected photoelectrons only escape from the top 0 to 10 nm of the sample. Thermofisher K-alpha X-ray Photoelectron Spectrometer was used to take X-ray photoelectron spectra of various functional layers. XPS spectra were taken from 0 eV to 1350 eV of binding energy. Each sample was scanned 5 times at 0.1 eV resolution over the binding energy range of 0-1350 eV. The samples were charge compensated with an electron flood gun. An Aluminium K-alpha X-ray source with an excitation energy of 1486.6 eV is used. Casa XPS version 2.3.16 was used to analyze the XPS results. All XPS measurements were carried out by Dr. Philip Holdway in the Department of Materials, University of Oxford.

4.4.3 Scanning Kelvin Probe

Scanning Kelving Probe is a technique which relies on measuring a potential gradient between a sample and the probe that is used to contact the material. To measure the potential gradient between the sample and probe, an applied voltage ΔV_{sp} is varied till the flat band potential is achieved, which is identified by no current flow, then $e\Delta V_{sp}$ is the work function difference between the probe and the sample, where e is the elementary charge. To get the absolute value, the probe has to be calibrated first with a material of known work function. Work function data were taken by the KP Technology Scanning Kelvin Probe System 2001. For each sample, 25 values were measured for each of 3 arbitrarily chosen scanning points (75 values in total). At the beginning and the end of the analysis, measurements of reference samples (Al: work function of 4.1 eV, and Au: work function of 5.1 eV) were used to generate a calibration curve. This calibration curve converts raw data, which are relative work function values with respect to the work function of the scanning probe, to absolute work function data.

4.4.4 Transient absorption

Transient absorption measurements were performed using an amplified Ti:sapphire laser system operating at 1 kHz with pulses of about 100 fs. The excitation pulse was chosen at 800 nm (1.55 eV), while the probe pulse was selected from an optical parametric amplifier at 930 nm (1.33 eV), keeping its intensity about 10 times lower than the excitation pulse. To avoid multi-exciton interactions of colloidal quantum dots, which could influence our data analysis, the excitation intensity was chosen such that the average number of absorbed photons per nanoparticle is much less than 1. The samples were deposited on the SiO_2 glass. Mr. Gabriel Nagamine in the University of Campinas conducted all transient absorption measurements as part of external collaborative work.

4.4.5 Transmission electron microscopy (TEM)

Transmission Electron Microscopy (TEM) analysis was performed on a JEOL-JEM 2100 LaB_6 microscope with an information limit of 0.16 nm at an accelerating voltage of 200 kV. Samples were prepared by drop-casting nanotube dispersions onto lacey carbon film-coated copper grids.

4.4.6 Optical profilometry

Optical profilometry is the technique to characterize the surface of samples by measuring the interference of light illuminating the samples. An Omniscan MicroXAM 5000B 3d ADE phase shift interference contrast optical profiler was used for this measurement. After adjusting the focus and the angle of the samples, the equipment measured the area of 0.85 mm $\times$ 0.63 mm with 360960 sample points.

4.4.7 Ellipsometry

Spectroscopic ellipsometry data (measured at angles 45, 55 and 65 degrees) of CQD thin film (of thickness 160 nm) and other functional layers were measured using a Woollam RC2 Spectroscopic Ellipsometer (210 nm - 1700 nm). Data analysis for thickness and refractive indices was carried out in CompleteEASE software provided with the instrument. These derived values were utilized for simulation modelling.

4.4.8 Raman spectroscopy mapping

Raman spectroscopy detects the presence of specific bonds that vibrate or rotate at a particular frequency. This relies on the inelastic scattering of incident light. Some photons from the incident light interact with phonons (quantized molecular vibrations), resulting in the scattered photons having more or less energy. This shift in energy gives us the identity of a certain bond. Scattered photons are detected and collected to form the Raman spectrum. Raman spectroscopy analysis was carried out using a JY Horiba LabRAM ARAMIS imaging confocal Raman microscope. A 532 nm laser is used, and

its intensity is controlled to minimize sample damage. Each scan is averaged upon 8 co-scans for 30 second accumulation time. Raman shifts recorded by the equipment are calibrated with silicon substrates. The grating of the spectrometer was set to 1800 which gives finer resolution in a CCD detector. The mapping has been done with the scale of 35.9 μm $\times$ 39.3 μm with 110 scanning points.

4.5 Device fabrication

4.5.1 Etching ITO substrates

Etching ITO is done to determine the device pixel area in a precise manner. The etchant was made up of deionized water, concentrated hydrochloric acid, and concentrated nitric acid in the volume ratio of 50:45:5. After covering the area to retain the ITO with an adhesive seal, ITO coated glass substrates were immersed in the etchant held at 60 °C for 5 mins. The substrates were then dipped into cool deionized water, stripped of their adhesive masks and then washed again with deionized water. Figure 4.1 illustrates the schematic of this process.

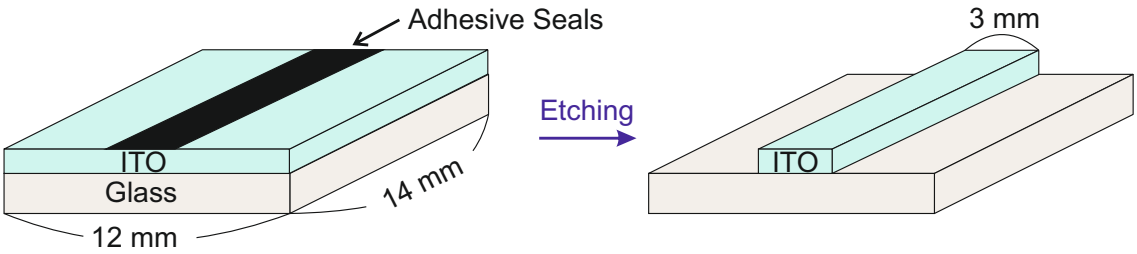


Figure 4.1: Schematic illustration of ITO etching with the 2D dimension of the glass substrates and ITO pattern after etching.

4.5.2 Substrate cleaning

After the ITO on the glass substrates is etched, the whole substrates were cleaned by ultrasonication and ozone cleaning, followed by deionized water with 2% Decon 90 detergent (Decon Laboratories), distilled water, acetone, and IPA in the ultrasonicator

for 15 minutes of 50 °C. Then, they were dried and transferred to the Ossila UV Ozone Cleaner, and cleaning was done for 15 minutes.

4.5.3 Spin-coating

First, ZnO nanoparticles were deposited on the substrates by spin-coating (2000 rpm for 30 secs) followed by annealing for 10 mins at 100 °C. After the deposition of ZnO, PbS CQD thin films were deposited either with solid-state ligand exchange, or solution-phase ligand exchange. For solid-state ligand exchange, spin-coating was done at a spin speed of 2500 rpm. First, 10 μL of PbS CQDs in octane solution (50 mg mL^{-1}) were dropped on to spinning substrate and left spinning for 15 sec. Then, 10 μL of EDT in acetonitrile solution of 0.1 vol.% was dropped to the spinning substrate to exchange the oleate ligands by EDT ligands, followed by a rinsing step with 15 μL of acetonitrile to remove the remaining oleate ligands and excess EDT. This spin-coating process was repeated until the desired thickness of functionalized PbS was achieved. To spin-coat the PbS CQDs after the solution-phase ligand exchange, 15 μL of PbS CQD solution in butylamine (200 mg mL^{-1}) was dropped on the substrates at a spin speed of 4500 rpm for 1 minute.200 μL of 0.12 mg mL-1 SWNT/P3HT solution in chloroform was deposited on the substrates dropwise at a spin rate of 3000 rpm immediately followed by a spin-coating of 20 mg mL-1 PMMA in chlorobenzene solution in air.

4.5.4 Top electrode deposition

After the deposition of the functional layers by spin-coating, the evaporation of top contact electrode was carried out in Thermal Evaporator Moorfield MiniLab T25M. After loading samples on to the sample holder, and the evaporation source into the tungsten boat, the evaporation chamber was closed and pumped to 5×10^{-6} mbar, and the metal source evaporated at a rate of 0.1-0.2 nm sec^{-1}. After the desired thickness was achieved, the current source was stopped and purge the evaporation chamber

purged with N_2 for 10 minutes. After purging, samples were ready to be taken out from the evaporation chamber.

4.6 Device characterization

4.6.1 Focused ion beam scanning electron microscopy

Scanning electron Microscope (SEM) imaging was performed using a Zeiss Nvision 40 FIB-SEM. Sample preparation for cross sectioning involved securing the glass substrate to a 12mm stub using carbon tape, followed by grounding the top contacts to the stub using conductive silver paint. To preserve the gold top-contact, e-beam deposition was performed prior to ion milling. Under a reduced raster from the scanning electron beam (5kV power, 120μm aperture, high current mode), a stream of C gas was passed over the sample for 5 minutes. A trench was milled with a 30kW/80pA Ga+ ion beam to a depth of 1μm. Images of the cross sections were taken using a secondary electron detector at 3kV using a 30μm aperture with the sample tilted to 36° from the normal. All FIB-SEM micrographs in this thesis work were taken by Mr. Daniel Gregory: a fellow D.Phil candidate in the same group.

4.6.2 Current and voltage (J-V) characteristics

J-V curve testing for photovoltaic devices was done in a chamber that was filled with flowing dry nitrogen gas and under a stable temperature of 25 °C. The pixel size of the solar cells was 3 mm^2, and there were three pixels on one substrate ($14mm \times 11mm$). Besides, an aperture was used to limit an illuminated area (1 mm^2) on the pixel that was smaller than the pixel size during the IV sweeps. For the illuminated condition, illumination was manipulated by a Newport solar simulator (Model 67005) with AM 1.5 filter. The intensity of the illumination is calibrated by an ABET Technologies Si reference cell (model 15151). This calibrated cell generates 100 mV output within the calibration accuracy of 6% at AM1.5G sun illumination conditions. The voltage sweep-

ing (dwell time 100 ms/step, sweeping speed 23 mV/step, sweeping direction reverse) were chosen. The scanning speed (dwell) was set to a relatively low value 100 ms/step to suppress the hysteresis observed for solid-state photovoltaics with halide ions in the system. To calibrate a light intensity with different distance between light source of the solar simulator and the sample holder, the V_{oc} values of ABET Technologies Si reference cell (model 15151) were measured with varying the distance from the light source and device holder chamber.

4.6.3 External quantum efficiencies (EQE)

EQE measurements were done in three steps; calibration of the photon flux with a Newport 818-UV and 918-IR calibrated photodiode, measurement with a white-light bias to have a fair measurement for an infrared region, and measurement without white-light bias to obtain a true signal level. The light source was generated by an Oriel Apex Monochromator Illuminator (Newport) and monochromated to a specific wavelength by an Oriel CornerstoneTM 130 1/8 m Monochromator (Newport). To cut off the undesired wavelengths of light, a Thorlabs FGL 400S Longpass Colored Glass Filter was used to pass light from 525-725 nm, and a Thorlabs FGL 610S Longpass Colored Glass Filter was used to filter the light noise below 700 nm, and an FGL 1000S Longpass Colored Glass Filter was used for allowing NIR light only. Signals were detected by a Keithley 6485 Picoammeter. To remove the signal corresponding to the white light in the EQE measurement with white-light bias, a Bentham 218 Variable Frequency Optical Chopper, and a Bentham 225 Programmable Lock-in Amplifier were used. The optical chopper was used to differentiate the signal excited by the light source with a chopping frequency from the signal excited by the white-light generated from a CVI Spectral Products Y1603 Cermax Xenon Fiberoptic Lightsource. After measurement with the white-light bias, measurements were done without white-light bias. The EQE data were adjusted with the signal response at a wavelength of 500 nm without white-light bias.

4.6.4 Integrating sphere reflectance measurements

The reflectance measurement were carrierd out using an ISP-REF Integrating Sphere. The samples were illuminated with from 400 nm to 1200 nm light, and all of unabsorbed light will be reflected to the ISP-REFs detector as the 100 nm Au back electrode is thick enough to have no transmission. Calibration of the baseline (100%) and 0% is done with the mask used for the measurement of photovoltaic devices to specify the device area. Measurements have been separated in two parts; 400-700 nm (visible light) and 700-1200 nm (NIR light), due to noise for NIR light. To reduce the noise, the exposure time for the NIR light measurements was set to 30 ms compared with 5 ms for visible light.

4.6.5 Electronic impedance spectroscopy measurements

Electronic impedance spectroscopy measurements were performed to explore the charge dynamics and measure charge transfer resistance values in the photovoltaic devices when the illumination was applied. In C-F measurements under illumination the higher frequency region reflects the series resistance, and lower frequency region depicts the charge transfer resistance. If a lower charge transfer resistance is observed in the impedance spectra this will suggest the charge transfer in the device is more efficient. An Agilent E4980A Precision LCR Meter was used to obtain impedance spectra of photovoltaic devices with 100 Hz-2 MHz frequency range and applied bias voltages from -1V to +2V. Samples were under 617 nm wavelength light illumination generated by a Thorlabs M167F2 fiber-coupled LED with intensity was set to achieve the photovoltaic devices to operate at V_{oc}.

Chapter 5

PbS CQD Solar Cells with SWNT-polymer Composite

5.1 Introduction

Efficient charge-selective layers adjacent to the absorber layers reduce voltage losses at the contacts and are also essential for improving the fill factor by balancing the transport of photogenerated electrons and holes and preventing the build-up of excess electrons and holes that results in charge carrier recombination. Furthermore, some of these charge transport layers show morphological changes at the interface of functional layer contacting electrodes which lead to an improvement of parasitic resistances through the suppression of the leakage current.[151–154] To date, efficiencies of CQD photovoltaics have not exceeded values of 14%[155] due to radiative and non-radiative recombination losses,[156] the misalignment of electronic levels at the semiconductor-semiconductor and metal-semiconductor interfaces,[157] and optical interference effects.[158,159] To overcome some of these limitations, and to improve the charge carrier transport from light absorber to the electrodes, this chapter investigates the use of single walled carbon nanotubes (SWNT) as a hole-selective contact. SWNTs are well-known for their mechanical and chemical stability[160] and, in particular, for their high electrical conductivity[139,140] SWNTs can have metallic or p-type semiconducting characteristics depending on their structure, namely their diameter and symmetry of the two-dimensional carbon lattice[161,162] In recent years, a number of reports have shown that by wrapping SWNTs

with conjugated polymers, processing challenges such as dispersibility and bundle formation can be overcome, thus opening the possibility to make use of the exceptional charge transport characteristics of SWNTs in different photovoltaics such as organic and perovskite solar cells.[147,163,164,164]

In this chapter, my collaborators and I use SWNTs which are wrapped in poly(3-hexylthiophene-2,5-diyl (P3HT) and coated by an insulating poly(methylmethacrylate) (PMMA) matrix as selective hole transporting layers at the interface between the PbS absorber and the top Au electrode. The power-conversion efficiency of the CQD-SWNT devices significantly outperforms that of control devices without the SWNT layer. I attribute the improvement in PCE to synergistic effects of the SWNT-PMMA layer as a charge-collection and optical spacer layer which leads to better light-harvesting and charge carrier extraction.

5.2 Results and Discussion

5.2.1 Device architecture and performance

Figure 5.1a shows a schematic of the device examined here, where all functional layers of the photovoltaic device are solution processed except for sputter coated indium tin oxide (ITO) electrodes on glass substrates and thermally evaporated gold as top electrode. On top of the ITO an electron transporting zinc oxide layer prepared by a sol-gel method[165] is deposited, and followed by a CQD absorber layer which is composed of PbS CQD stabilized by methylammonium iodide. Through the solution-phase ligand exchange process, the oleic acid (OA) ligands coordinating to PbS nanocrystals were exchanged by methylammonium iodide (MAI) ligands. Figure 5.1b exhibits the FT-IR spectra for PbS CQD film samples drop cast on glass substrates, and it confirms the ligand exchange process of PbS CQD photoactive semiconductor used in this chapter. For MAI PbS CQD thin film samples after the ligand exchange, the distinctive stretching and bending motion peaks for the N-H bonds were detected by FT-IR.[166]

This iodide ligand has been shown by Ning *et al.* to produce CQD films with higher charge carrier mobilities.[167]

Control devices have a direct contact between PbS CQD layer and the hole-extracting evaporated gold electrode. For the SWNT devices, the hole transport layer is processed by sequential spincoating first the SWNTs from chloroform followed by a PMMA layer from chlorobenzene. To determine the sheet resistance of the SWNT-P3HT in PMMA film, four point probe measurements were conducted. This measurement gave the result of 238±9Ω/square as the sheet resistance. In addition, surface analysis was carried out by the Omniscan MicroXAM 5000B 3d ADE phase shift interference contrast optical profiler. Figure 5.1c and figure 5.1d show the deviations in height from the average height of P3HT wrapped SWNT in PMMA and pristine PMMA layer. This surface analysis gave a root mean square roughness of 2.40±0.56 nm for P3HT wrapped SWNT in PMMA compared with 1.61±0.20 nm for the pristine PMMA layer. Finally, 100 nm of Au were thermally evaporated to form the top-contact.

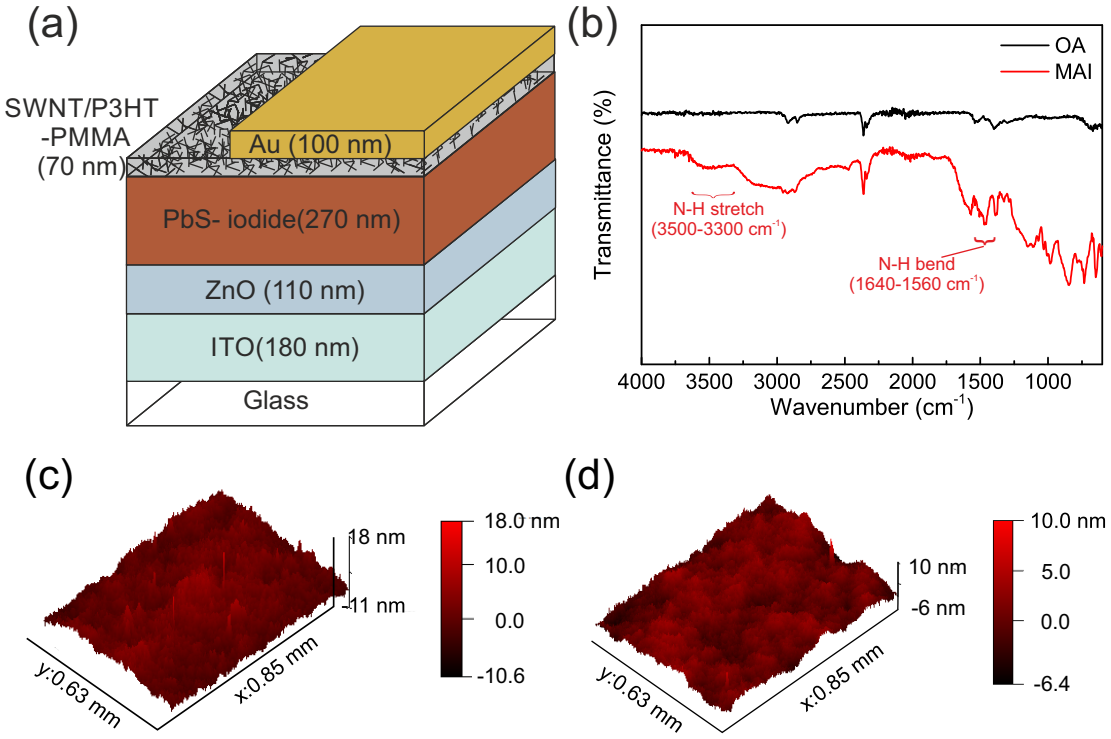


Figure 5.1: (a) Device structure of PbS CQD solar cells using SWNT/P3HT in PMMA matrix (70 nm) as a hole transport layer between light-harvesting PbS-iodide (270 nm) and Au (100 nm) cathode. (b) FT-IR spectra of colloidal PbS CQDs films on glass substrates before and after solution-phase ligand exchange from oleic acid ligand to methylammonium iodide ligand. Additional N-H peaks at 3500-3300 cm^{-1} and at 1640-1560 cm^{-1} appeared after the solution-phase ligand exchange that corresponds to the N-H bond in a methylammonium ligand. Deviation from the average height of the surface of (c) SWNT-P3HT in PMMA film and (d) pristine PMMA film over an area of 0.546 mm^{-2}.

A focused ion beam scanning-electron microscope (FIB-SEM) image of the device (figure 5.2a) shows a cross-section of the SWNT device, and a transmission electron microscope (TEM) image in figure 5.2b illustrates the size and aspect ratio of the SWNTs.

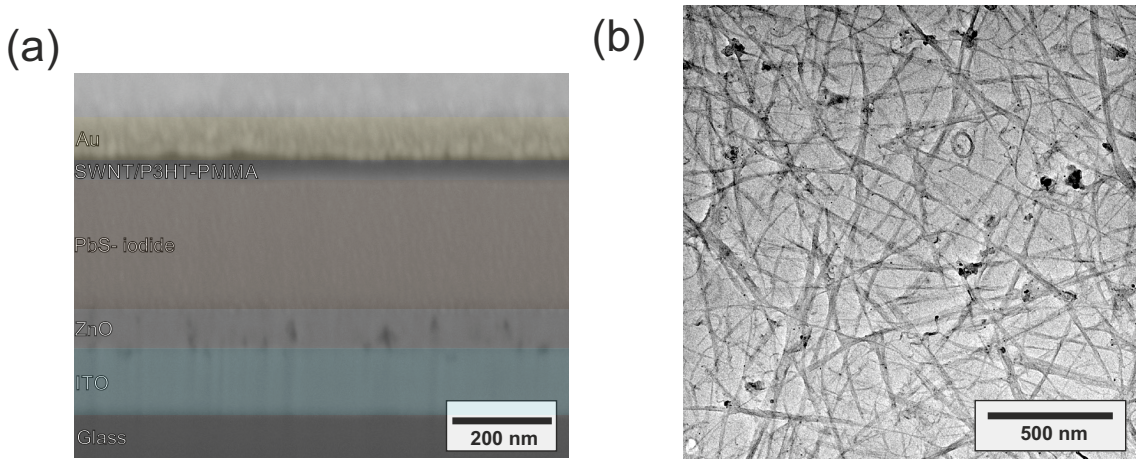


Figure 5.2: (a) FIB-SEM micrograph of cross-section of the device with SWNT/P3HT-PMMA. (b) TEM micrograph of spin-coated SWNT/P3HT.

Champion device current-voltage curves are shown in figure 5.3, comparing the performance with and without the SWNT/P3HT layer in addition to the device with P3HT only layer. As shown in figure 5.3, hysteresis of the J-V curves between the forward sweeps and the reverse sweeps was observed. This phenomenon has also been observed for perovskite solar cells that have methylammonium halides in their crystal compositions,[168–170] and the mechanisms ascribed to electrode polarization caused by the migration of I^- and MA^+ ions in the organometal halide perovskite.[171] The migration of ions can induce the interfacial electric or ionic charge accumulation[172] or band bending bringing about the non-steady-state photocurrent or J-V curve hysteresis. I expect similar effects to happen in the PbS photoactive layer with MAI ligands. Because the hysteresis of J-V curve is influenced by the rate of the scanning, I chose a relatively slow scanning speed (dwell) 100 ms/step.

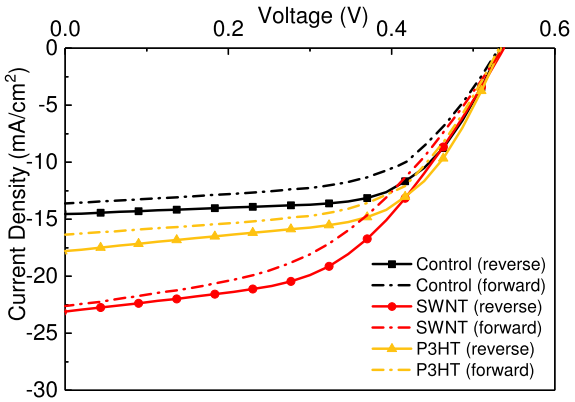


Figure 5.3: J-V curves for champion PbS CQD PV devices with SWNT/P3HT in PMMA (SWNT: red line with squares), without SWNT/P3HT in PMMA (Control: black line with circles), and with P3HT(P3HT: yellow line with triangles) in both forward bias (broken line), and reverse bias (solid line).

A statistical comparison of device performance is shown in Fig 5.4a-d. There is an overall improvement in the PCE by around 2.0% absolute when the SWNTs are included (SWNT devices in figure 5.5), while devices with P3HT only hole transport layer (P3HT devices in figure 5.5) did not exhibit as much performance improvement as SWNT devices did. This enhancement of device performance in SWNT devices arises from significant improvements (50%) in the short-circuit current density (J_{sc}). However, the FF values were slightly worse for the SWNT devices (nearly 10% relative loss) with a small increase in V_{oc} in comparison with controls. These results are contrary to P3HT devices which had higher fill factor values than control devices and slightly increased J_{sc} and V_{oc} values compared to control devices. A series of experiments were performed to understand the mechanism of the observed effects in SWNT and control devices.

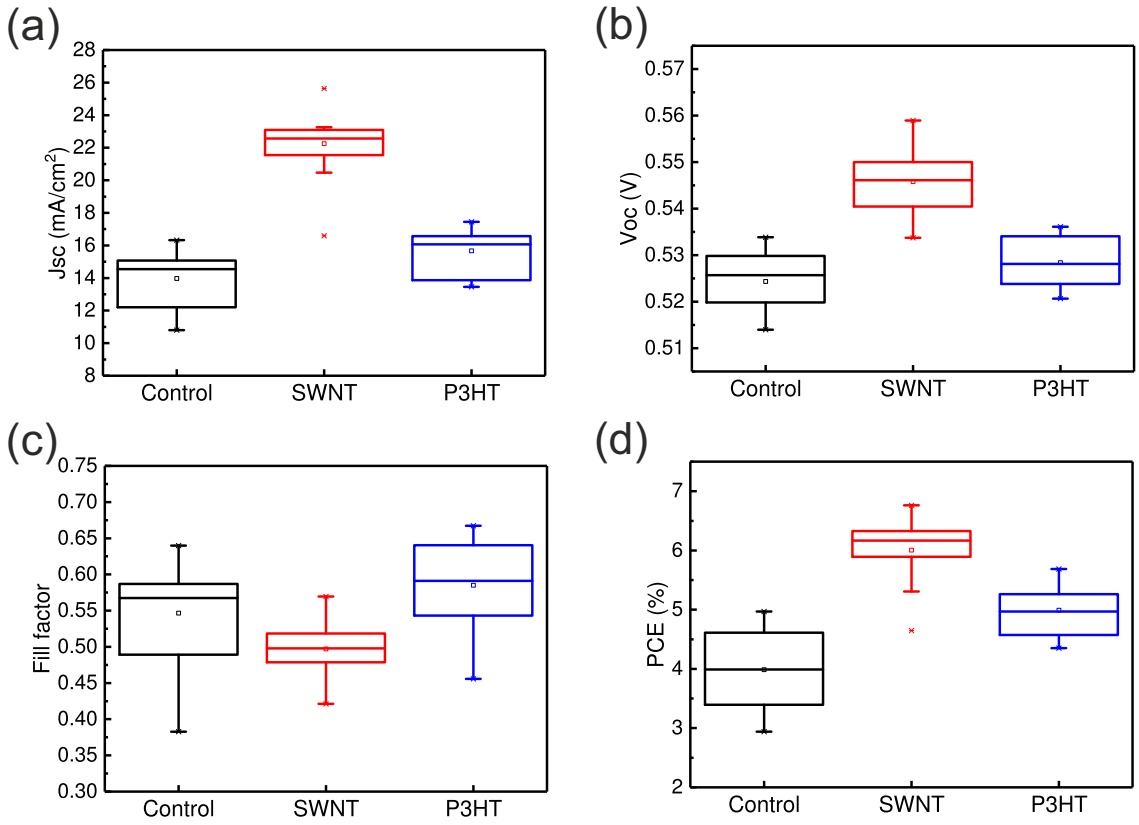


Figure 5.4: (a) J_{sc}, (b) V_{oc}, (c) FF, and (d) PCE of devices without SWNT/P3HT (Control in figure), devices with SWNT/P3HT (SWNT in figure), and devices with only P3HT at day 2 of storage in the air. Square symbols at the middle of the boxes are mean values. The upper lines, middle lines, lower lines of the boxes are representing 75^{th} percentile, median, and 25^{th} percentile respectively. Sticks cover maximum and minimum values excluding outliers that are outside the upper or lower lines. The reported mean values and percentiles for all parameters were calculated from a sample of 12 devices.

5.2.2 Charge transfer

In a photovoltaic device in which the terminals are connected without a load, the J_{sc} corresponds to the number of photogenerated charge carriers which are successfully extracted into the external circuit having evaded both radiative and non-radiative recombination processes.[173] In terms of charge carrier collection, the SWNTs were originally hypothesized to act as a charge-selective p-type transport layer which would minimize the formation of a space charge depletion layer at the Au electrode.[174]

How charges transfer from CQDs to SWNTs are described in figure 5.5, which

illustrates the cross-section of the PbS CQD layer and SWNT/P3HT in PMMA matrix. Figure 5.5 illustrates that the holes generated and separated in the PbS CQD thin film transport through carbon nanotubes accumulated on the CQD thin film, and conduct through the Au electrode. Due to the considerable gap between conduction bands of PbS-MAI and SWNT/P3HT, the coupling of electronic wavefunctions of two different materials will be the mechanism of the carrier transport between them.[175]

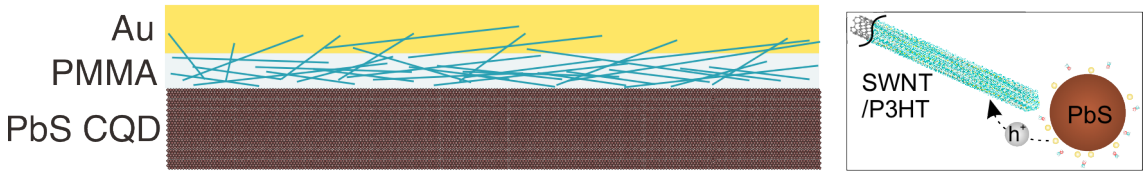


Figure 5.5: Cross-section illustration of the stacking PbS CQD, PMMA and Au layers. Carbon nanotubes are embedded in PMMA matrix and conduct holes from PbS CQDs to the Au electrode.

The nanohybrid system of P3HT-wrapped SWNTs should act as a selective hole transport layer, and this has been explored by both the valence band spectra from x-ray photoelectron spectroscopy (XPS) and the UV-Vis absorption spectra. First, a KP technology Scanning Kelvin Probe System 2001 was used to measure the Fermi level of the P3HT wrapped SWNTs. For each sample, 25 measurements were taken at three arbitrarily chosen points on the sample. The instrument was calibrated using aluminium and gold films. As a result, the Fermi level of P3HT wrapped SWNT was determined to -4.96±0.01 eV. Next, the valence band spectrum was used to determine the valence band position relative to the Fermi level determined by the Kelvin probe. Thermofisher K-alpha X-ray Photoelectron Spectrometer was used to obtain the valence band spectra of SWNT-P3HT thin films with 1486.7 eV x-rays. The XPS valence band spectrum in figure 5.6a shows that the energy difference between the Fermi level and valence band edge is smaller than 0.60 (±0.07) eV. Finally, the bandgap of the CQD and SWNT/P3HT were determined by a Cary Varian 4000 UV-vis-NIR spectrophotometer. The UV-vis-NIR spectrum in figure 5.6b shows the absorption peak at

568 nm which corresponds to an optical band gap of 2.18 eV. By integrating these three measurements, I conclude that P3HT wrapped SWNT has a Fermi level of -4.96 eV, a valence band maximum of -5.56 eV and conduction band minimum at -3.34 eV respectively, as presented in figure 5.6c showing the band positions of the functional layers in the SWNT devices. Due to their p-type character, the P3HT-SWNTs provide a more favourable extraction pathway for photogenerated holes from the PbS CQD absorber as opposed to photogenerated electrons. In contrast to the non-selective Au electrode, the SWNT layer should therefore facilitate selective charge extraction, which would result in a reduction in non-radiative recombination at this interface (see figure 5.6c). In the actual devices, both semiconductor-electrode contacts have ohmic contact, and all heterojunctions have type-II heterojunction configuration.

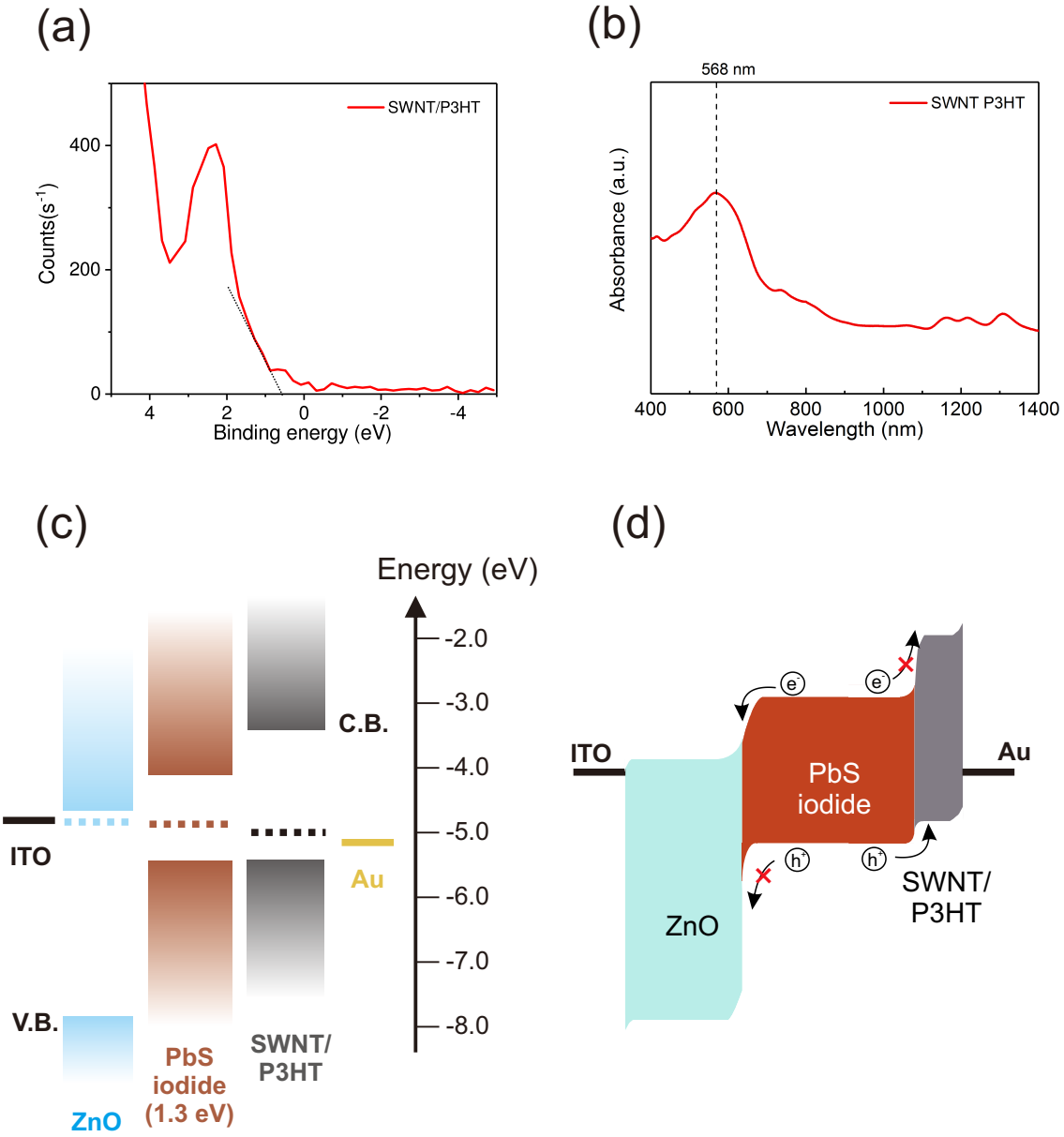


Figure 5.6: (a) a XPS valence band sepctrum of a SWNT-P3HT thin film. (b) UV-Vis-NIR sepctrum of SWNT-P3HT thin film. (c) Conduction band, valence band and Fermi level of materials used in the device stack. The Fermi levels of the semiconductors are represented as dotted lines, and the Fermi levels of conductive electrodes (ITO, and Au) as solid lines. (d) Schematic illustration of band bendings in the planar and bulk heterojunction devices.

However, the fill factor of devices containing SWNT was lower than control samples as shown in figure 5.5c. The factors which can negatively impact device performance, especially the fill factor, are the formation of a space charge layer at one of the elec-

trodes due to increased charge carrier recombination,[176,177] reverse saturation current and parasitic resistances.[178] To examine the cause of charge carrier recombination, measurements of V_{oc} under different white light intensities (figure 5.7a-c) were carried out. The dependence of V_{oc} on light intensity is expected to reflect both monomolecular and bimolecular recombination as all of the charges recombine under open-circuit conditions.[179] Figure 5.7c presents the plot of V_{oc} *versus* natural logarithm of the light intensity for both control and SWNT devices. The slope of that plot gives kT/q for both monomolecular and bimolecular recombination.[180] If monomolecular recombination is operative in addition to bimolecular recombination, a slope greater than kT/q is observed.[181] In figure 5.7c, the SWNT device has shown 2.88kT/q which is bigger than 2.25kT/q from the control device. This implies that the imcorporation of SWNT/P3HT allows monocolecular recombination to occur more readily than bimolecular recombination. This indicates that recombination due to trapping sites for either holes or electrons has a stronger effect after introducing the SWNT/P3HT in PMMA layer. Possible trapping sites will be at the interfaces between PbS CQD or P3HT and the PMMA matrix which localizes some charge carriers and facilitates recombination with free charge carriers.

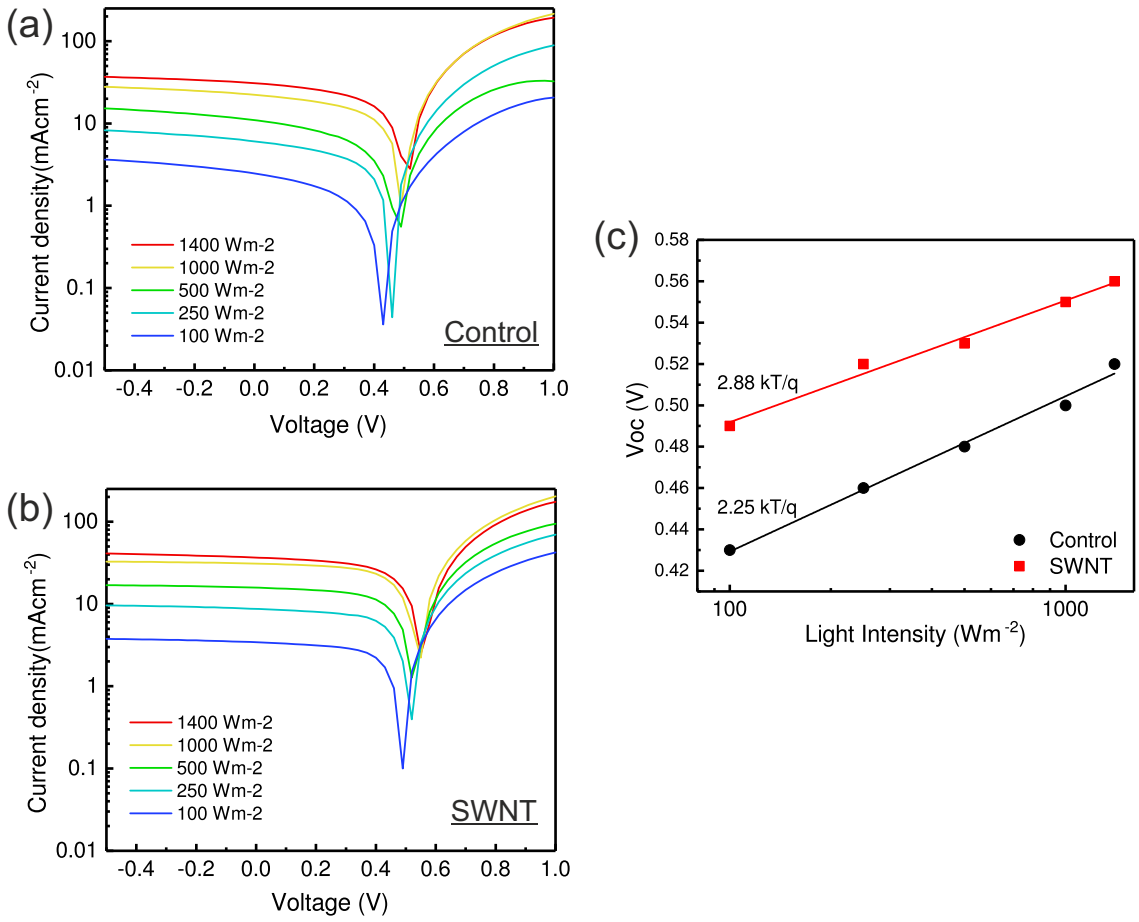


Figure 5.7: Plot of the logarithm of current density *versus* voltage under a light intensity of 1400 Wm^{-2}, 1000 Wm^{-2}, 600 Wm^{-2}, 250 Wm^{-2} and 100 Wm^{-2} for (a) control device and (b) SWNT device. (c) V_{oc} of the control device (without SWNT: red and square symbols) and SWNT device (with SWNT: black and circles symbols) under different illumination intensities. The slope of the linear fitting to V_{oc} *versus* logarithm of light intensity was analysed as the factor to the thermal voltage.

To probe the charge transfer dynamics, my collaborator Mr. Gabriel Nagamine in the University of Campinas conducted ultrafast transient absorption (TA) measurements as part of external collaborative work. The measurements were done on samples of 270 nm PbS iodide CQD thin films on glass with and without the SWNT layer, and PbS CQD films with oleic acid ligands on glass. These samples were without Au electrodes, and thus optical enhancement caused by light reflected by Au electrodes, which will be discussed later, was negligible in these measurements. These measurements should be able to probe the charge transfer kinetics from CQD to SWNT following

the light absorption in the CQD layer at picosecond time scales. The samples were pumped with a pulse at 1.55 eV, and probed with a weak probe beam at the energy of the first optical transition peak of PbS CQD (1.30 eV). The probe beam was chosen at 1.30 eV in order to monitor exclusively the electron and hole population at the PbS QDs band edge state, excluding the influence from higher lying states and intraband cooling dynamics. To minimize the influence from the fast dynamics due to multi-exciton recombination, the pump intensity was kept at a low level such that the average number of absorbed photons per CQD was $\langle N \rangle \approx 0.1$ corresponding to a flux of 10^{22} photons s^{-1} m^{-2} which is slightly higher than the photon flux for AM 1.5 (4.3×10^{21} photons s^{-1} m^{-2}), but still in the low excitation regime. As shown in figure 5.8a, in this low pump intensity regime oleic acid (OA) coordinated PbS CQD have extremely long charge carrier relaxation times. An initial small fast decay signal for the OA capped sample is observed, and is fitted to a lifetime of 17±1 ps. This value corresponds to the biexciton Auger lifetime for PbS CQDs with a band gap at 1.30 eV,[182,183] and this is confirmed by pump fluence dependent studies as shown in figure 5.8b. When oleic acid is replaced by methylammonium iodide, which is a short chain ligand, the excited carrier may hop to other nanocrystals, and as a consequence the lifetime becomes much shorter. The dynamics may be fitted by a single exponential decay of 210±30 ps (accounting for nearly 85% of the decay), meanwhile the long lived plateau accounts for only about 15% of the signal. By incorporating the layer of SWNTs on top of the CQD layer, he observed that an even faster component emerges, and a bi-exponential decay is necessary to fit the data. The fastest component is 25±4 ps, accounting for 45% of the decay, while the slower component is kept constant, but accounts for only 46% of the amplitude. Meanwhile, the long lived plateau is about 9% of the total dynamics. The fast decay observed on the transient absorption experiment for the OA capped sample (in figure 5.8a) is due to the presence of a small biexciton population. To show that, and to measure the biexciton Auger lifetime for this sample,

he has repeated the experiment for different pump fluences and for a shorter dynamic range (100 ps). figure 5.8b shows the results. Fitting these data assuming a monoexponential decay and a plateau, he estimated that the fast component, which increases with the pump intensity, has a lifetime of 17±1 ps. This is in agreement with the literature value for biexciton Auger recombination for PbS quantum dots with band gap at about 1.3 eV.[182,183] These results suggest that the fast component is due to fast charge extraction and transport from CQD to SWNT. This reduction in relaxation time in the presence of SWNTs indicates that photogenerated charge carriers are now transferred more rapidly from the CQD films to the SWNT layer.

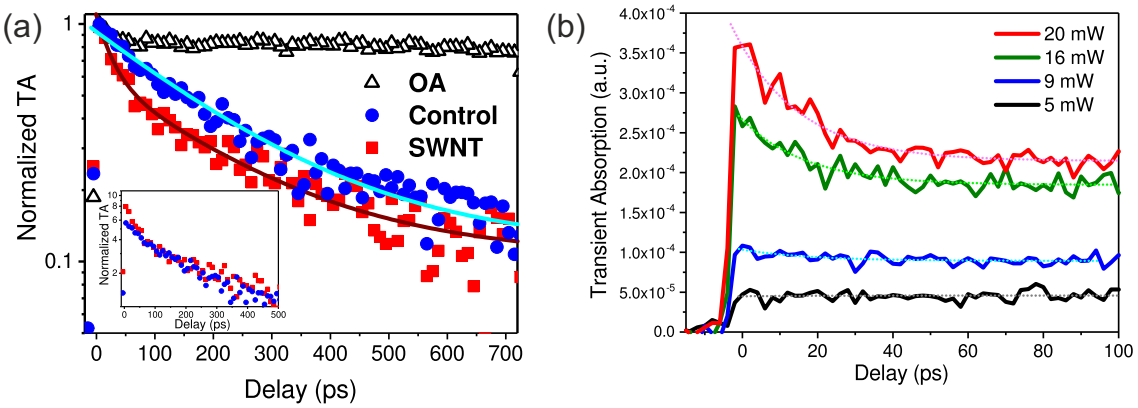


Figure 5.8: (a) Transient absorption for thin films (270 nm) of PbS CQD capped with oleic acid ligands (OA: open circles, thickness 200 nm), PbS CQD with iodide ligands (Control blue circles), and PbS CQD with iodide ligands with SWNT/P3HT (SWNT red squares). The pump laser for excitation was chosen at 1.55 eV (800 nm) at an estimated photon flux of about 4×10^{14} photon cm^{-2}. The probe was selected to be at the first absorption peak for those samples, 1.30 eV (950 nm). (b)Pump fluence dependence transient absorption for the OA capped sample. The fitting indicates a fast decay of 17±1 ps.

Electronic impedance spectroscopy was carried out for control and the SWNT devices which have shown a much lower charge transfer resistance. These measurements were performed to explore the charge dynamics and measure charge transfer resistance values in the photovoltaic devices under illumination. Lower charge transfer resistances observed in impedance spectra could identify if the charge transfer in the device is more efficient.[184–186] An Agilent E4980A precision LCR Meter was used to obtain impedance

spectra of photovoltaic devices over the 100 Hz-2 MHz frequency range with various bias voltages from -1V to +2V. Samples were under 617 nm wavelength illumination generated by a Thorlabs M167F2 fiber-coupled LED with intensity was set so that the photovoltaic devices have voltages equal to V_{oc}. The wavelength of the light was set to 617 nm because light of wavelengths shorter than 600 nm will give more absorption in the SWNT-P3HT composite which is not suitable to observe charge transfer from PbS to SWNT-P3HT. Figure 5.9a and figure 5.9b are impedance spectra under illumination for control and SWNT samples with the bias voltage equal to V_{oc}. A single RC-model was used to fit the Nyquist plots obtained by impedance spectroscopy for either n-i (control) or n-i-p (SWNT) planar heterojunction solar cells. The equivalent circuit based on the RC-model is shown in the figure 5.9c, where R_{ser} is the series resistance, C_{tot} is the total capacitance in the solar cell, and R_{char} is the charge transfer resistance in the solar cell. Values of these parameters obtained by fitting are listed in Table 5.1. With SWNT-P3HT, the charge transfer resistance had a drastic decrease from 115280 Ω to 13238 Ω. These results further suggest that employing the SWNT-PMMA composite could improve charge transport throughout the device.

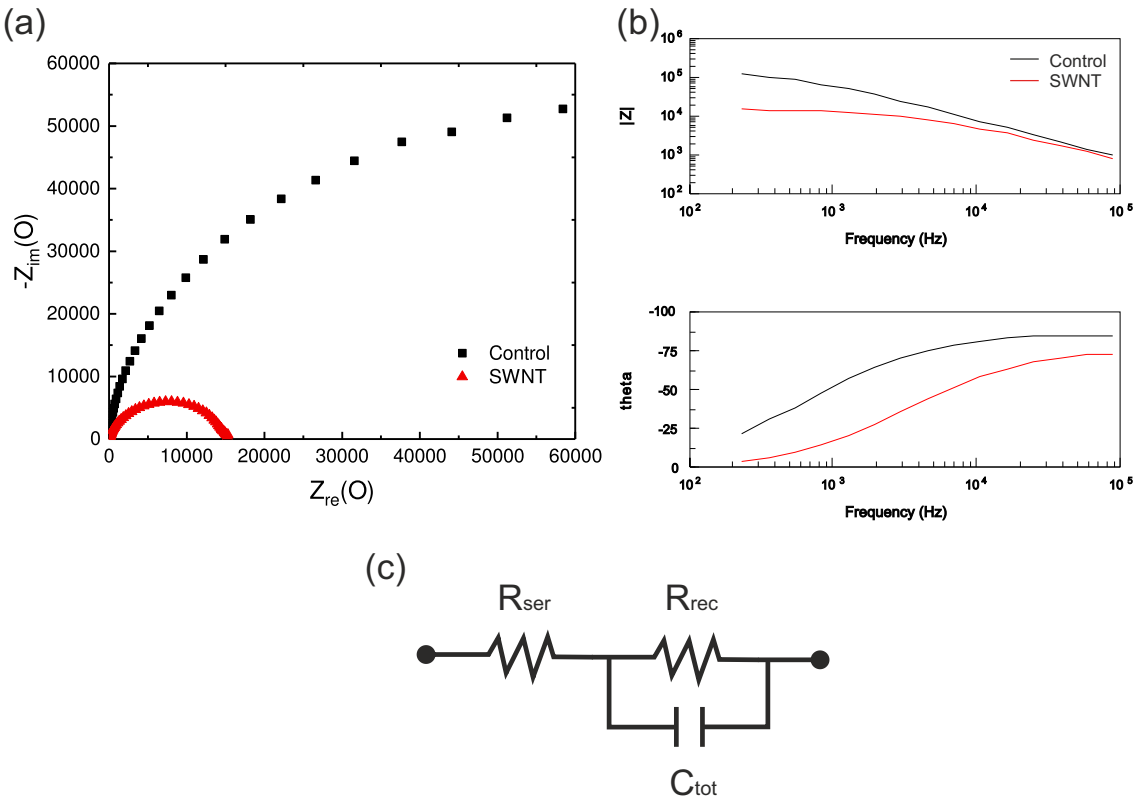


Figure 5.9: (a) Nyquist plot of impedance spectra of control and SWNT devices under 617 nm wavelength illumination at a bias voltage equivalent to the solar cell open circuit voltage. (b) |Z| *versus* frequency plot and theta *versus* frequency plot corresponding to acquired Nyquist plots. (c) Equivalent RC circuit used to fit the impedance spectra, where R_{ser} is the series resistance, C_{tot} is the total capacitance in the solar cell, and R_{char} is the charge transfer resistance in the solar cell.

Table 5.1: List of parameters obtained by fitting impedance spectra using the equivalent circuit shown in figure 5.9. The active area of the device is 0.01 cm^{-2}.

Sample	R_{ser} (Ω)	R_{char} (Ω)	C_{tot} (F)
control	126	115280	2.023×10^{-9}
SWNT	270	13238	2.662×10^{-9}

5.2.3 Optical enhancement

Considering the magnitude of the increase in current density in the presence of SWNTs, I investigated the impact of the SWNT composite layer on the external quantum efficiency (EQE). The results from both reflectance and EQE measurements indicate that the inclusion of the composite layer of SWNTs and PMMA enhances the optical ab-

sorption and EQE in photovoltaic devices. figure 5.10a shows the absorbance spectra for different architectures of the photovoltaic device with the Au electrode on top made with an integrating sphere. In this measurement, a reduction in reflection means that a sample absorbs more of the probe light as all the scattered light is detected.

For the SWNT device without PMMA (0 nm in figure 5.10a), I observe a significant decrease in reflection over a broad region centered around 800 nm with an additional absorption at around 590 nm when compared with the control sample. I attribute this additional peak to the characteristic reflection feature of the P3HT sheath wrapped around the SWNTs. In addition to the optical absorption of the SWNTs, the change of the light absorption (reflectance) is also influenced by varying the thickness of PMMA matrix layer (see figure 5.10 to figure 5.11). As I systematically increase the thickness of the PMMA layer on top of the SWNT layer, I observe a maximum in absorption at a thickness of 70 nm (figure 5.10a). This corresponds to a rising excitation feature (at around 800 nm) in the EQE spectra, reaching its highest point at 70 nm (figure 5.10b). Further increasing the PMMA thickness leads to a re-increase of the reflectivity and a decrease in EQE. This thickness dependence directly translates into J_{sc} values which reach their maximum value when the reflectance is at its lowest and the EQE is at its highest in figure 5.11. Interestingly, for PMMA thicknesses beyond 200 nm, I observe a reversal of the trend, with a re-increase in photoconversion in the red region of the spectrum. This observation leads us to conclude that the SWNT-PMMA layer acts as an optical spacer which enhances the absorption properties of the device stack, and contributes to the overall improvement in performance. Optical spacer effects are the result of constructive interference in the absorber layer leading to enhanced light absorption.[187,188] The optical spacers layer in between subcells of tandem solar cells modifying the interference minimum and maximum in subcells was reported to rectify the current mismatch between subcells.[189] If the extra interface reflects more of the light that has already penetrated the photoactive layer, that helps that photoactive

layer to absorb more photons. The variation of the optical absorbance depending on the thickness of PMMA can be ascribed to the change of the spatial distribution of the light intensity with respect to the absorber layer resulting from the interference between the incident light and reflected light from the electrode. By varying the thickness of PMMA, the intensity of the interference occurs at different depths in the PbS photoactive layer. At a PMMA thickness of 70 nm, the intensity peak appears to be optimally located inside the absorber allowing for maximal photoconversion.

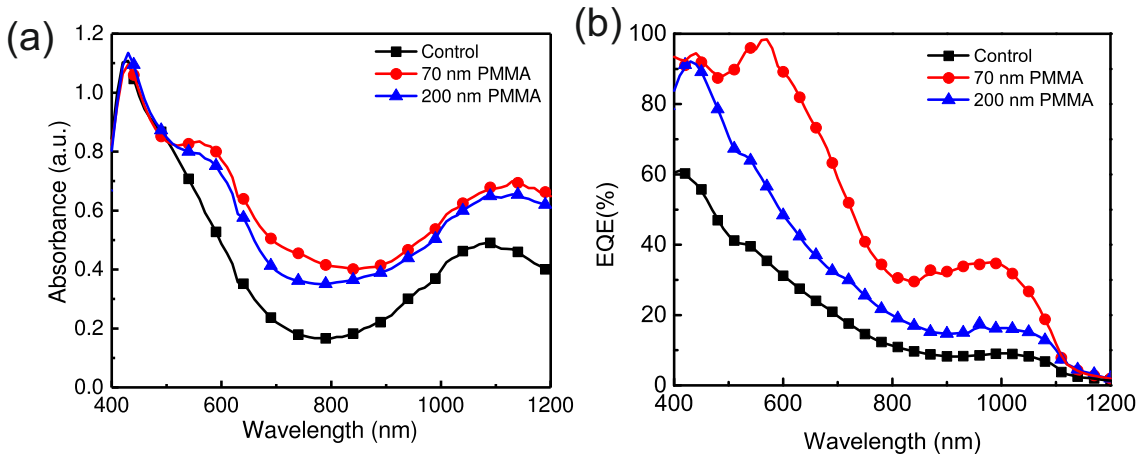


Figure 5.10: (a) Absorbance of control sample (black squares) without both SWNT/P3HT and PMMA, 70 nm (SWNT with 70 nm PMMA matrix) device (red circles), and 200 nm (SWNT with 200 nm PMMA matrix) device (blue triangles). (b) External quantum efficiencies (EQE) for control (black squares), 70 nm (SWNT with 70 nm PMMA matrix) device (red circles), and 200 nm (SWNT with 200 nm PMMA matrix) device (blue triangles) as a function of wavelength from 400 nm to 1200 nm.

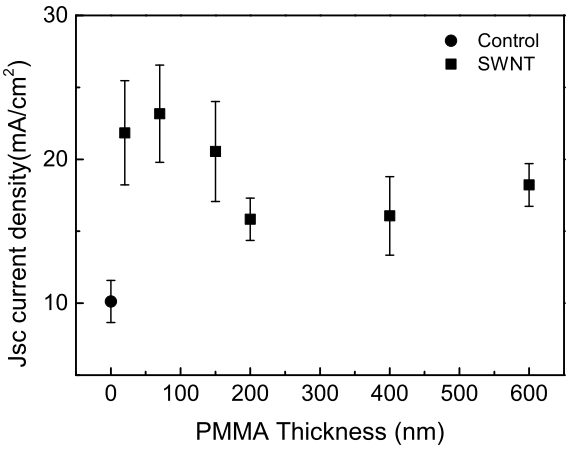


Figure 5.11: Comparison of J_{sc} for control device and SWNT devices. The thickness of PMMA were varied over the range 0 nm, 20 nm, 70 nm, 150 nm, 200 nm, 400 nm, 600 nm for these SWNT devices.

The overall comparisons of the obtained data from reflectance and EQE measurements are summarized in figure 5.11. As shown in this figure, the absorption traces are reflected in the EQE results except for the SWNT device with 70 nm of PMMA (70 nm SWNT device) and the one with 400 nm of PMMA (400 nm SWNT device). For the 70 nm SWNT device, the EQE signal was exceptionally high in the NIR region (800-1100 nm) compared to devices with different PMMA thickness. This can be ascribed to the depth where NIR absorption occurs in a PbS CQD thin film. If the peak of the interfered light happens to be at the optimal region regarding the diffusion length of electrons and holes in the photovoltaic device, the quantum efficiency would rise. Next, although the reflectance data shows that the 400 nm SWNT device had a similar spectrum to the SWNT device with 600 nm PMMA (600 nm SWNT device) matrix, the EQE of the former was lower than the one of the latter in the short-wavelength region. The cause of this mismatch between reflectance data and EQE data might be carrier recombination happening in the functional layer. The series resistance of the 400 nm SWNT device was significantly lower (18 Ωcm^2) compared to the other device architectures (see figure 5.13). This series resistance value of the 400 nm SWNT device suggests that carrier recombination is increased because

of the resistance in SWNT/P3HT-PMMA layer with an exceptionally thick PMMA matrix. The difference of series resistance and EQE between the 400 nm SWNT and 600 nm SWNT devices could be due to the morphological change of SWNT/P3HT in the solution processing.

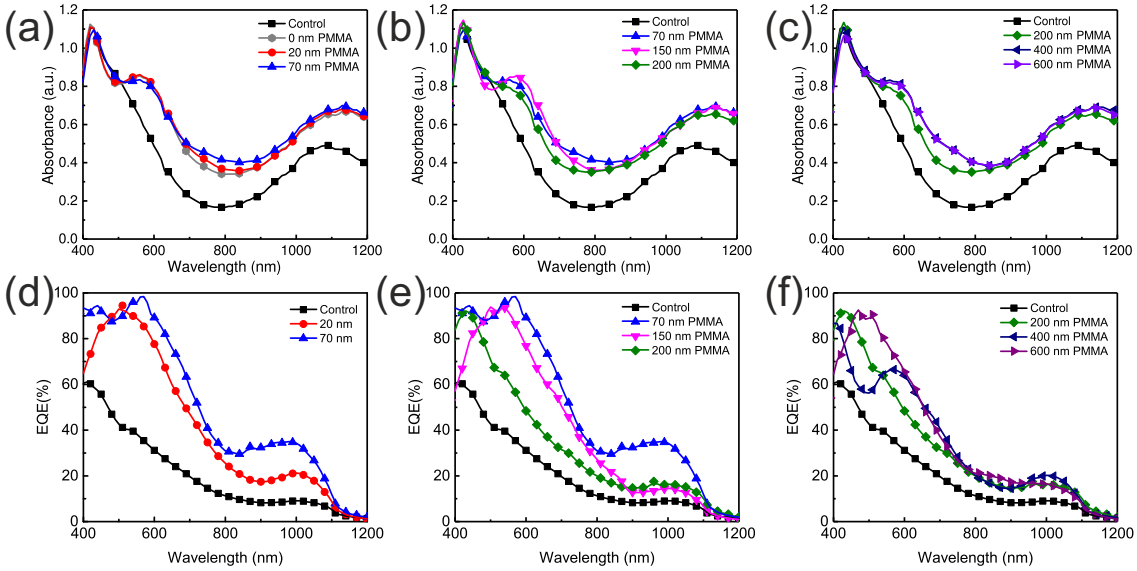


Figure 5.12: Absorbance of (a) a set of full control stack without both SWNT/P3HT and PMMA, 0 nm (SWNT without PMMA matrix), 20 nm (SWNT with 20 nm PMMA matrix), and 70 nm (SWNT with 70 nm PMMA matrix) device, (b) a set of control, 70 nm device, 150 nm device, and 200 nm device, and (c) a set of control, 200 nm device, 400 nm device, and 600 nm device. EQE of (d) a set of control without both SWNT/P3HT and PMMA, 0 nm (SWNT without PMMA matrix) device, 20 nm (SWNT with 20 nm PMMA matrix) device, and 70 nm (SWNT with 70 nm PMMA matrix), (e) a set of EQE of control, 70 nm device, 150 nm device, and 200 nm device, and (f) a set of EQE of control, 200 nm device, 400 nm device, and 600 nm device.

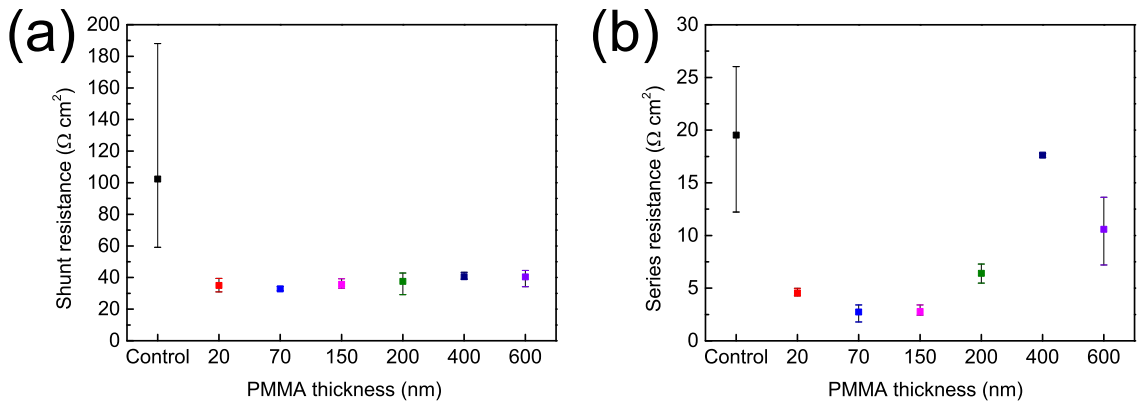


Figure 5.13: (a) Shunt resistance, and (b) series resistance of control devices and SWNT devices with different PMMA thickness from 20 nm to 600 nm. For the shunt resistance, the control samples exhibited higher (better) values compared to the SWNT devices regardless of their PMMA thickness.

5.2.4 Simulation of optics

From the absorption measurements by integrating sphere and the EQE measurements, the hypothesis that the light distribution changes with the application of SWNT/P3HT-PMMA was proposed. To support this hypothesis, my collaborator Dr. Severin Habisreutinger modeled the effect of the PMMA layer thickness on the current generation employing a transfer-matrix formalism developed by Burkhard *et al.*[190] The optical constants for the PbS layer required for the model were first measured by ellipsometry. In this modeling approach he investigated how the photocurrent generation in the device stack is affected by variations of the PMMA layer thickness. To simplify the approach he assumed an internal quantum efficiency of 100%.

Modelling the absorption through the device stack shows that the stack with 50 nm PMMA has an increased absorption peak between 900 and 1000 nm, which is in good agreement with the increased EQE in the same range (figure 5.10 b). As the underlying mechanism for the observed improvements in the red-IR absorption of the device stack in the presence of the PMMA layer, he postulated an optical spacer effect. This effect is based on an optimized distribution of the incident electric field through the absorber layer. This result is summarized in figure 5.14, where the optical properties

of the device stack across the wavelength range from 400 to 1200 nm are presented comparing two different device stacks, one without a PMMA spacer and one with a spacer of 50 nm. In the presence of the optical spacer, the relative absorption in the PbS layer increases, in particular 800 - 1000 nm range. This simulated result corresponds well to the experimental observation shown in figure 5.10. In fact, by modeling the electric field intensity of the light through the device stack for different wavelengths (figure 5.15), he could show that the addition of 50 nm of PMMA has a strong effect especially on the 1000 nm wavelengths. In contrast to the stack without PMMA, a much higher fraction of the field distribution conincides with the CQD absorber layer of the stack at this wavelength, resulting in an increase in charge generation (figure 5.17). Similarly, he observed that a larger fraction of the electric field at 600 nm conincides with the absorber layer, which is consistent with the enhanced EQE measured at this wavelength (figure 5.10b). The beneficial effect of the optical spacer on the distribution of the optical electric field is apparent in particular for the wavelength of 1000 nm, which corresponds well with the observed increase in EQE in this wavelength range (figure 5.10 and figure 5.12).

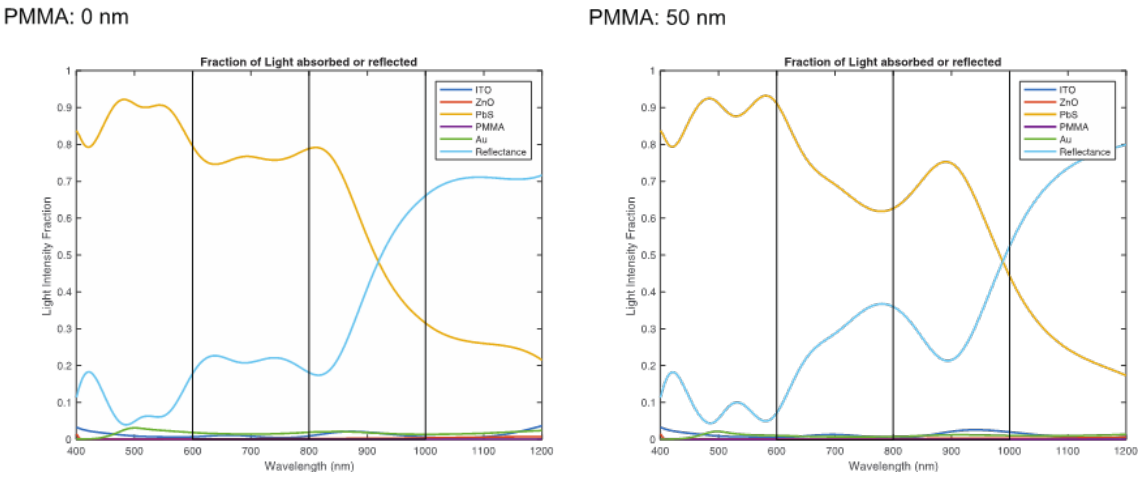


Figure 5.14: These two graphs show the modelled absorption of the incident wavelengths in the different layers as a fraction of the total incident light (per wavelength), as well as the wavelength-dependent total reflection of the stack.

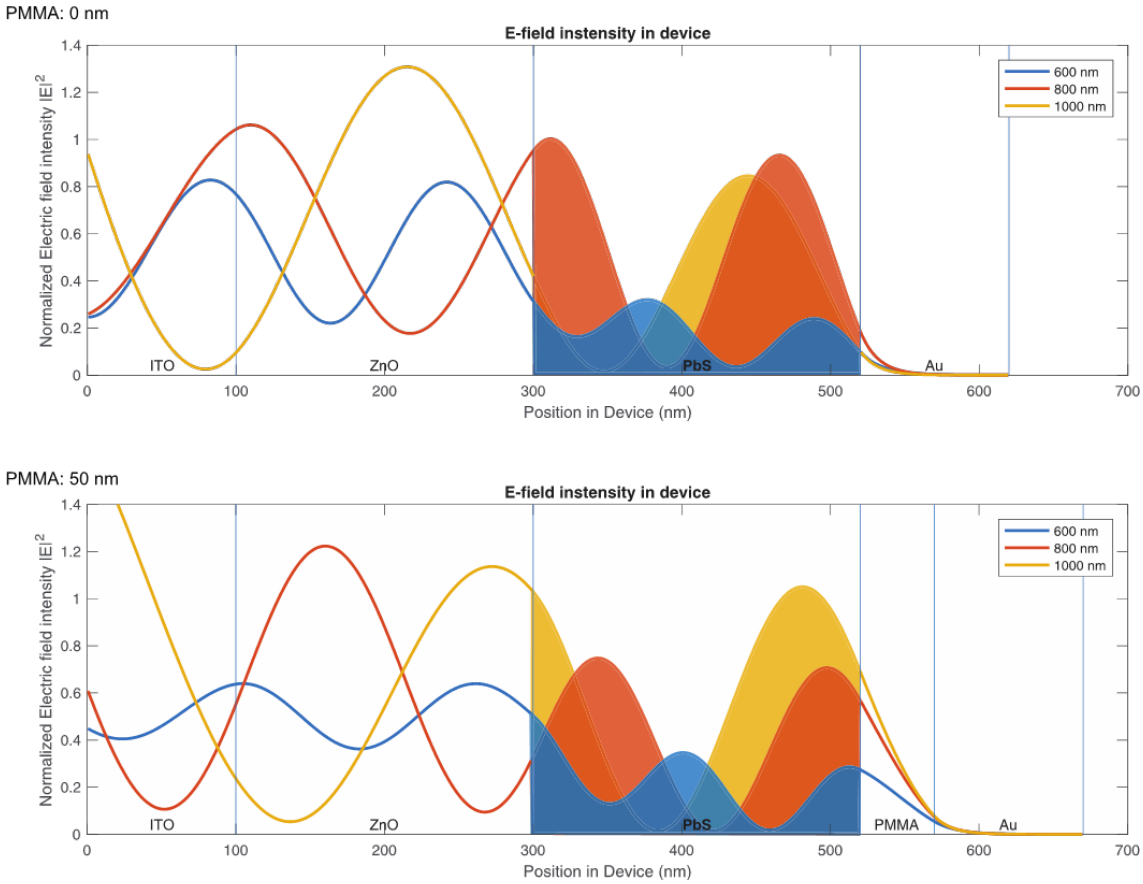


Figure 5.15: The simulation of red-IR absorption of the device stack in the presence of the PMMA layer. Two different simulated models are compared. One is in the absence of the optical spacer (top), and another is in the presence of an optical spacer of 50 nm (bottom).

With increasing PMMA thickness, the model in figure 5.17 shows an initial increase in photocurrent at around 50 nm, followed by a decrease in photocurrent. To simplify the approach he assumed an internal quantum efficiency of 100%. The resulting current dependence on the PMMA layer thickness (figure 5.17) follows the experimental trend (figure 5.11), as there is a clear maximum at around 50 nm, and a minimum at around 200 nm. Overall the trend appears to follow qualitatively the experimentally observed trend. Quantitatively, the experimental trends exceed these predictions to some extent which can be explained by taking into consideration the previous observations of enhanced hole transfer due to the presence of the SWNTs, which significantly enhances the effect of the optical spacer. This is well illustrated by the comparison of

the device stack without SWNTs or PMMA, and the device stack with SWNTs and 70 nm PMMA, which results in a significant increase in photocurrent extraction. The model predicts that the addition of a PMMA layer of this thickness should more than double the charge generation near the p-type interface (figure 5.17). The increase in J_{sc} is therefore probably the result of compounding positive effects of improved charge transport, increased photoconversion and vicinity of charge generation in the PbS CQD photoactive layer.

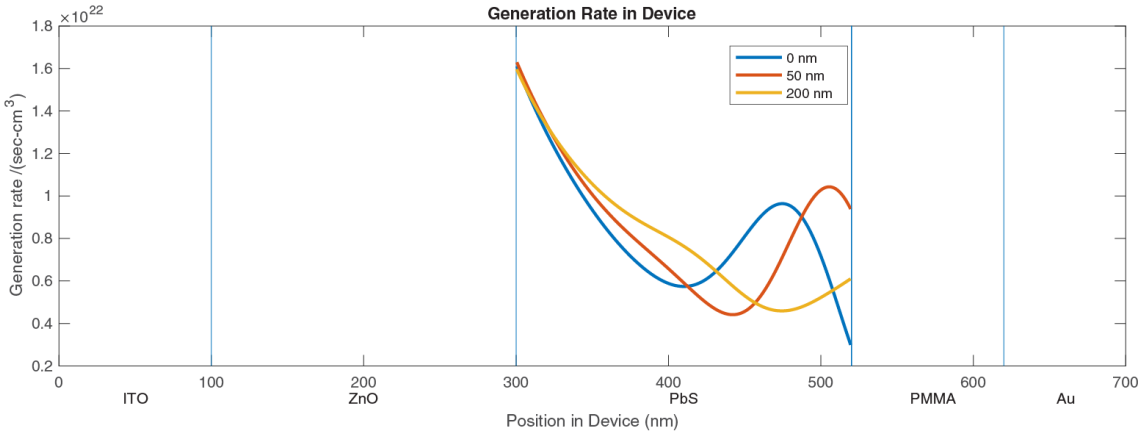


Figure 5.16: Excitation generation for device stacks with PMMA layers of different thicknesses. This simulation demonstrates the position in the absorber layer where charges are generated for an incident AM1.5 spectrum.

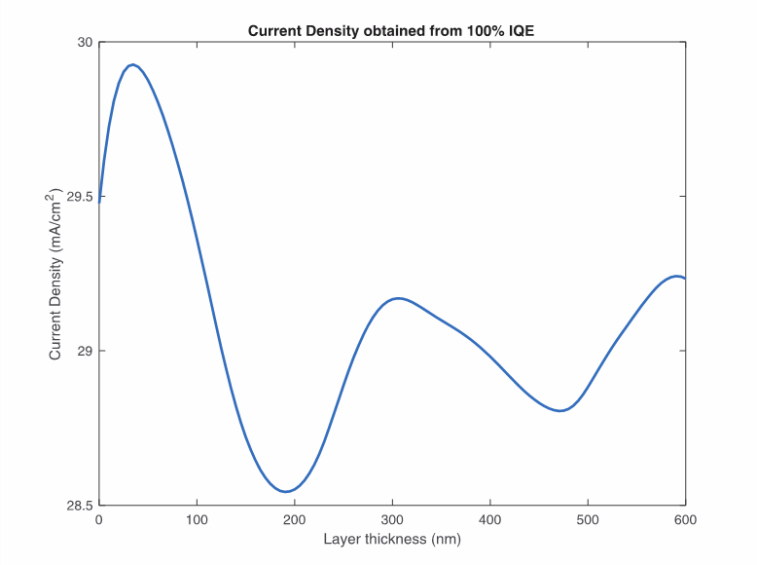


Figure 5.17: PMMA thickness dependence of the J_{sc} current density on the assumption of 100% IQE. The model stack includes, analogously to the experimental devices, the following layers at a fixed thickness; glass as substrate, a layer of ITO (100 nm), ZnO (200 nm) as n-type layer, the PbS absorber (220 nm) and gold (100 nm).

5.2.5 Stability

In addition to improving the overall device performance, I also find that the SWNT-PMMA layer enhances the device stability. This observation is confirmed by tracking the device performance over a 35-day period, where the devices were stored in ambient air without humidity control under dark conditions (see figure 5.18). Although some deterioration of the performance can be observed for the SWNT devices, they appear to retain the majority of their initial efficiency, while the control devices perform almost 50% worse than initially after 35 days. Store devices under dark conditions is comparable with ISOS-D-1 according to the stability testing protocols for organic PV devices.[191]

Our hypothesis is that the protective effect of the PMMA layer is to block the ingress of water and oxygen which could degrade the quality of the photoactive PbS CQD layer by affecting the surface defects on the nanocrystals and ligands coordinated to the nanocrystals. The oxidized surface defects on nanocrystals create mid-gap states

which facilitate charge carrier recombination,[63] or change the electronic structure and the position of the energy levels of a CQD thin film.[192] This energy level alteration can explain the trends of V_{oc} in the control devices. Some extent of oxidation in the photovoltaics was found to improve the band alignment of the photovoltaics,[151] and could be due to the improvement of V_{oc} after 10 days of the storage. However, further oxidation of PbS made deteriotated V_{oc}. The alteration of the electronic energy levels of the PbS CQD layer can generate a potential barrier at the interface with the cathode or the n-type semiconductor causing a loss in potential or a decrease in charge extraction.

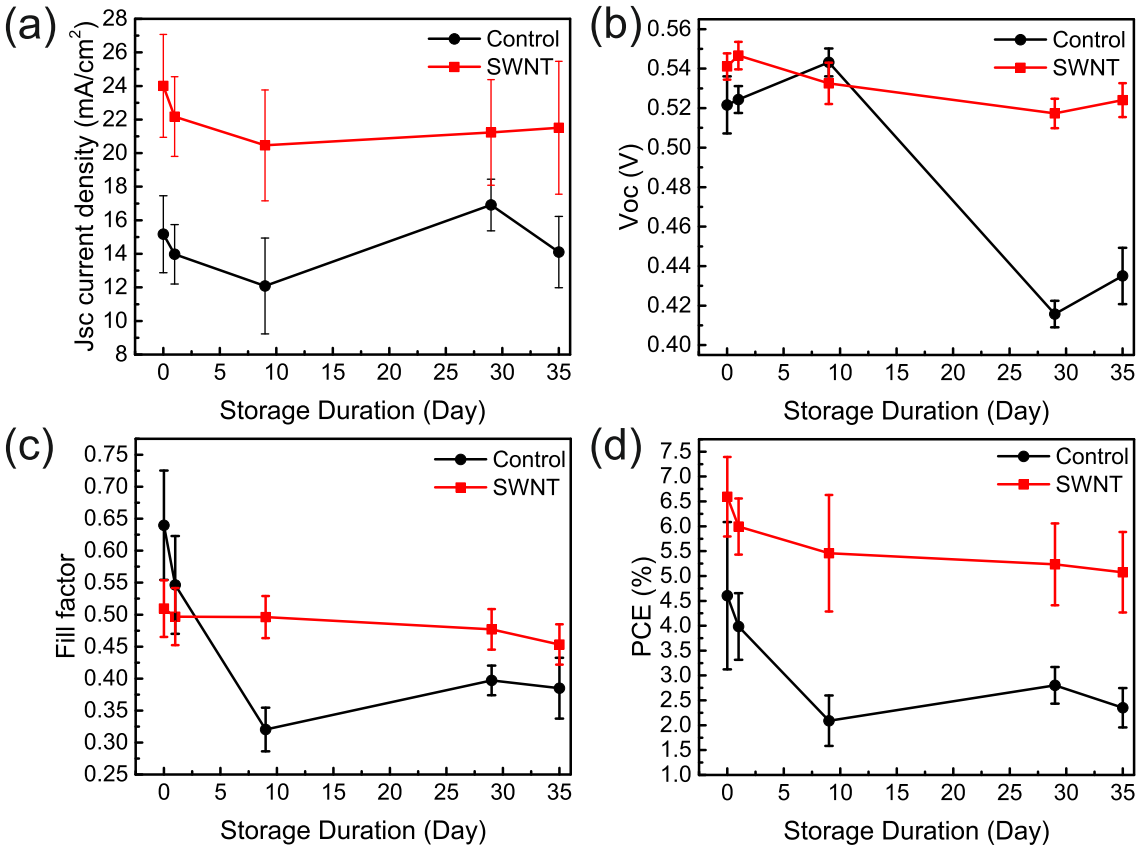


Figure 5.18: The variation of photovoltaic performance metrics of devices with and without SWNT/P3HT-PMMA with storage time. (a) J_{sc}, (b) V_{oc}, (c) FF, and (d) PCE. The devices were unencapsulated and were stored in ambient air between each measurement in a dark environment without any humidity control. The standard deviation (error bars) and the average (data point) were calculated from a sample of 12 devices on 4 separate substrates.

5.3 Conclusions

By employing SWNTs in a PMMA matrix as a hole extraction layer between the photoactive PbS CQD thin film and the Au back electrode, I demonstrate an improvement of up to 50% for the photocurrent of CQD devices, which results in a significant enhancement of the overall power-conversion efficiency (see table 5.2).

My collaborators and I provide experimental and theoretical evidence that the increase in photocurrent comes from optical enhancements in the device as well as faster carrier transfer, namely enhanced light management and better hole extraction. The latter results from the PMMA layer acting as an optical spacer leading to a significant boost of the external quantum efficiency of the PbS CQD absorber.

Furthermore, ultrafast transient absorption measurements suggest much faster hole transfer in the presence of the SWNT-PMMA layer. In fact, I propose that the improvement in the charge-transport characteristics by the SWNTs leads to hole-dominant charge extraction which, in turn, results in the formation of a space charge region causing increased non-radiative charge carrier recombination and thus an overall lower fill factor.

Table 5.2: The comparison of control device and SWNT device in relaxation time in transient absorption (ps), J_{sc} (mA cm^{-2}), power factor in an intensity-dependent J_{sc} measurement, fill factor, and power conversion efficiency (%).

device	relaxation time in transient absorption (ps)	J_{sc} (mA cm^{-2})	power factor α in intensity dependent J_{sc}	FF	PCE (%)
control	81 ± 9	14.0 ± 1.77	0.97 ± 0.00(4)	0.54 ± 0.07	3.99 ± 0.67
SWNT	36 ± 6	22.2 ± 2.38	0.93 ± 0.02	0.49 ±0.04	5.99 ± 0.56

Chapter 6

Bulk Heterojunction PbS CQD SWNT Solar Cells

6.1 Introduction

In chapter 5, the SWNT/P3HT composite was embedded in the PMMA matrix, and the whole film was planarly adjacent with PbS photoactive layer. In this chapter, the possibility of SWNT/P3HT composite to be used as a hole transporting material in a bulk heterojunction structure with a PbS photoactive layer is examined. Introduction of a bulk heterojunction structure is expected to enhance the charge collection length of the junction with PbS CQDs to allow carriers migrating to the contact when the thickness of PbS CQD increases. The first approach is the use of mesoporous TiO_2 for n-type semiconductor as has been developed by research on bulk heterojunction organic solar cells to form a three-dimensional interpenetrating network of donor and acceptor.[108] In that method, large TiO_2 particles (150-200 nm) were deposited on top of a thin TiO_2 layer with smaller TiO_2 particles (10-30 nm). With that mesoporous structure, improved absorption, EQE and photocurrent at infrared wavelengths have been observed.[109] For CQD photovoltaics, the following methods have been explored; lithographically defined nanopillar arrays,[110] porous templated wells,[111] or nanowire arrays[20] of the wide-bandgap n-type semiconductor to make a directional transport.

In this chapter, bulk heterojunctions are fabricated by an all-solution process by spin-coating of a PbS CQD solution and a SWNT-P3HT solution. Due to SWNTs'

exceptional capability in charge transport, they would be the desired materials incorporated in bulk heterojunction structure to suppress carrier recombination while thickening PbS CQD layer to obtain higher absorption.

6.2 Results and Discussion

6.2.1 Device architecture and performance

I hypothesized that the PbS CQD photoactive layer could be thickened by implementing a bulk heterojunction structure with a SWNT/P3HT composite. In this project, two different layers of PbS CQD thin films were deposited for all devices. One is intrinsic PbS CQD thin films with lead iodide and ammonium acetate (PbS-PbI_2/AA) as the primary absorber, and p-type PbS CQD thin films with 1,2-ethanedithiol ligands (PbS-EDT). The PbS-EDT layer is reported to have excellent stability compared with PbS CQD thin films with halide ligands, thanks to its strong binding energy to the Pb atoms on the PbS nanocrystal surfaces. Also, PbS-EDT is expected to mitigate the band mismatching from intrinsic PbI_2/AA to a cathode. In this project, the PbS-EDT layer has been another component of the bulk heterojunctions together with SWNT/P3HT composites because the PbS-EDT layer is deposited by a layer-by-layer deposition method which makes varying the thickness of the bulk heterojunction layer easy. Figure 6.1a and 6.1b show schematic illustrations of the device architecture of the devices with bulk heterojunction structures (BHJ devices), and devices with planar heterojunction structures (PHJ devices). The thickness of the PbS-EDT layer was varied from 60 nm, 120 nm, 180 nm, to 240 nm for both BHJ devices and PHJ devices to explore the effect of bulk heterojunction structures with thicker PbS CQD layers. Figure 6.1c and 6.1d summarize the energy levels of each functional layer in planar and bulk heterojunction solar cells, and how band bending occurs in the actual devices under thermal equilibrium. Both electrodes have ohmic contact as n-type semiconductor ZnO has a higher Fermi level than the Fermi level of ITO, and p-type semiconduc-

tor SWNT/P3HT has a lower Fermi level than the Fermi level of Au. The type of all heterojunctions in these photovoltaics is the type-II heterojunction because each semiconductor overlaps each other and shifts slightly to lower energy level towards Au cathode.

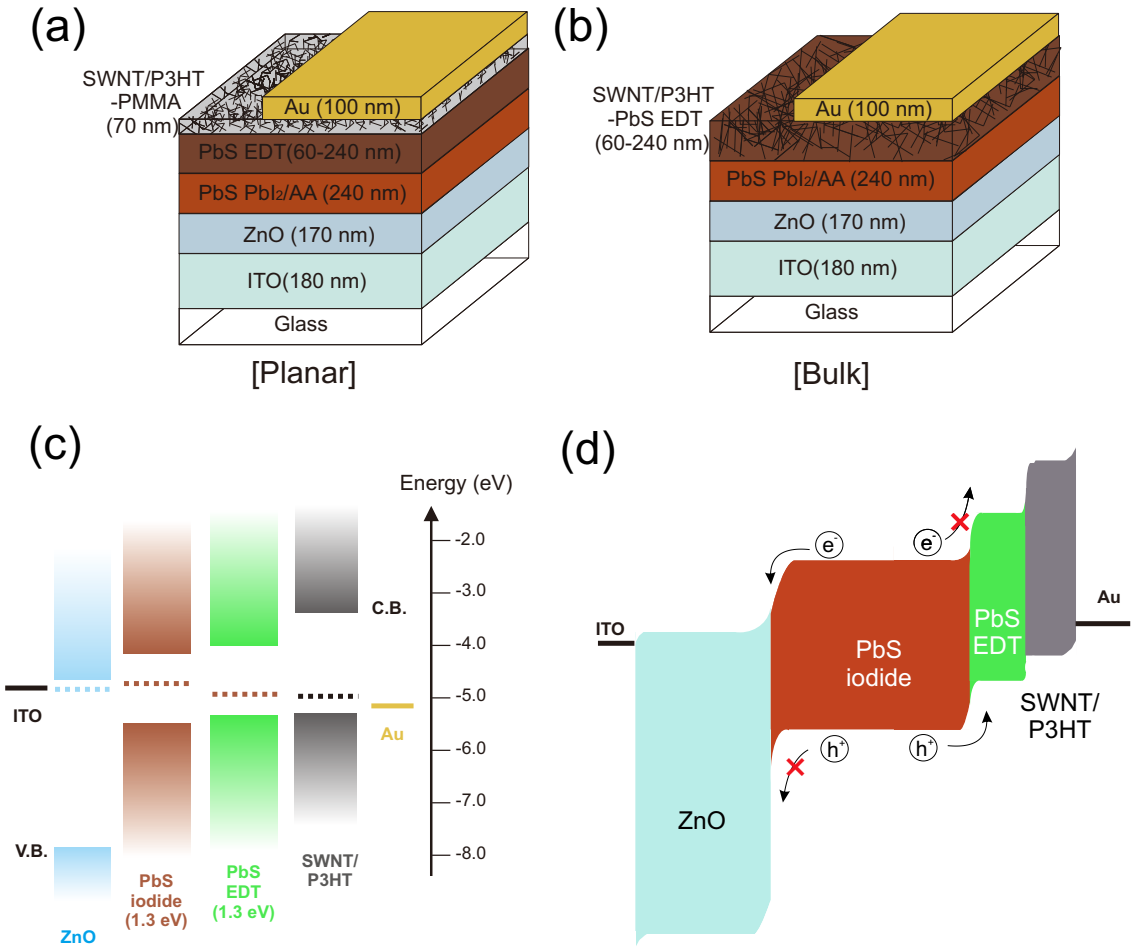


Figure 6.1: Schematic illustrations of (a) PbS CQD solar cell with a planar heterojunction structure, and (b) PbS CQD solar cell with a bulk heterojunction structure. (c) Energy band diagram showing the energy levels of all functional layers in planar and bulk heterojunction devices. (d) Schematic illustration of band bendings in the planar and bulk heterojunction devices.

Figure 6.2a is a cross-sectional image of the BHJ device with 240 nm PbS-EDT layer taken in a FIB-SEM. Figure 6.2b illustrates how carbon nanotubes embed in the PbS-EDT layer and connect to the Au electrode. This structure between carbon nanotubes and EDT-coordinating PbS CQDs realizes the bulk heterojunction structure

in photovoltaic devices. How carriers transport from PbS CQD to carbon nanotubes is expected to be generally analogous to how charge carriers transport from PbS CQD to carbon nanotubes in chapter 5. However, devices in this chapter have PbS-EDT layer which is p-type, and conduction bands of PbS-EDT layer and carbon nanotubes are relatively close compared with extensive separation of conduction band between PbS-MAI and carbon nanotubes in chapter 5. This relatively close gap between conduction bands of PbS-EDT and SWNT/P3HT may suggest that charge transport might be facilitated by the variable range hopping between similar energy levels in between two different materials.[193]

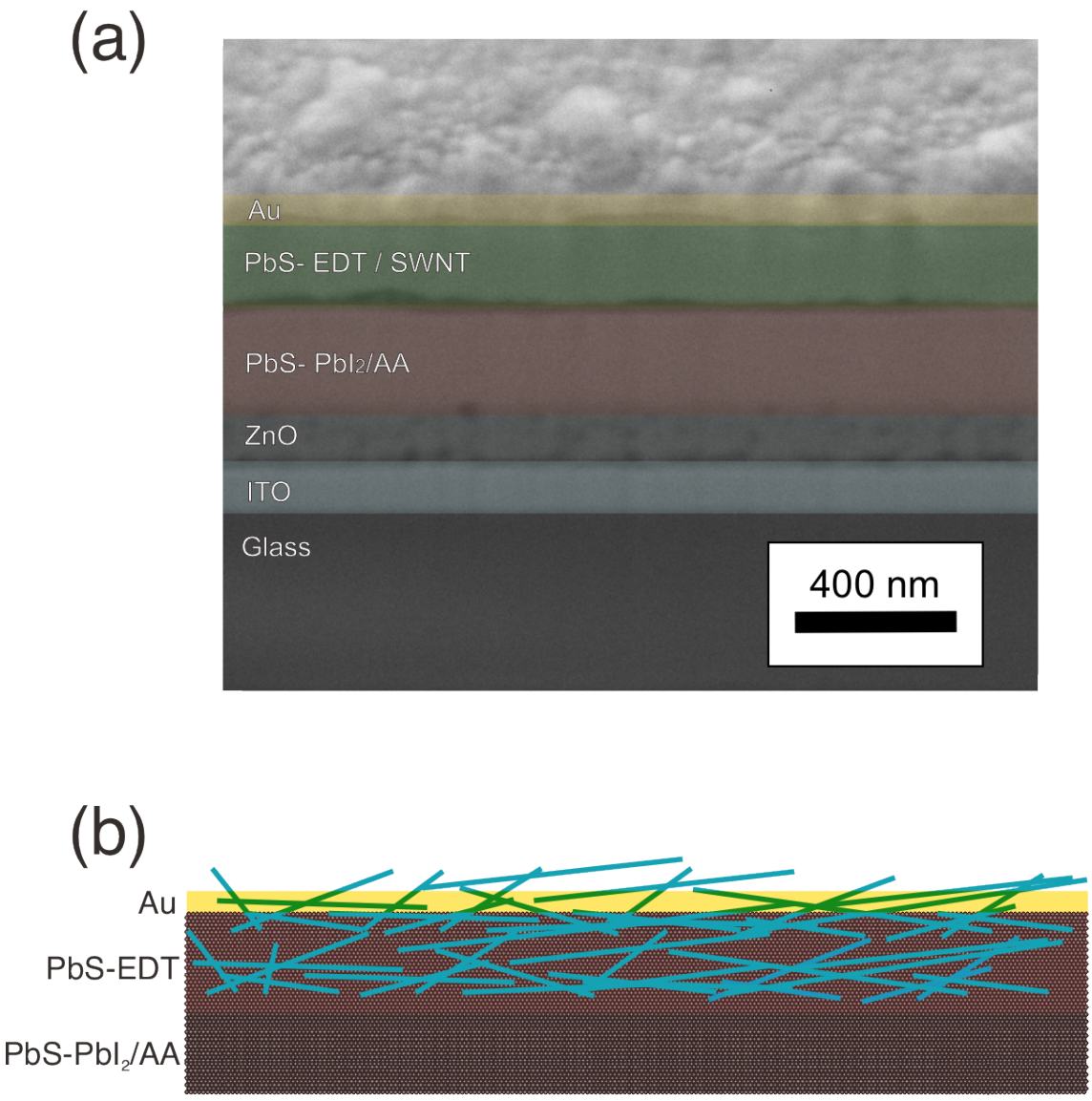


Figure 6.2: (a) FIB-SEM cross-sectional image of bulk heterojunction structure PbS CQD solar cell with 240 nm PbS-EDT and with SWNT-P3HT layer. (b) Schematic illustration of the cross-section of carbon nanotubes embedded in the PbS-EDT layer on the PbS-PbI_2/AA and conduct holes to Au electrode.

Figure 6.3 compares the JV curves of BHJ and PHJ devices at different PbS-EDT layer thicknesses under AM1.5 illumination. From figure 6.3a to 6.3d, the PbS-EDT layer has been thickened, and the thicker the PbS-EDT layer, the champion JV curve of the PHJ devices becomes to a linear curve compared with JV curve of BHJ devices.

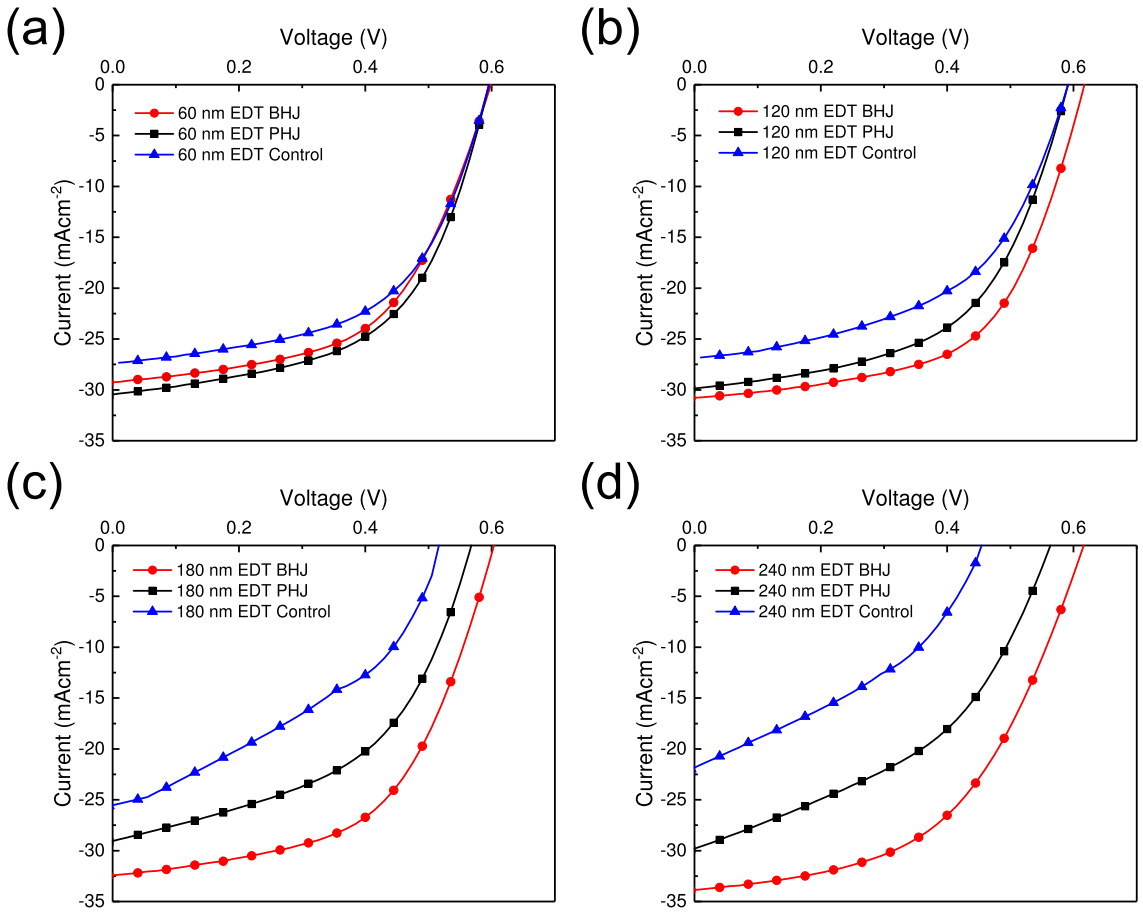


Figure 6.3: J-V curves for median bulk heterojunction structure (BHJ: red line with circle symbols), planar heterojunction structure (PHJ: black line with square symbols), and control (Control: blue line with triangular symbols) PbS CQD devices at (a)60 nm, (b) 120 nm, (c) 180 nm, and (d) 240 nm thickness of PbS-EDT.

First, control devices performed much worse than BHJ and PHJ devices when the PbS EDT layer thicknesses exceeded over 120 nm. The first noticeable change was J_{sc} and fill factor values, and even V_{oc} values got much lower than the other two devices when the thickness of the PbS EDT layer hit to 240 nm. Regarding the comparison of JV curves of BHJ, PHJ and control devices, three critical parameters (J_{sc}, V_{oc}, and FF) and overall power conversion efficiency (PCE) are summarized in figure 6.4. There is a remarkable difference in J_{sc} between BHJ and PHJ devices. Although the PHJ devices have shown the similar J_{sc} value to BHJ devices with PbS-EDT thicknesses up to 120 nm, the PHJ devices with PbS-EDT layer over that thickness showed a decrease

or plateau in J_{sc}. Contrary to that, the BHJ devices exhibited an increase of J_{sc} when the PbS-EDT layer was thickened from 120 nm to 240 nm. Next, while V_{oc} of the PHJ devices had a monotonic decrease as the thickness of the PbS EDT layer was increased, the BHJ devices could maintain the value of V_{oc} over 0.6 V as the thickness of PbS EDT layer increased to 240 nm. This observation is due to the probability of carriers recombining at the trap states of the thickened PbS EDT layer. If the thickness of the PbS EDT layer increases, it may provide a higher probability for carriers to recombine in the devices. The lost of the potential of excited electrons by carrier recombination will reduce V_{oc} of the devices. Although there are differences in V_{oc} values of BHJ and PHJ devices as the thickness of the PbS EDT layer is increased, those differences are relatively small compared with the differences in fill factor (FF) of those devices. The fill factor is more directly affected by carrier recombination in photovoltaic devices. As presented in figure 6.3, the JV curves of PHJ devices show more linear curves than the JV curves of the BHJ devices when the PbS EDT thickness was more than 180 nm, which means that the PHJ devices have a lower fill factor. With the improvement of carrier collection in the PbS EDT layer, BHJ devices exhibited 18% higher FF values than PHJ devices with a PbS EDT layer thickness of 240 nm. As a result of combining those three critical parameters, the power conversion efficiency (PCE) of the BHJ devices was higher for thicker PbS EDT layers (120-240 nm), so the device efficiency of BHJ devices was of a similar value to PHJ devices with a 60 nm PbS EDT layer. The BHJ devices achieved the highest PCE with a 120 nm PbS EDT layer, maintaining the high device performance through 240 nm PbS EDT thickness, which is contrary to the devices which show a monotonic decrease in device performances.

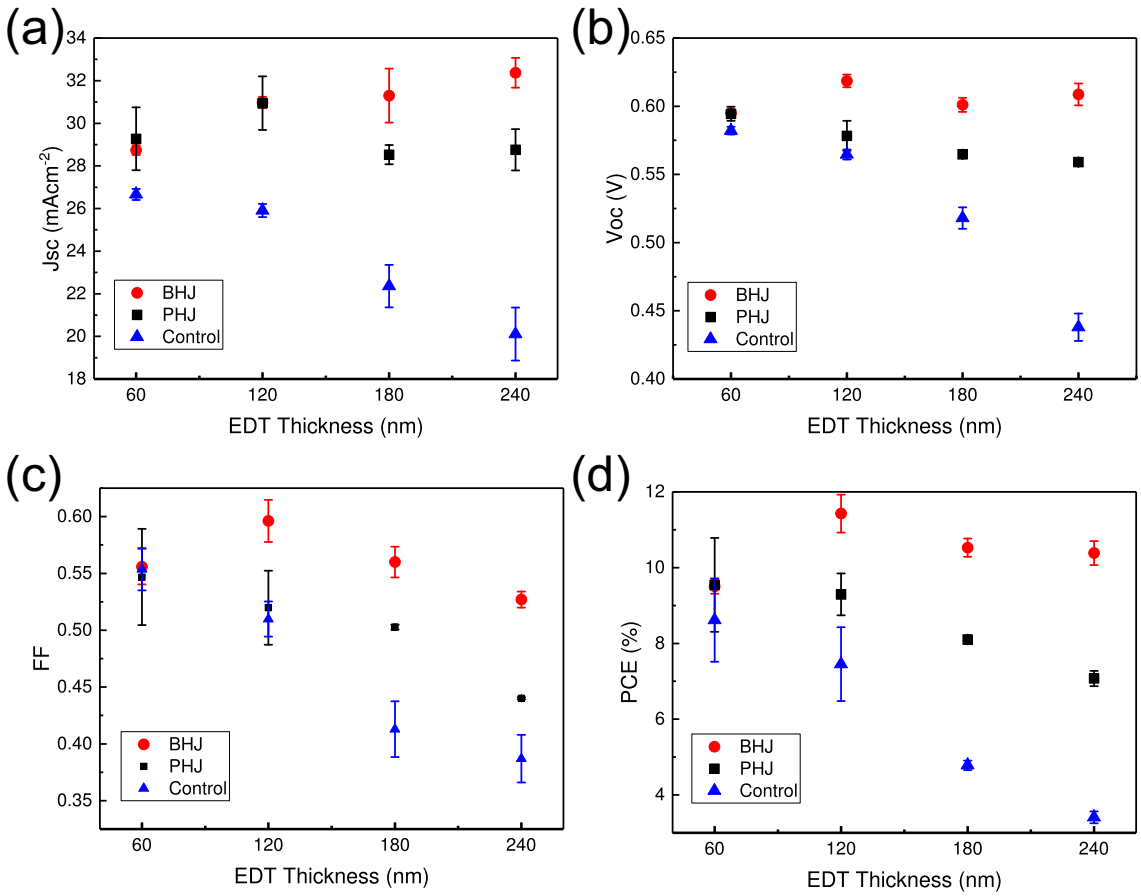


Figure 6.4: (a) J_{sc}, (b) V_{oc}, (c) FF,and (d) PCE of PbS CQD bulk heterojunction solar cells (BHJ) and PbS CQD planar heterojunction solar cells (PHJ) at different thickness of PbS-EDT layer under AM1.5 illumination in nitrogen atmosphere at day 1 of storage. The reported mean values and error bars for all parameters were calculated from a sample of 12 devices.

6.2.2 Comparison of BHJ and PHJ devices

As presented in figure 6.3 and figure 6.4, BHJ devices have shown significant advantages over PHJ and control devices in terms of the fill factor. I hypothesize that this improvement in fill factor is brought about by the reduction of non-radiative recombination in the PbS-EDT layer. To examine the cause of the charge carrier recombination happening in PHJ devices, measurements of V_{oc} under different white light intensities (figure 6.5a-d) were carried out. The dependence of V_{oc} on light intensity is expected to reflect both monomolecular and bimolecular recombination as all of the charges recombine at open-circuit condition.[179] Figure 6.5 presents the plot of V_{oc} *versus* natural logarithm

of the light intensity for both control and SWNT devices. The slope of that plot gives kT/q for both monomolecular and bimolecular recombination.[180] If monomolecular recombination is important in addition to bimolecular recombination, a slope greater than kT/q is observed.[181] In figure 6.5a-d, while the BHJ devices maintain slope from 2.5 kT/q to 3.0 kT/q, PHJ devices have a much steeper slope especially with thicker PbS EDT layers. With a 60 nm PbS EDT layer, PHJ devices have exhibited a slope of 4.77 kT/q, and this became steeper to 10.5 kT/q. This indicates that recombination due to trapping sites for either holes or electron in a thicker PbS EDT layer is significant, and the bulk heterojunction structure of PbS EDT and SWNT reduces the impact of the trap states in thick PbS EDT film.

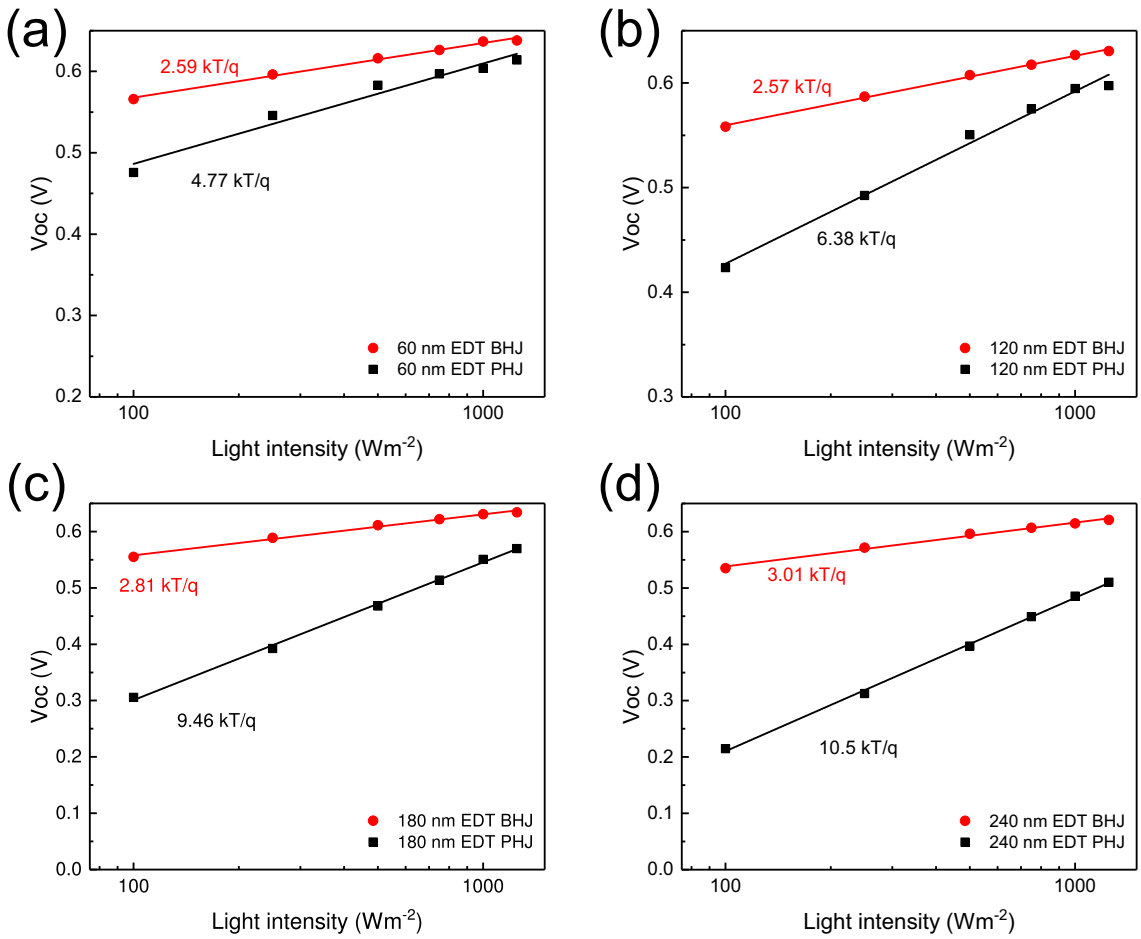


Figure 6.5: Comparison of V_{oc} values in BHJ and PHJ devices *versus* light intensity in logarithmic scale plots with (a) 60 nm, (b) 120 nm, (c) 180 nm, and (d) 240 nm EDT thickness.

In addition to the reduction of monomolecular carrier recombination in BHJ devices which has contributed to the improvement of V_{oc} and FF, the J_{sc} of BHJ was slightly better than in the PHJ devices at the same thickness of PbS EDT layer. To explore the causes behind these J_{sc} features, external quantum efficiency (EQE) and absorbance measurements have been conducted. First, the EQE measurement was done from 350 nm to 1100 nm. This measurement can show how much excitation and collection of carriers have been achieved with a certain level of illumination to the devices without excluding the reflective effect from front glass of PV devices. Figure 6.6a-d compares the EQE of BHJ devices and PHJ devices at different thicknesses of PbS EDT layer. As shown in figure 6.8a, the BHJ and PHJ devices did not show remarkable differences in EQE curves if the PbS EDT layer thickness was only 60 nm. However, once the thickness of the PbS reaches 120 nm, the BHJ devices had a slightly higher efficiency in EQE throughout the measured range of wavelength. The degree of the increase in EQE became even more prominent for devices with 180 nm and 240 nm PbS EDT layers. This increase of EQE for BHJ devices might be due to either the improvement of carrier collection after the excitation or enhancement of the absorption caused by the light scattering effect by the SWNT-P3HT composite. Xu *et al.* claimed that TiO_2 nanowires in PbS thin films enhanced the absorption in the PbS film by the nanowires' light scattering effect.[194]

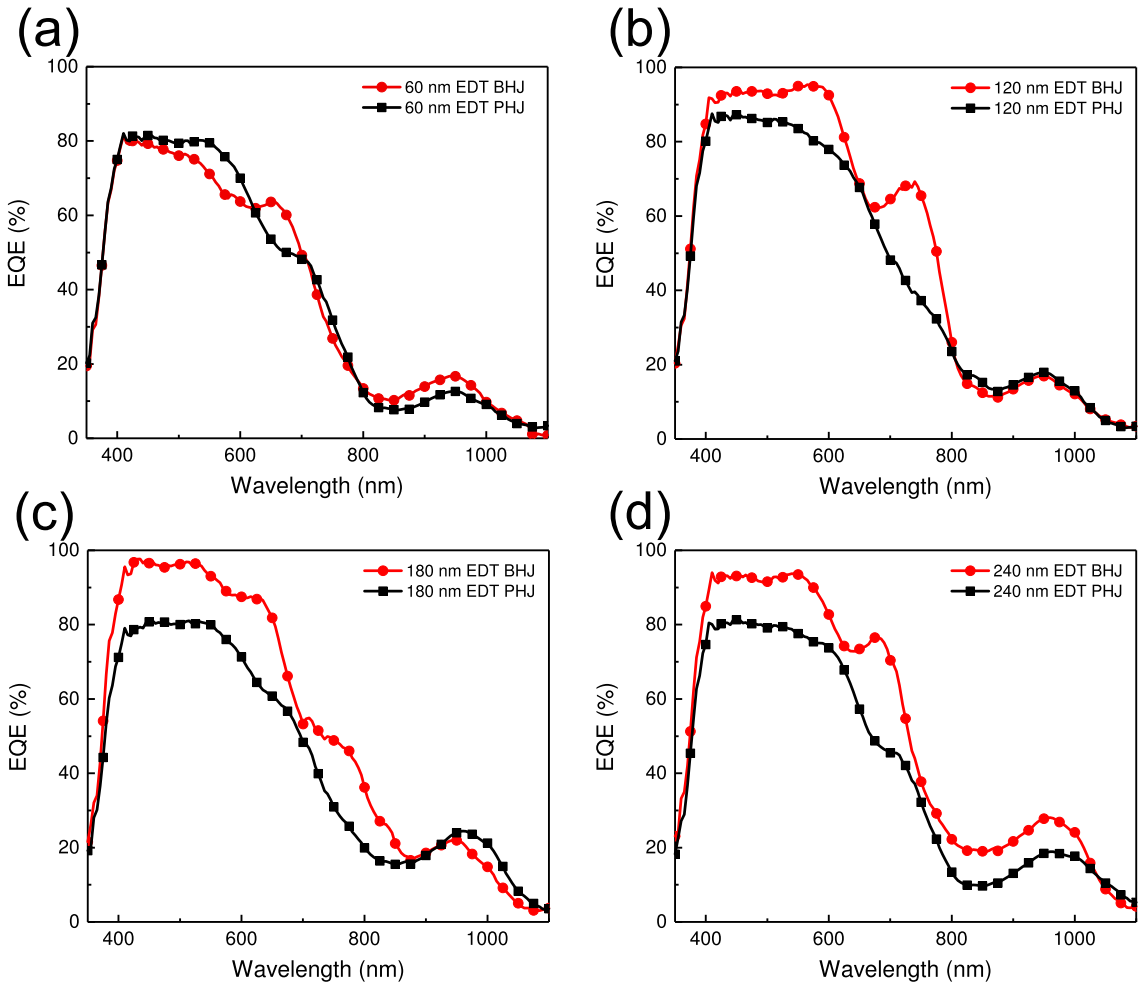


Figure 6.6: Comparison of BHJ (red solid line with circular symbols) and PHJ (black solid line with square symbols) in external quantum efficiency (EQE) over 350 nm to 1100 nm wavelength with (a) 60 nm, (b) 120 nm, (c) 180 nm, and (d) 240 nm EDT thickness.

To examine the hypothesis that BHJ devices have a higher absorption with incorporating SWNT-P3HT composites in the PbS EDT layer, absorbance measurement by integrating sphere has been conducted. Figure 6.7 compares the absorbance of the BHJ and PHJ devices with several different thicknesses of PbS EDT layer. Comparison of the absorption in the PV devices with different PbS EDT thickness gave consistent result. First, both BHJ and PHJ device withs 60 nm PbS EDT have exhibited a strong transmission peak at around 760 nm. When the thickness of the PbS EDT increased from 60 nm to 120 nm, the absorption at 760 nm increased by 0.15 absorbance units

for both BHJ and PHJ devices. Once the thickness of EDT hits 180 nm, only BHJ devices have shown a higher absorption over the wavelength range of 800 nm to 1100 nm. Finally, the absorption for IR light from 700 nm to 1200 nm reaches over 0.9 absorbance units when 240 nm thickness of PbS EDT layer was incorporated into the photovoltaic devices, and this is a much-improved value compared with the devices with a 60 nm PbS EDT layer. Regarding the comparison between BHJ and PHJ devices, whereas the BHJ device with 180 nm PbS EDT layer had a significant increase in absorption for light from 800 nm to 1100 nm, the absorption of BHJ devices were just marginally higher than the PHJ devices. Thus, thickening the PbS EDT layer from 60 nm to 240 nm dramatically improves the absorption for NIR light for both BHJ and PHJ devices, so the absorption differences between BHJ and PHJ devices is limited. This may suggest that the improvement in J_{sc} and EQE for BHJ devices is not dominated by light scattering effects.

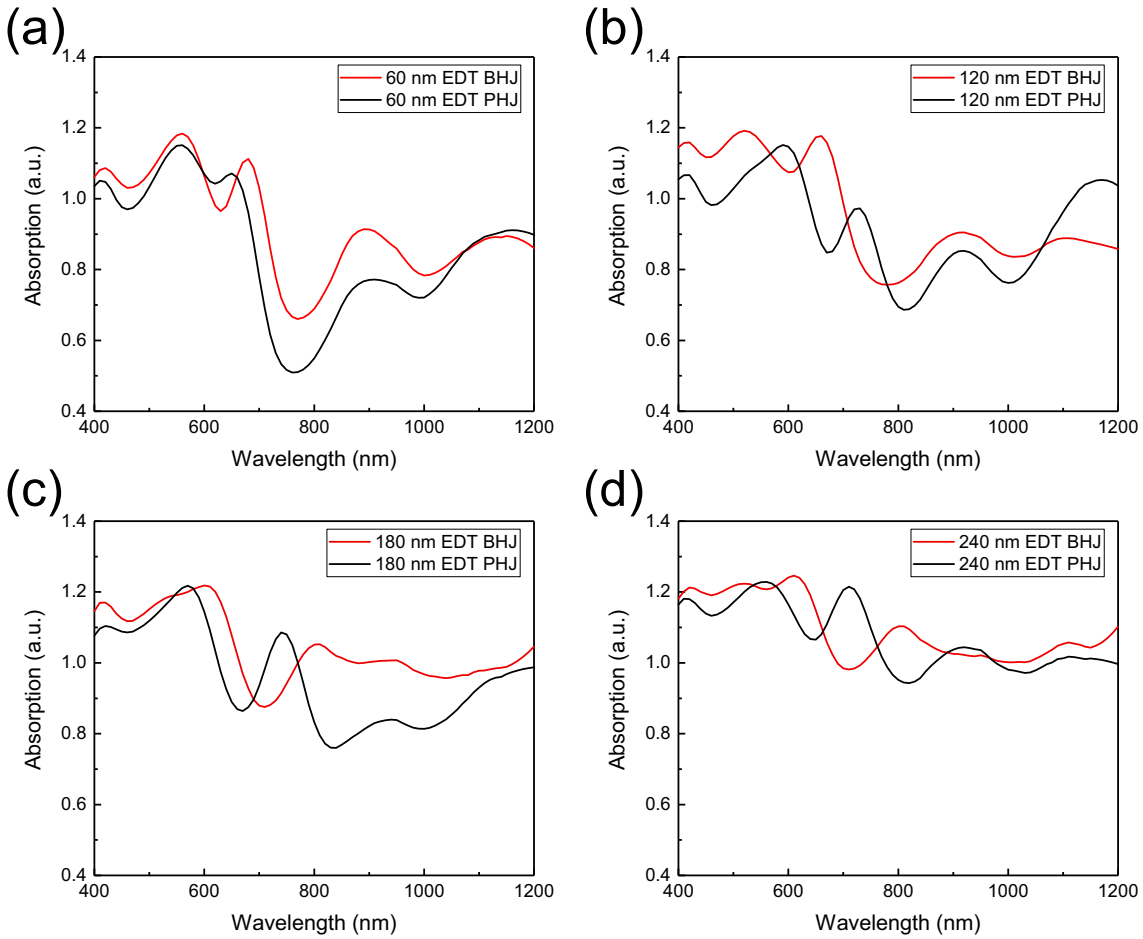


Figure 6.7: Absorbance of (a) BHJ devices and (b) PHJ devices with EDT thicknesses of 60 nm (black solid line), 120 nm (red solid line), 180 nm (blue solid line), 240 nm (green solid line) from 400 nm to 1200 nm.

The absorption measurement revealed the enhancement in the light absorption with light scattering effect by SWNT-P3HT composite in PbS EDT layer. This means that the enhancement in light harvesting is mainly due to the enhancement in the carrier collection after the absorption of the light in these photovoltaic devices. To visualize the efficiency after the absorption of the light to devices, internal quantum efficiency (IQE) plots were created by integrating the EQE and absorption measurements. IQE can be calculated by the following equation, where %T is percent transmittance, and A is absorbance in an absorbance units.

$$IQE = \frac{EQE}{(100 - \%T)/100} = \frac{EQE}{(100 - 10^{(2-A)})/100} \tag{6.1}$$

Calculated IQEs for BHJ and PHJ devices are compared in figure 6.8a-d regarding several different thicknesses of PbS EDT layers in each device. For devices with a 60 nm PbS EDT layer, the BHJ devices had almost identical IQE from 400 nm to 1100 nm. When the thickness of PbS EDT was increased to 240 nm, the BHJ devices had a higher efficiency to generate collected carriers from the absorbed light, especially in the visible and NIR region, as presented in figure 6.8b-d. Also, BHJ devices with thicker PbS EDT layers seemed to have a higher IQE at around 700 nm compared with the PHJ devices. As can be seen in figure 6.7, the light absorbed most effectively with extra thick PbS EDT layers was around 700 nm. This means that devices with higher IQE around 700 nm could effectively transport carriers generated by extra absorption. Thus, the IQE results suggest that BHJ devices have better carrier transport compared with PHJ devices, especially for light harvested with extra thick PbS EDT layers.

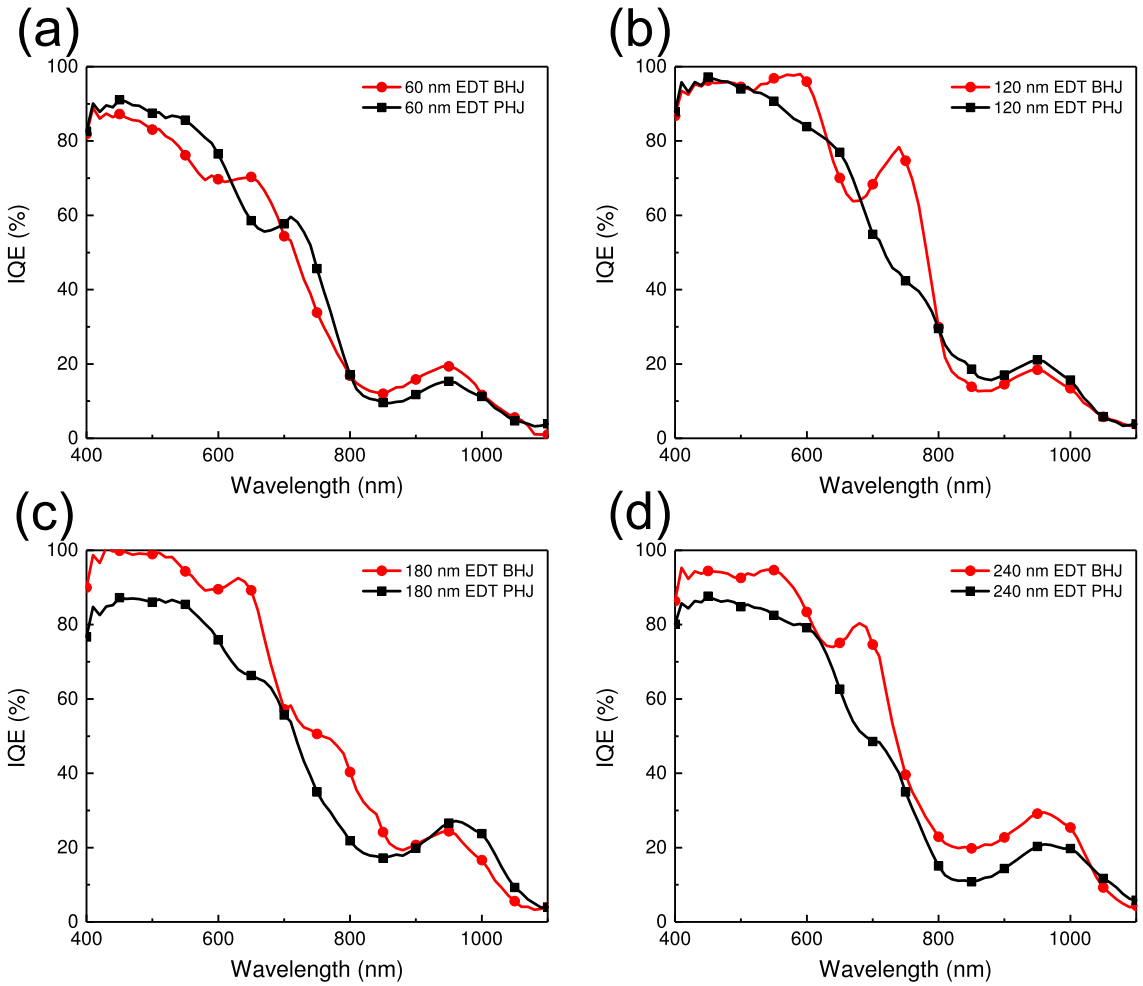


Figure 6.8: Comparison of BHJ (red solid line with circular symbols) and PHJ (black solid line with square symbols) in internal quantum efficiency (IQE) with (a) 60 nm, (b) 120 nm, (c) 180 nm, and (d) 240 nm EDT thickness from 350 nm to 1100 nm.

Electronic impedance spectroscopy was also done for these BHJ and PHJ devices, showing a much lower charge transfer resistance for BHJ devices. Electronic impedance spectroscopy measurements were performed to explore the charge dynamics and measure charge transfer resistance values in the photovoltaic devices under illumination. The wavelength of the light was set to 617 nm because wavelengths shorter than 600 nm will give more absorption to the SWNT-P3HT composite which is not useful to observe the charge transfer from PbS to SWNT-P3HT. Figure 6.9a and figure 6.9b are the impedance spectra under illumination for control and SWNT samples with the bias voltage equal to the photovoltaic devices V_{oc}. A single RC-model was used to fit the

Nyquist plots obtained by impedance spectroscopy for a n-i-p heterojunction solar cell. The equivalent circuit based on the RC-model is shown in figure 6.9c, where R_{ser} is the series resistance, C_{tot} is the total capacitance in the solar cell, and R_{char} is the charge transfer resistance in the solar cell. Values of these parameters obtained by fitting are listed in table 6.1. With the BHJ structure, the charge transfer resistance was 4 to 5 times smaller than for the PHJ devices, as can be seen in table 6.1. These results further suggest that employing the bulk heterojunction structure will help to transport generated carriers out efficiently from photovoltaic devices. This improvement in charge resistance was seen as the improvement in IQE in figure 6.8 and ultimately in the J_{sc} values observed for BHJ devices.

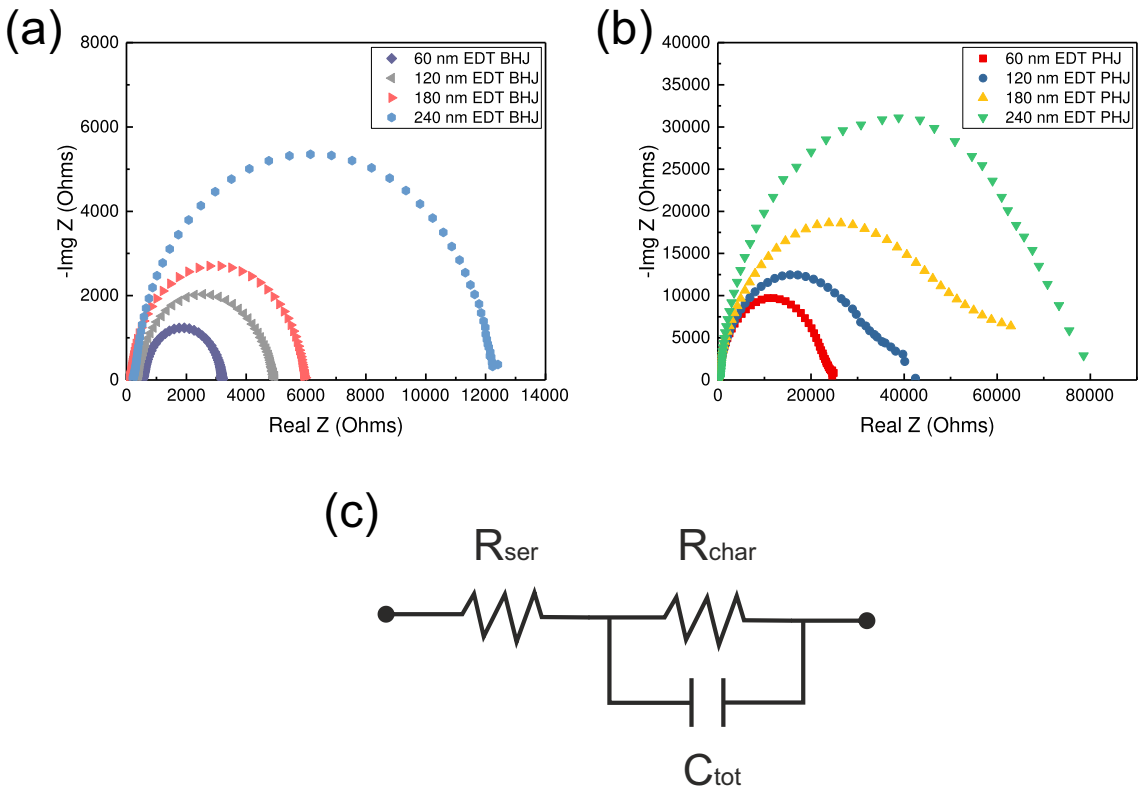


Figure 6.9: Nypuist plots of impedance spectra of (a) BHJ and (b) PHJ devices under 617 nm wavelength light illumination at a bias voltage equivalent to solar cells open circuit voltage. (c) Equivalent circuit of RC single model which was used to fit the impedance spectra, where R_{ser} is the series resistance, C_{tot} is the total capacitance in the solar cell, and R_{char} is the charge transfer resistance in the solar cell.

Table 6.1: List of parameters obtained by fitting impedance spectra using the equivalent circuit shown in figure 6.9. The active area of the device is 0.04 cm^{-2}.

EDT thickness (nm)	device type	R_{ser} (Ω)	R_{char} (Ω)	C_{tot} (F)
60	BHJ	493.2	1180	1.749×10^{-9}
60	PHJ	325.3	5249	1.346×10^{-9}
120	BHJ	175.9	1432	2.586×10^{-9}
120	PHJ	268.3	5572	2.261×10^{-9}
180	BHJ	61.73	1931	3.780×10^{-9}
180	PHJ	352.8	8628	2.853×10^{-9}
240	BHJ	112.5	2682	3.852×10^{-9}
240	PHJ	451.3	111015	3.459×10^{-9}

6.3 Conclusions

Bulk heterojunction structures of PbS EDT layer and SWNT-P3HT composite improved the charge transfer from the PbS EDT compared with planar heterojunction devices of PbS EDT and SWNT-P3HT in PMMA matrices. To test the effect of charge transfer by SWNT-P3HT, the thickness of the PbS EDT photoactive layer was increased from 60 nm to 240 nm to obtain higher absorption. With the enhancement in charge transfer, a reduction in monomolecular carrier recombination has been observed by the intensity-dependent V_{oc} measurement. This reduction of the non-radiative carrier recombination ultimately helped PV devices with the bulk heterojunction between PbS EDT and SWNT-P3HT to improve the fill factor of the devices and maintain the voltage of the devices compared to planar heterojunction PbS EDT and SWNT-P3HT devices as the thickness of the PbS EDT layer increased. Moreover, an absorption study of PbS CQD PV devices with various PbS EDT layer thicknesses has been conducted, and with a 240 nm PbS EDT layer, the NIR light was absorbed more strongly, which was not achieved without thicker layers of PbS EDT. Although the improvement of absorption has been observed for both BHJ and PHJ devices, BHJ devices exhibited better IQE for NIR light compared with PHJ devices. This eventually gave BHJ devices a higher J_{sc} value than PHJ devices. For example, BHJ devices have shown 8% improvement in J_{sc} when the thickness of PbS EDT layer is 240 nm, and recorded

the highest J_{sc} values. With those factors discussed above, BHJ devices have recorded the highest efficiency of 11.5% when the EDT thickness is 120 nm.

Chapter 7

PbS CQD Solar Cells with Graphene Electrode

7.1 Introduction

1-D carbon nanomaterials single-walled carbon nanotubes have been utilized to improve the efficiency of PbS CQD solar cells by both optical and electronic enhancements. In this chapter, PbS CQD solar cells using graphene as a highly-conductive electrode were fabricated and tested.

PbS CQD PV has been struggling with the V_{oc} and FF values because of the bandgap of the photoactive layer and resulting built-in potential. The most significant cause of this deficit in both V_{oc} and FF is the presence of sub-bandgap trap states on the QDs.[16,88,89] Lots of work has been reported on the improvement of CQD passivation techniques to reduce the trap states on CQDs.[18,23,73,90,94,95] In this chapter, I approach the enhancement of V_{oc} and FF by a device architectural approach rather than improving the surface chemistry of the CQD photoactive layer. In the photovoltaic devices I examine here, the graphene layer is used as the highly-conductive electrode to minimize voltage loss in the device.

Graphene is known for its particular characteristic in an electronic band structure called Dirac cones.[117,122] With this feature, the movement of charge carriers in graphene could be described as a massless fermion, which brings about the ultra high carrier mobility. With that exceptional carrier mobility, I hypothesized that graphene can be

a good candidate for a highly-conductive electrode.

7.2 Results and Discussion

7.2.1 Device architecture and performance

In this chapter, both control devices without graphene layers, and devices with a graphene layer in between the PbS photoactive layer and Au top contact were compared in performance. The main photoactive layer in these devices is a PbS CQD thin film with lead iodide and ammonium acetate (PbI_2/AA) ligands which is covered by a PbS EDT hole transporting layer. Figure 7.1 is the schematic to show how to transfer a graphene layer on top of the device. All graphene layers covered with PMMA on Cu substrates in this chapter were supplied by Dr. Yuewen Sheng in the Department of Materials, the University of Oxford as a part of collaborative work. First, 3-hour long etching of the Cu substrates was done by a 0.2 M aqueous solution of ammonium persulfate, followed by three-time soaking in distilled water for 15 minutes each time. After rinsing with distilled water, graphene was fished out onto the desired substrates. After the coarse evaporation of water, all samples were kept in the low air pressure (-40 kPa) overnight. Next, some samples were annealed at 120 °C as annealing was thought to give graphene better adhesion to the substrates. Finally, the PMMA coating was dissolved in an acetone bath for 10 mins. After this graphene transfer process, a Au top contact was evaporated onto the functional layers to make the active device area of 0.04 cm^2. Then the functional layer between each active area including the graphene layer was scraped off to make pixels isolated from each other.

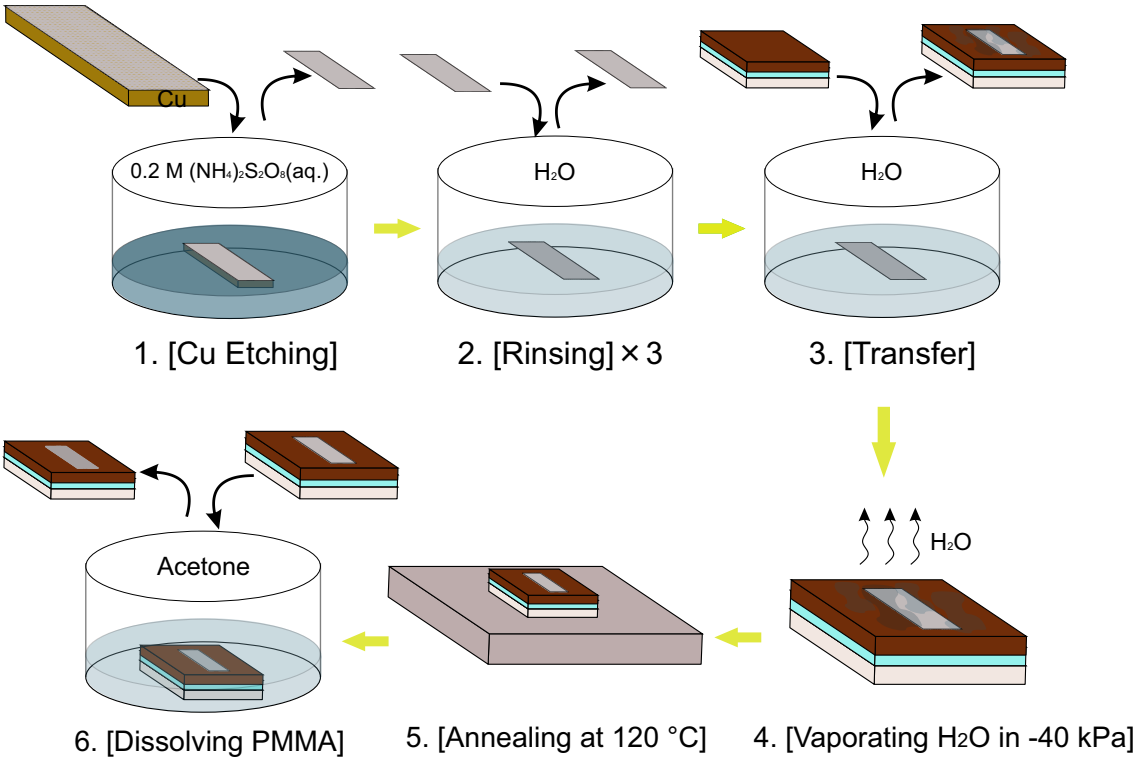


Figure 7.1: Schematic illustration of the graphene transfer process. Graphene layer was sandwiched by the copper substrate and the PMMA film after CVD growth and PMMA shielding.

Figure 7.2a illustrates the architecture of the photovoltaics fabricated. All functional layers of the photovoltaic device are solution processed except for the sputter coated indium tin oxide (ITO) electrodes on glass substrates and thermally evaporated gold as top contact electrode. On top of the ITO, an electron transporting zinc oxide layer, prepared by a sol-gel method,[165] is deposited and followed by a CQD absorber layer which is composed of PbS CQD stabilized by lead iodide and ammonium acetate. Through the solution-phase ligand exchange process, oleic acid (OA) ligands coordinating to PbS nanocrystals were exchanged by the anionic iodide ligands and cationic ammonium ligands (PbS-PbI_2/AA). On top of PbS-PbI_2/AA, 40 nm of PbS thin film was spun-coated with solid-state ligand exchange with 1.2-ethanedithiol (PbS-EDT). This PbS-EDT layer is expected to have better stability than PbS-PbI_2/AA and have an electron blocking functionality as it has p-type characteristic compared with the

intrinsic characteristics of PbS-PbI_2/AA. For graphene incorporated devices, graphene transfer was done after these spin-coating procedures. Finally a top contact Au electrode was thermally evaporated. Compared with the control sample, the graphene layer was inserted between the PbS thin film and Au cathode in the photovoltaic device (graphene device). For both control and graphene devices, device performance was analyzed with or without an annealing treatment after the graphene deposition to pursue the optimum way to incorporate the graphene layer in the PbS CQD PV devices. Figure 7.1b and 7.1c summarize the energy levels of each functional layer in graphene solar cells, and how band bending occurs in the actual devices under thermal equilibrium. Both electrodes have ohmic contact as n-type semiconductor ZnO has a higher Fermi level than the Fermi level of ITO, and p-type semiconductor SWNT/P3HT has a lower Fermi level than the Fermi level of Au and graphene. The type of all heterojunctions in these photovoltaics is the type-II heterojunction because each semiconductor overlaps each other and shifts slightly to lower energy level towards Au cathode.

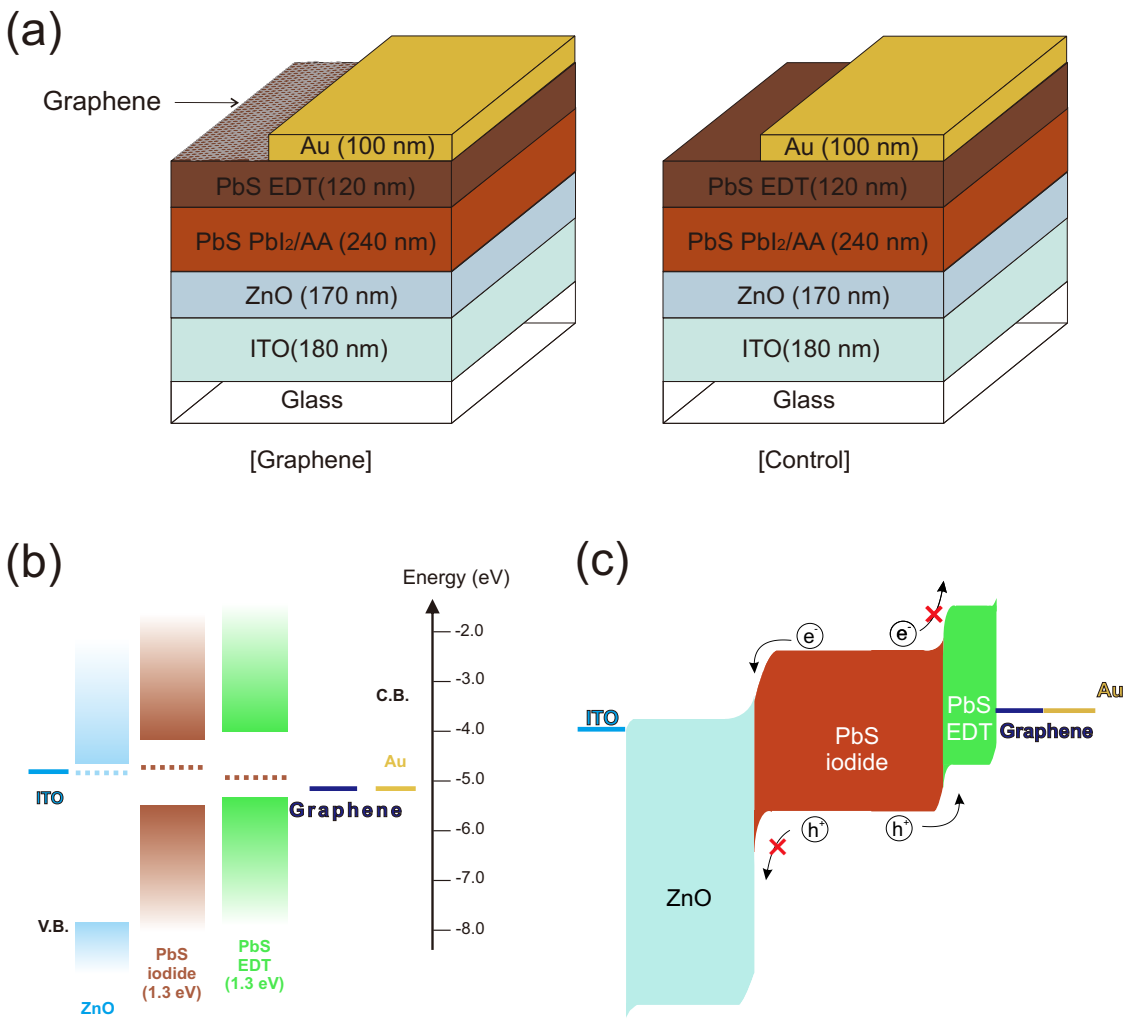


Figure 7.2: (a)Schematic illustration of PbS CQD photovoltaic device using graphene between PbS-EDT (120 nm) and Au (100 nm) cathode as a highly-conductive electrode, and PbS CQD photovoltaic device without graphene as a control. (b) Energy band diagram showing the energy levels of all functional layers in graphene devices. (c) Schematic illustration of band bendings in the graphene devices.

Figure 7.3 summarizes the photovoltaic performance of control devices and graphene incorporated devices under AM1.5 illumination with variations of annealing and acetone bath treatment during device fabrication. First, both control and graphene devices without annealing process have shown higher J_{sc} and V_{oc} than all the annealed devices. Although the annealed control devices had less than half of the J_{sc} value compared with non-annealed control samples, the annealed graphene sample only had 20% reduction of J_{sc} compared with non-annealed graphene devices. The reason why graphene de-

vices have higher J_{sc} values after annealing is the shielding effect of the PMMA layer covering the graphene during annealing. In V_{oc}, there is a trend that devices which had an acetone bath treatment after the annealing (Ann. graphene and Ann. bath control in figure 7.3b) have lower V_{oc} than other devices. The fill factor of the annealed graphene sample is approximately 15% lower than other samples. Overall, there is a discrepancy in power conversion efficiency between non-annealed graphene or control samples and annealed graphene or control samples.

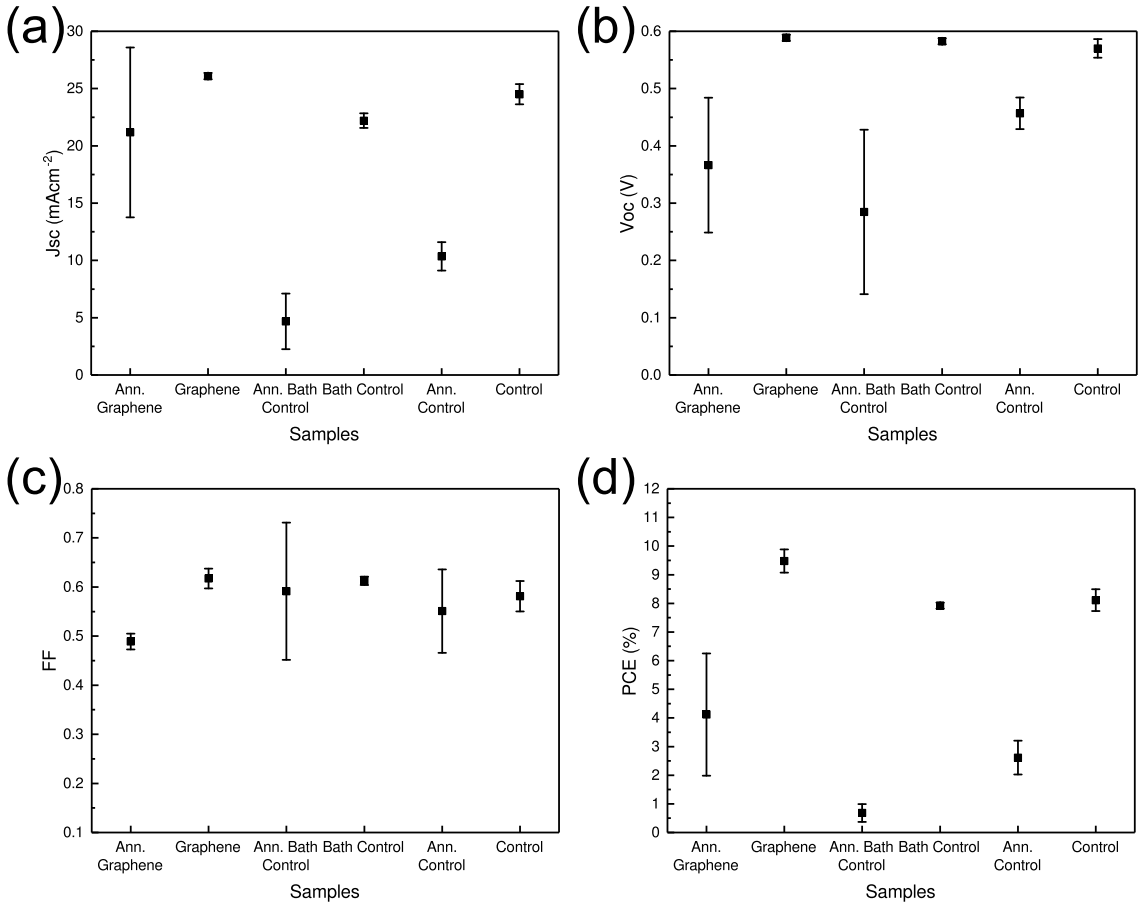


Figure 7.3: (a) J_{sc}, (b) V_{oc}, (c) FF, and (d) PCE of graphene incorporated devices with annealing (Ann. Graphene), of graphene integrated devices without annealing (Graphene), of control devices with annealing and acetone bath (Ann. Bath Control), of control devices soaked in an acetone bath without annealing (Bath Control), of control devices with annealing but without acetone bath (Ann. Control), and of control devices without either annealing and acetone bath (Control) under AM1.5 illumination at day 1 of storage in the air. The reported mean values and error bars for all parameters were calculated from a sample of 12 devices.

7.2.2 Influence of annealing and acetone bath

As presented in figure 7.3, annealing had a significant impact on the device performance although it was expected to give better adhesion of the graphene layer to the PbS CQD photoactive layer. To understand the adverse effect of annealing on the functional layers in the devices, some chemical and physical measurement have been done. FT-IR measurement were conducted to observe any chemical changes in the ligands coordinating to the PbS nanocrystals in the thin films. As shown in figure 7.4b, FT-IR exhibit that the PbS thin film with PbI_2/AA has lost a peak at 3400-3300 cm^{-1} corresponding to the N-H bond stretching of the primary amine after both annealing and acetone bath treatment. This loss of the peak suggests that both annealing and an acetone bath could remove the ammonium cation coordinating to the CQD. The reduction of the ligands in CQD induces sub-bandgap trap states, which causes the intraband carrier recombination and ultimately degradation of the voltage. Hence, the removal of the ammonium cation in the PbS-PbI_2/AA with annealing and acetone bath treatment has been shown, and this is suggested to be the cause of the lower V_{oc} in both graphene and control devices after either annealing or an acetone bath treatment.

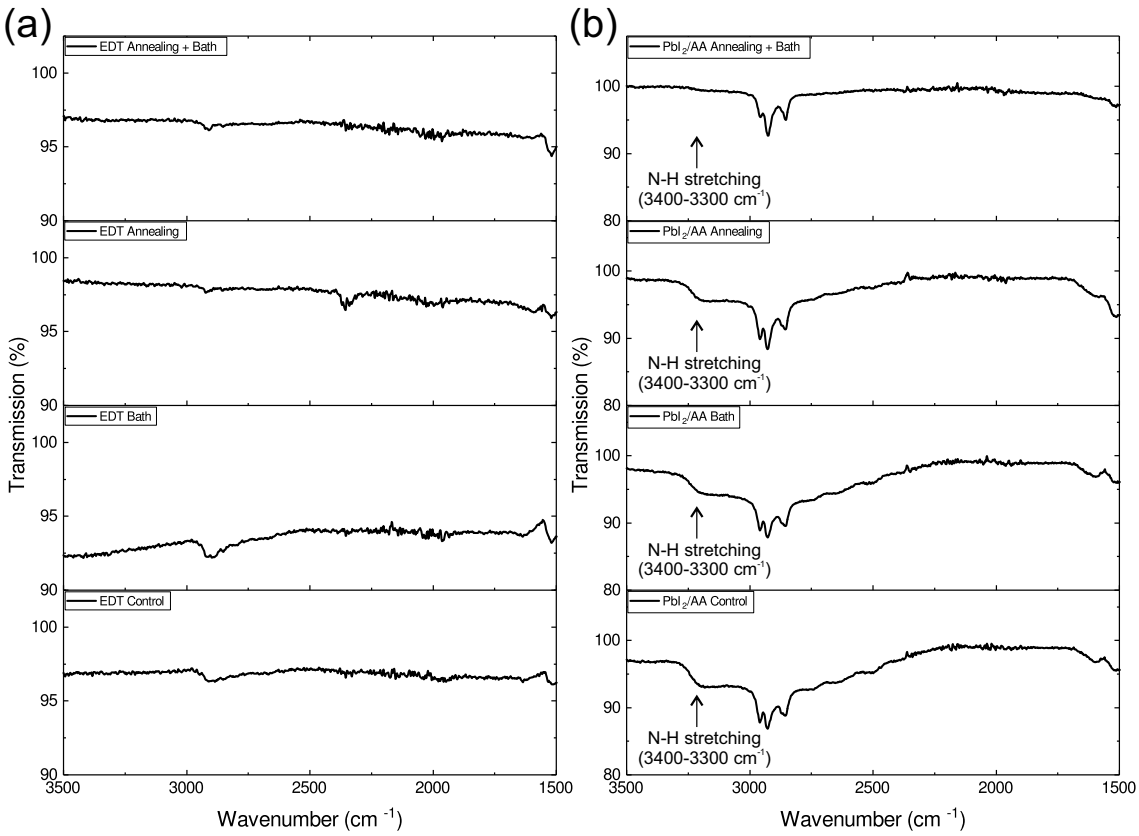


Figure 7.4: FT-IR transmission spectra of (a) PbS EDT layer, and (b) PbS PbI_2/AA layer on glass substrates from wavenumber 3500 cm^{-1} to 1500 cm^{-1}. Both EDT and PbI_2/AA samples have been treated in an acetone bath (Bath in a figure), Annealing (Annealing in a figure), or both annealing and acetone bath (Annealing + Bath in a figure).

X-ray photoelectron spectroscopy (XPS) was performed to measure the state of oxidation in both PbS-EDT and PbS- PbI_2/AA films after annealing and bath processes. Figure 7.5a compares the binding state of the O 1s orbitals in PbS PbI_2/AA films. All thin films show Pb-OH bonds which are known to exist after the hot-injection synthesis method of PbS CQDs. There is a COO functional group from the acetate in ammonium acetate during the solution-phase ligand exchange process for all samples as well. The only difference after the annealing and acetone bath is the emergence of Pb-O bonding. This Pb-O bond suggests that annealing would make a dangling bond on Pb atoms and acetone will further oxidize Pb atoms by donating oxygen to these Pb atoms. Contrary to the control PbS PbI_2/AA sample, the PbS EDT control

sample showed a higher count intensity in general as it has been treated by solid-state ligand exchange with methanol solution which would make a Pb-OH during the ligand exchange process. Compared with that control sample, annealing creates Pb-O bonds by creating dangling bonds. After the acetone bath treatment following annealing, a peak corresponding to COO bonds appeared as COO in the acetone binds to the dangling bonds on Pb atoms created by annealing. Thus, XPS measurements suggest that annealing triggers Pb atoms to have more dangling bonds and the acetone bath treatment would further oxidize the CQDs or make carboxyl bonds to Pb atoms with dangling bonds.[195,196]

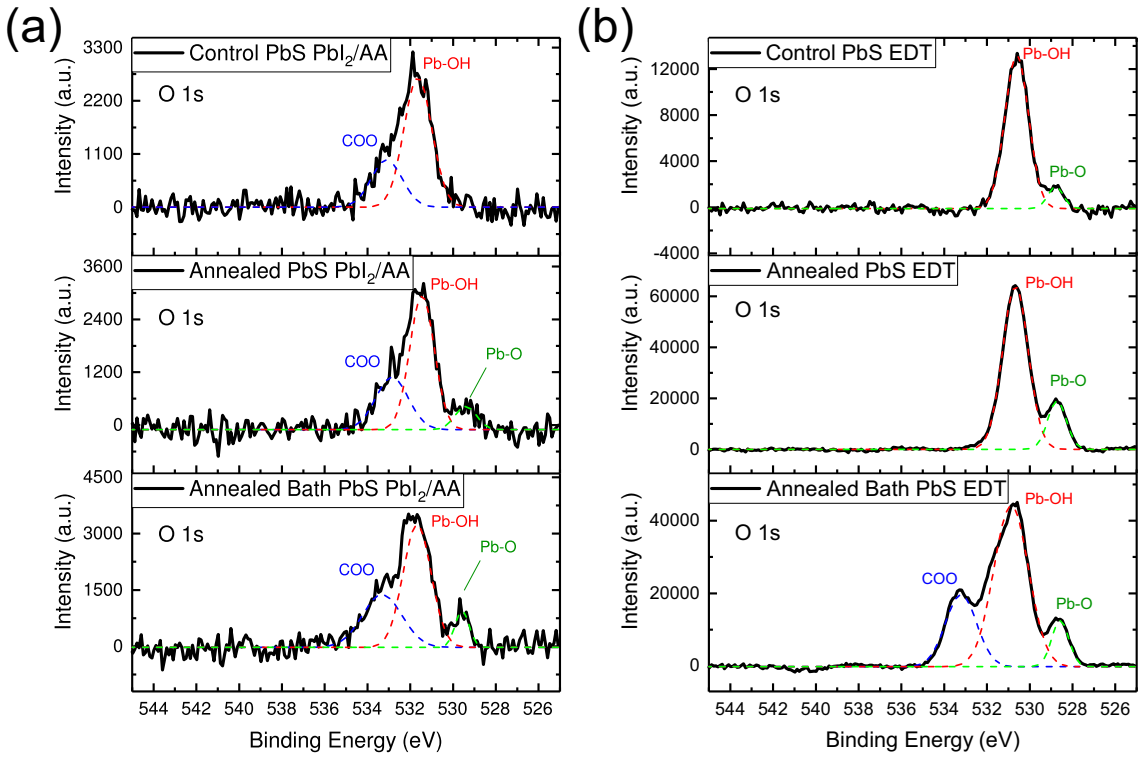


Figure 7.5: X-ray photoelectron spectra of (a) PbS-PbI_2/AA thin film and (b) PbS-EDT thin film samples on glass from 525 eV to 545 eV of binding energy corresponding to the O 1s orbital. The intensity peak of the counts for that energy range is analyzed by Gaussian distributions and illustrated by dashed lines in three different colours (COO in blue, Pb-OH in red, and Pb-O in green).

To further understand the differences in J_{sc} by various treatment and the presence of graphene in devices, EQE measurements were carried out for devices with variations

in the presence of graphene, or in the annealing and acetone bath treatment. One interesting difference between non-annealed samples and annealed samples lies in the wavelength range 800 nm -1100 nm in figure 7.6b-c. Contrary to the non-annealed samples which have a weak peak at 970 nm, the annealed samples do not show that peak but have had the EQE increase towards 1100 nm. This phenomenon might suggest that there are more intraband trap states which cause more radiative carrier recombination, which will eventually make the excitation peak energy small (of high wavelengths).

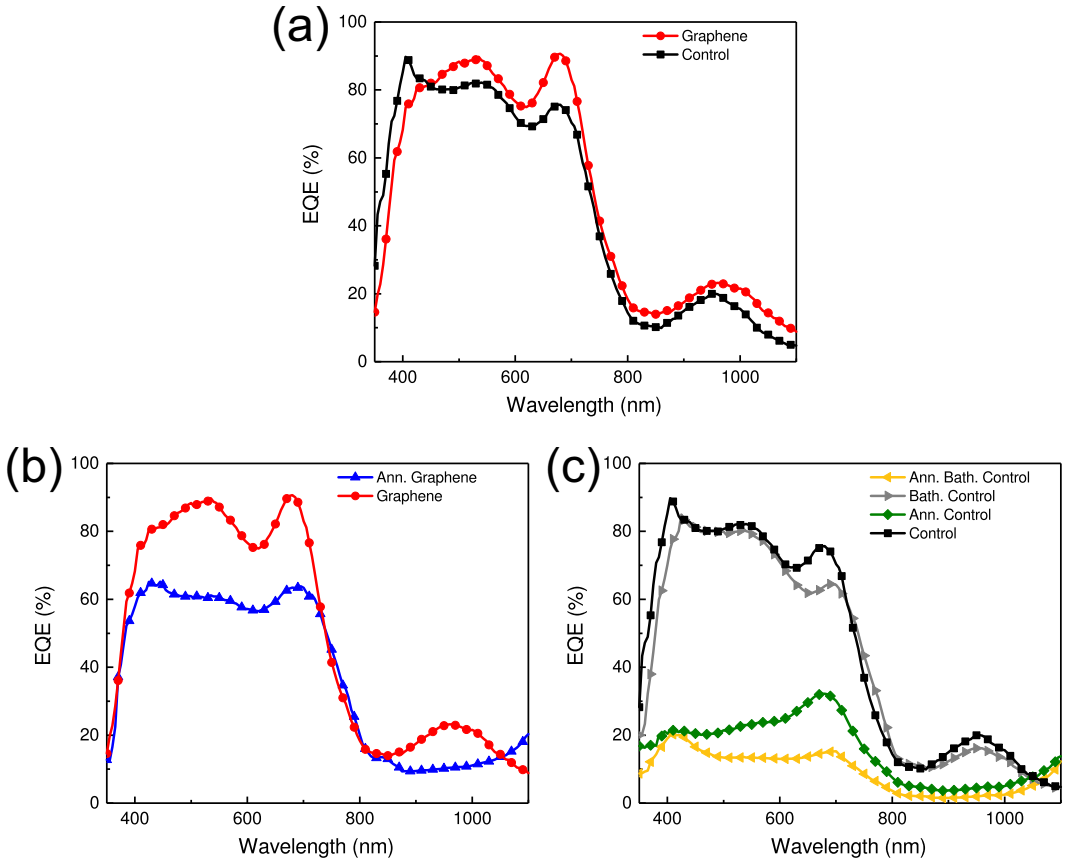


Figure 7.6: (a) External quantum efficiency comparison of control (black squares), and graphene device (red circles). (b) External quantum efficiency comparison of annealed graphene device (blue top-pointing triangular symbols), and graphene device (red circles). (c) External quantum efficiency comparison of control samples with annealing and acetone bath (yellow left-pointing triangular symbols), with only an acetone bath treatment (Grey right-pointing triangular symbols), with only annealing treatment (green diamonds), and with no treatment (black squares).

Finally, Raman spectroscopy mapping has been done to confirm the presence of graphene on top of PbS, with annealing and without annealing. Raman spectroscopy is the most common technique to characterize some properties as layer thickness, charge and strain, and defect states. It is known that monolayer graphene gives strong peaks around 1580 cm^{-1} and 2700 cm^{-1} of the Raman shift. The first peak is called the G-band and is caused by the stretching of the C-C bond in sp^2 carbon systems. The latter is named as a 2D peak corresponding to the phonon resonance. Also, there is a weak peak at around 1350 cm^{-1} Raman shift which is called as D-band caused by the disorder in sp^2. The ratio of D-band and G-band peaks (D/G ratio) is used to quantify the degree of the deficiency in the 2D materials. Figure 7.7 compares the Raman spectroscopy mapping of the non-annealed and annealed samples with representative spectra of the area covered by graphene and the area which was not covered by graphene layer on both samples. This mapping confirms that the non-annealed sample could keep graphene covering the surface of PbS. In addition to that point, the D/G ratio for both samples have shown a similar value (0.118 for non-annealed, and 0.116 for annealed). Thus, Raman spectroscopy confirms that the graphene layer is present on PbS thin films both with and without annealing.

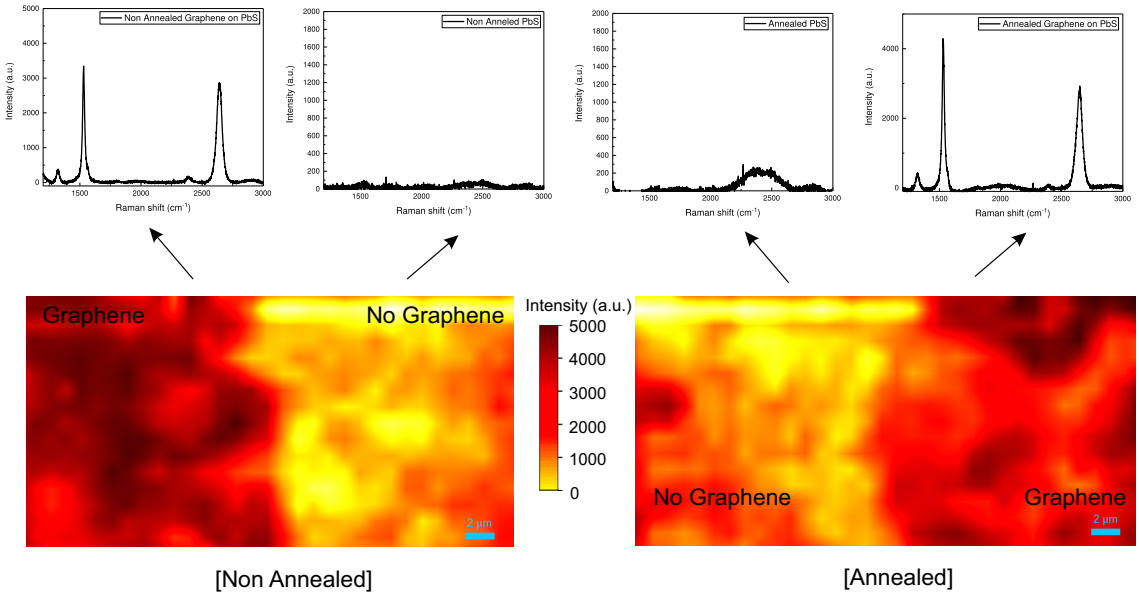


Figure 7.7: Raman mapping at the boundary of pristine PbS layer and graphene on top of PbS layer with or without annealing. Mapping has been done by taking an integral of the spectra from 1500 cm^{-1} to 1700 cm^{-1} in a raster of 17 $\times$ 38 dots over an area of 16.29 μm$\times$ 36.61 μm at the edge of the graphene strip on PbS CQD thin films.

7.2.3 Comparison of control samples and graphene samples

In the previous section, the adverse influence of annealing before an acetone bath treatment has been explored by chemical and physical measurement techniques. In this section, there are side-by-side comparisons of the performance from both control devices and graphene devices without any annealing treatment. Figure 7.8 compares the JV curves of the PbS photovoltaic device without graphene which was not treated by any annealing or an acetone bath (control), and PbS photovoltaic device with graphene with only the acetone bath treatment (graphene). The JV curve of the median graphene device has a higher maximum power point compared with the JV curve of the median control device.

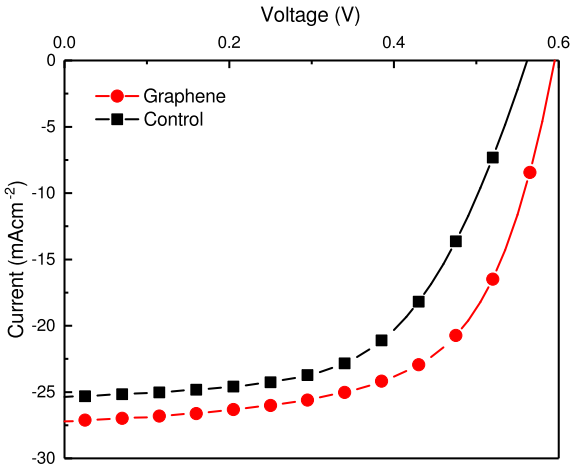


Figure 7.8: JV curve comparison of graphene device (a solid red line with red circular symbols), and of control device without an acetone bath treatment (a solid black line with black square symbols) under AM1.5 illumination.

Figure 7.9a-d summarizes the device performance of the graphene and control devices. All three parameters (J_{sc}, V_{oc}, and FF) have shown better values for the graphene devices compared with control devices. Although the V_{oc} for graphene devices were marginally better than the control devices, both J_{sc} and FF for the graphene devices had considerably higher values than the control devices. Overall, the graphene devices had 13% improvement in overall efficiency compared with the control devices.

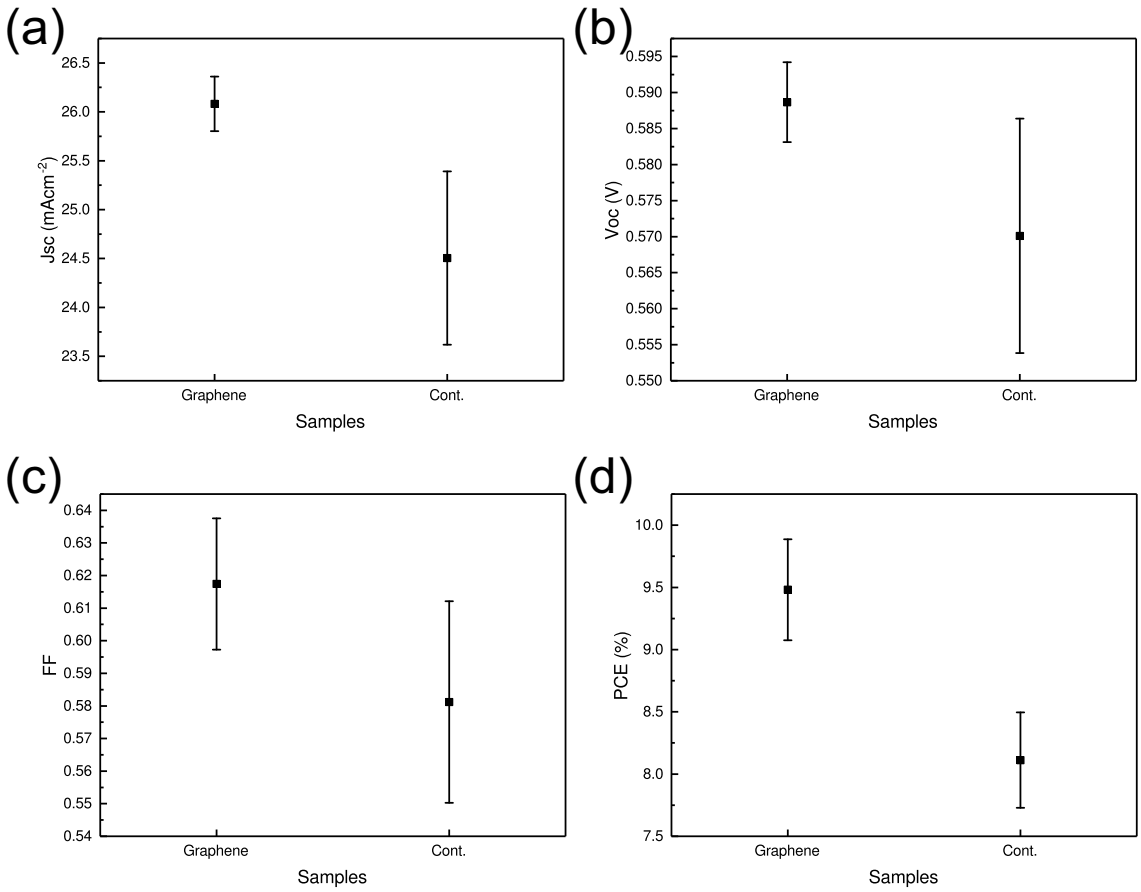


Figure 7.9: (a) J_{sc}, (b) V_{oc}, (c) FF and (d) PCE of graphene incorporated devices without annealing (Graphene), of control devices without annealing (Control) under AM1.5 illumination at day 1 of storage in the air. The reported mean values and error bars for all parameters were calculated from a sample of 12 devices.

As shown in figure 7.9a, J_{sc} has been improved with a graphene layer inserted between the PbS EDT layer and Au electrode. To see if the graphene layer enabled PbS thin film to absorb more light, absorbance measurements were conducted with integrating sphere. The results of the measurement are summarized in figure 7.10a. Except for the absorption peak at around 700nm, the graphene device has shown higher absorbance than the control device. This might be due to the better refractive index of graphene (refractive index n = 2.35)[197] to have a better reflection from the back Au (refractive index n = 0.13833)[198] electrodes. This improvement in absorbance is prominent at 800 nm. Although the absorbance of the control device hit as low as 0.68 absorbance unit, the graphene device has shown 0.82 absorbance unit as the minimum

peak of absorbance.

Moreover, internal quantum efficiency (IQE) analysis has been done by combining results from the EQE and absorbance measurements. Figure 7.10b compares the IQE of the graphene device and the control device. Although graphene devices have shown superior IQE values for visible light (up to 700 nm), the IQE of graphene device was not notably higher than control device for NIR illumination. This IQE result matches with the position of the graphene layer. Light with a shorter wavelength would be absorbed more to the front side of the photovoltaic device while graphene is positioned at the rear side of the device. Regarding the diffusion length of carriers in the PbS CQD thin film, better carrier transfer by graphene would be more effective to the carriers generated at the front side of the photovoltaic device. Hence, improvement in both absorption and internal carrier transfer in the graphene device is confirmed and be supports of higher J_{sc} value for graphene device.

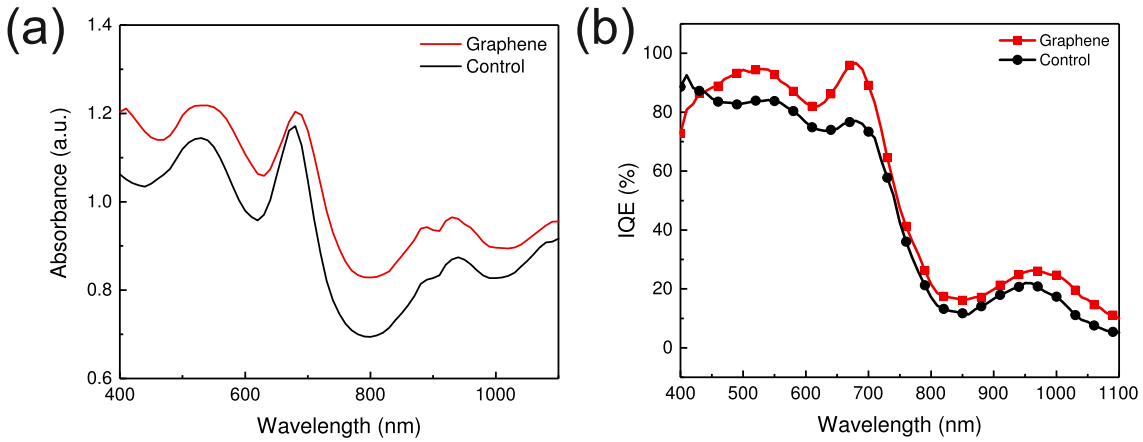


Figure 7.10: (a)Absorbance of graphene device (red solid line), and control device (black solid line) from 400 nm to 1200 nm. (b) Comparison of graphene devices (red solid line with square symbols) and control devices (black slid line with circular symbols) in internal quantum efficiency (IQE) from 350 nm to 1100 nm.

In contrast to the Au electrode alone, the graphene layer should facilitate charge extraction, which would result in a reduction in non-radiative recombination at this interface. As shown in figure 7.9c, the graphene device without annealing recorded the best fill factor compared with other devices. To examine the state of charge carrier

recombination, measurements of V_{oc} under different white light intensities (figure 7.11a-c) were carried out. The dependence of V_{oc} on light intensity should reflect both monomolecular and bimolecular recombination as all of the charges recombine at the open-circuit condition. In figure 7.11c, the slope of the graphene device is 2.91kT/q which is flatter than the slope of 3.32kT/q from the control device. This result suggest that the graphene device has less monomolecular carrier recombination than the control device.

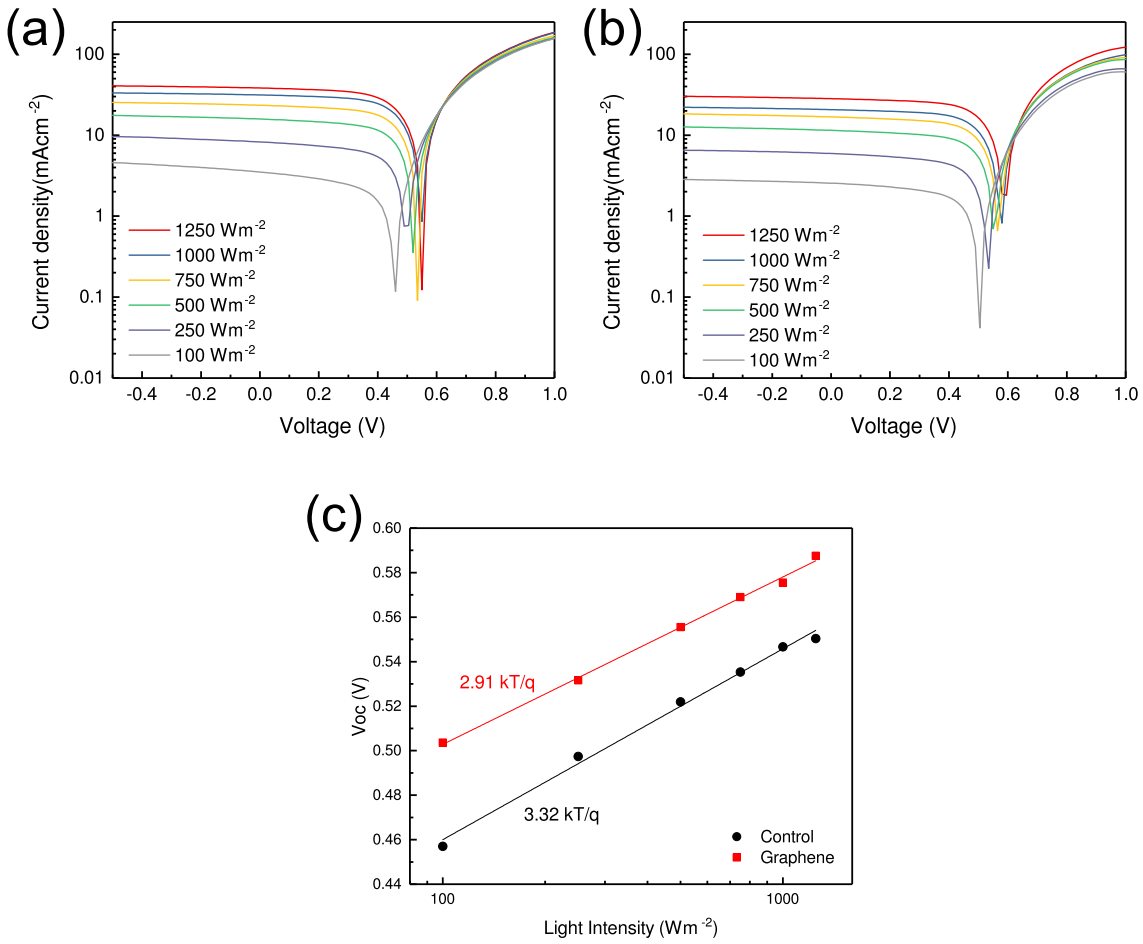


Figure 7.11: Plots of the logarithm of current desnity *versus* voltage under light intensity of 1250 Wm^{-2}, 1000 Wm^{-2}, 750 Wm^{-2}, 500 Wm^{-2}, 250 Wm^{-2}, and 100 Wm^{-2} for (a) control device, and (b) graphene device. (c) V_{oc} of the control device (without graphene: red squares) and graphene device (with graphene: black circles) under different illumination intensities. The slope of the linear fitting to V_{oc} *versus* logarithm of light intensity was analysed as the factor to the thermal voltage.

Electronic impedance spectroscopy was done for control and graphene devices which

has shown a much lower charge transfer resistance for graphene device. Figure 7.12a-c are the impedance spectra under illumination for control and graphene samples with the bias voltage equal to photovoltaic devices V_{oc}. A single RC-model was used to fit the Nyquist plots obtained by impedance spectroscopy for either n-i-p planar heterojunction solar cell. The equivalent circuit based on RC-model is used to fit the data, where R_{ser} is the series resistance, C_{tot} is the total capacitance in the solar cell, and R_{char} is the charge transfer resistance in the solar cell. Values of these parameters obtained by fitting are listed in Table 7.1. With the graphene layer, the charge transfer resistance had a slight decrease from 51183 Ω to 20569 Ω. These results further suggest that employing the graphene could improve charge transport throughout the device.

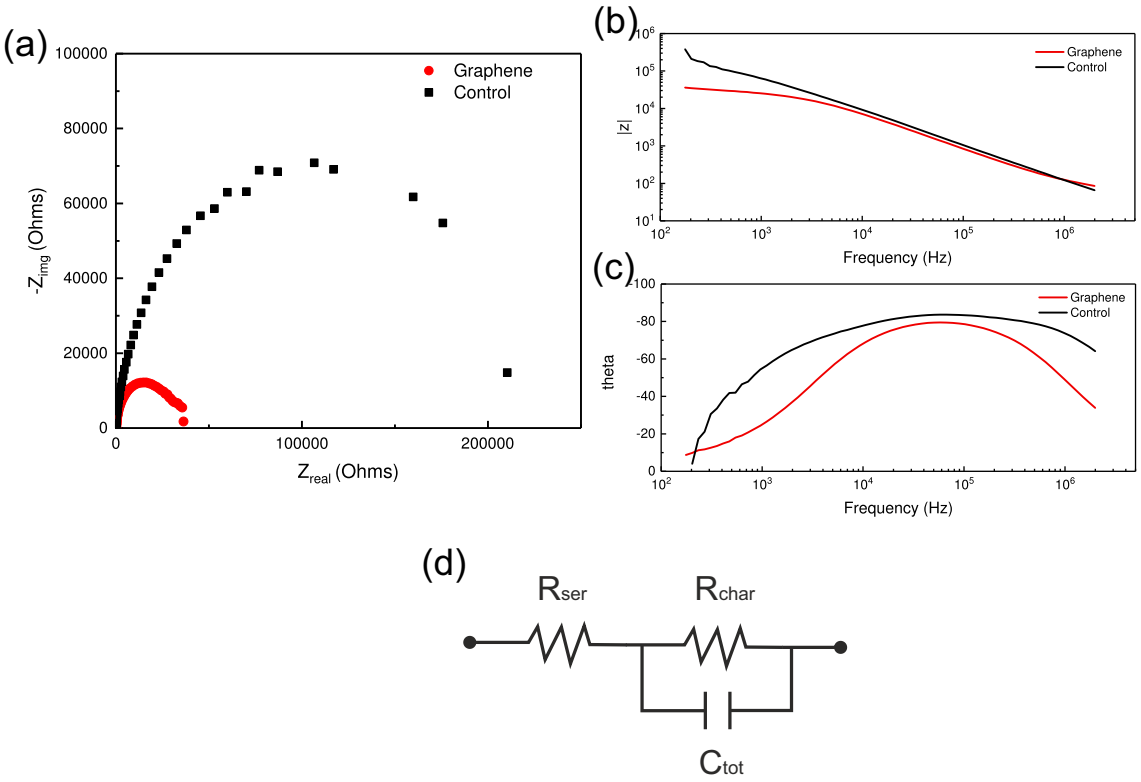


Figure 7.12: (a) Nyquist plots of impedance spectra of control and graphene devices under 617 nm wavelength light illumination at bias voltage equivalent to solar cells open circuit voltage. (b) Impedance modulus |Z| *versus* frequency plots corresponding to the acquired Nyquist plots. (c) Phase angle theta *versus* frequency plots corresponding to the acquired Nyquist plots. (d) Equivalent circuit of RC single model which was used to fit the impedance spectra, where R_{ser} is the series resistance, C_{tot} is the total capacitance in the solar cell, and R_{char} is the charge transfer resistance in the solar cell.

Table 7.1: List of parameters obtained by fitting impedance spectra using the equivalent circuit shown in figure 7.12a-b. The active area of the device is 0.04 cm^{-2}.

Sample	R_{ser} (Ω)	R_{char} (Ω)	C_{tot} (F)
control	45.25	51183	1.552×10^{-9}
graphene	92.61	20569	1.951×10^{-9}

7.3 Conclusions

In this chapter, the optimized method to transfer the graphene layer to PbS CQD thin films has been studied, and the device performance of the PbS CQD solar cells using graphene and control PbS CQD solar cells were compared. First, the effect of the annealing and an acetone bath treatment to both graphene stacking and the quality of PbS CQD thin film have been explored. Although the annealing effect did not seem to have a significant impact on the stacking of the graphene layer onto PbS CQD thin film, annealing had a detrimental impact on PbS CQD devices. Among both graphene devices and control devices, the ones treated with annealing and an acetone bath have exhibited much lower performance compared with devices without those treatments. To understand the detrimental effect of those two treatments, FTIR and XPS measurements were done. FTIR indicated that the ammonium cation coordinating PbS nanocrystals was removed after those treatments. Additionally, XPS measurements confirmed oxidation of the PbS nanocrystals with both PbI_2/AA and EDT ligands after the annealing and an acetone bath treatment. The aim of annealing graphene devices is to make the graphene layer stack well to the PbS CQD thin film. However, Raman microscopic mapping revealed that the graphene layer without annealing appears as well adhering as the layer with annealing treatment. Not only the strength of the peaks but also the D/G ratio showing the degree of defects in the graphene layer exhibited similar values for both annealed and non-annealed samples. Thus, annealing is not necessary after the transfer of graphene onto PbS devices to make it well stacked.

In the latter part, side-by-side comparisons of the graphene device and the con-

trol device have been made. The graphene devices performed better over control devices in absorption and J_{sc}. Moreover, intensity-dependent V_{oc} and quantum efficiency measurements confirmed that the graphene device has less monomolecular carrier recombination and better IQE which results in a better V_{oc} and FF. To support these hypothesis of better charge transfer, AC impedance spectroscopy has done with the single RC model. As a result, charge transfer resistance of the graphene solar cell has reduced by nearly 40% compared to the control device. Thus the graphene layer has been proven to be a good highly-conductive electrode. This project used graphene as a highly-conductive electrode incorporated in PbS CQD solar cells, but it could be used as an interlayer for tandem structure solar cells to connect top cell and bottom cell in series.

Chapter 8

Conclusions

8.1 Summary of the thesis

In chapter 5, polymer-wrapped single-walled carbon nanotube (SWNT) films embedded in an insulating poly(methyl methacrylate) (PMMA) matrix and capped by a thermally evaporated Au electrode are investigated as a composite hole transport layer and optical spacer. Employing transient absorption spectroscopy I show that the SWNTs enhance the charge transfer rate from CQD to CQD, ZnO, or SWNT. In order to pinpoint the underlying mechanism for the improvement, I investigate the energetics of the junction by measuring the relative alignment of the band edges using Kelvin probe and cyclic voltammetry. Measuring the external quantum efficiency and absorption I find that the improvement is not mainly from electronic improvements but from enhanced absorption in the CQD absorber. I demonstrate experimentally and theoretically, by employing a transfer-matrix model, that the transparent PMMA matrix acts as an optical spacer, which leads to enhanced absorption in the absorber layer. These improvements slightly shift from the research objectives where SWNT/P3HT composite was expected to electrically improve the fill factor of PbS CQD photovoltaics. Indeed, the effect of optical enhancement took an active role to overall efficiency improvement compared to the influence of the electric improvement of the photovoltaic devices. With these electronic and optical enhancements, the efficiency of the PbS CQD solar cells improved from 4.0% to 6.0%.

In chapter 6, SWNT-P3HT composites were utilized in a bulk heterojunction structure with PbS EDT layer. The bulk heterojunction structure is an architectural approach to give a better charge transport while thickening the photoactive PbS CQD layer of the photovoltaic devices. Devices with a bulk heterojunction layer of SWNT-P3HT composite and PbS CQD with 1.2-Ethanedithiol (EDT) were compared with control devices which have planar heterojunction structure between PbS-EDT and SWNT-P3HT, and by varying the thickness of the PbS-EDT layer from 60 nm to 240 nm. Among all devices, the bulk heterojunction device with 120 nm PbS-EDT thickness recorded the highest power conversion efficiency of 11.5%. In general, bulk heterojunction devices exhibited better carrier transfer with less monomolecular carrier recombination. As a result, the devices with bulk heterojunction structure have demonstrated better fill factor values. By thickening the PbS-EDT layer from 60 nm to 240 nm, both bulk heterojunction devices and planar heterojunction devices had increases in absorption. However, bulk heterojunction devices showed increase of J_{sc} towards 240 nm thickness of PbS-EDT, while the planar heterojunction devices had a decrease in J_{sc} after a peak at 120 nm thickness of PbS-EDT. The difference in J_{sc} with the thicker PbS-EDT layer was examined by IQE analysis and electronic impedance spectroscopy measurement. Regarding the original aim of the chapter, SWNT/P3HT composite worked as they should. It improved the ability to transport charge while the PbS CQD layers were thickened. The bulk heterojunction structure gave more prominent differences to other planar-structured photovoltaics when the thickness of the PbS-EDT exceeded over 120 nm.

In chapter 7, the optimized method to transfer a graphene layer to PbS CQD thin films has been studied, and the device performance of the PbS CQD solar cells using graphene and control PbS CQD solar cells were compared. First, the effect of the annealing and an acetone bath treatment to both graphene stacking and the quality of PbS CQD thin film has been explored. Although the annealing effect did not seem

to have a significant impact on the adhesion of the graphene layer onto PbS CQD thin film, annealing had a detrimental impact on the performance of PbS CQD devices. To understand the mechanisms of detrimental effects of annealing and aceton bath treatments, FTIR and XPS measurements were carried out. Both measurements confirmed the removal of ligands coordinating to PbS nanocrystals and the oxidation of PbS nanocrystals which degrades the quality of PbS CQD thin films. The aim of annealing graphene devices is to make the graphene layer stick well to the PbS CQD thin film. However, Raman microscopic mapping revealed that the graphene layer without annealing is adhered as well as the layer with the annealing treatment, and has the same defect levels. In the latter part of the chapter, side-by-side comparisons of the graphene device and the control device have been made. The graphene devices performed better over control devices in absorption and J_{sc}. Moreover, intensity-dependent V_{oc} and quantum efficiency measurements confirmed that the graphene device has less monomolecular carrier recombination and better IQE which results in a better V_{oc} and FF. The results of electronic impedance spectroscopy further confirmed the better charge transfer with a graphene monolayer in PbS CQD PV devices. Thus the graphene layer has been proven to be a good electrode for further applications.

8.2 Future work

8.2.1 Application of other 1D materials in PMMA matrices

In chapter 5, a composite of SWNT and P3HT was employed in an insulating PMMA matrix to be a hole-transport layer in PbS CQD photovoltaic devices. This enhances the performance and long-term stability of PbS CQD solar cells. The use of 1D materials in a PMMA matrix can be applied to other 1D materials such as silver nanowires to give better device stability to PbS CQD solar cells.

8.2.2 Ordered patterning of SWNT in bulk heterojunction structure

In chapter 6, the bulk heterojunction layer of SWNT-P3HT composite and PbS CQD thin film was fabricated by spin-coating. Although the devices with bulk heterojunction structure exhibited the superior performance over the devices with the planar heterojunction structure, an ordered structure in the bulk heterojunction layer would improve their performance even more by reducing the carrier recombination even more. The application of a high electric field (AC signal with 10V of peak-to-peak voltage)[199] or magnetic field (5-12 Tesla)[200] is known to align carbon nanotubes. However, such a high electric field would degrade the photovoltaic devices. Thus, the application of high magnetic field could be the path to realize the micropatterning of SWNT in bulk heterojunction structure.

8.2.3 Monolithic tandem (multi-junction) solar cell with graphene as an interlayer

In chapter 7, the method to transfer graphene on PbS CQD thin film has been explored. The results suggested that the monolayer of graphene can stick well on PbS CQD thin films without annealing. With this discovery, the development of monolithic tandem solar cells with monolayer graphene as an interlayer could be a tremendous step in utilizing graphene for PbS CQD solar cells. As graphene has such high transparency and conductivity, it is very sufficient to be an interlayer in the monolithic tandem solar cells.[201,202]

Bibliography

[1] Wadia, C.; Alivisatos, A. P.; Kammen, D. M. Materials Availability Expands the Opportunity for Large-Scale Photovoltaics Deployment. 2009.

[2] Nelson, J. *The physics of solar cells*; World Scientific, 2003; Vol. 57.

[3] Sze, S. M.; Ng, K. K. *Physics of semiconductor devices*; John Wiley & Sons, 2006.

[4] Tang, J.; Sargent, E. H. Infrared colloidal quantum dots for photovoltaics: fundamentals and recent progress. *Advanced Materials* **2011**, *23*, 12–29.

[5] Pagliaro, M.; Ciriminna, R.; Palmisano, G. Flexible solar cells. *ChemSusChem* **2008**, *1*, 880–91.

[6] Part II Photovoltaic Cell I-V Characterization Theory and LabVIEW Analysis Code - National Instruments. http://www.ni.com/white-paper/7230/en/.

[7] Schöll, E. *Theory of Transport Properties of Semiconductor*; Springer: London, 1998; p 7.

[8] Park, J.; Joo, J.; Kwon, S. G.; Jang, Y.; Hyeon, T. Synthesis of monodisperse spherical nanocrystals. *Angewandte Chemie (International ed. in English)* **2007**, *46*, 4630–60.

[9] Carey, G. H.; Levina, L.; Comin, R.; Voznyy, O.; Sargent, E. H. Record Charge Carrier Diffusion Length in Colloidal Quantum Dot Solids via Mutual Dot-To-Dot Surface Passivation. *Advanced Materials* **2015**, *27*, 3325–30.

[10] Milliron, D. J. Quantum dot solar cells: The surface plays a core role. *Nature Materials* **2014**, *13*, 772–773.

[11] Brown, P. R.; Kim, D.; Lunt, R. R.; Zhao, N.; Bawendi, M. G.; Grossman, J. C.; Bulović, V. Energy Level Modification in Lead Sulfide Quantum Dot Thin Films through Ligand Exchange. *ACS Nano* **2014**, *8*, 5863–5872.

[12] Choi, H.; Ko, J.-H.; Kim, Y.-H.; Jeong, S. Steric-Hindrance-Driven Shape Transition in PbS Quantum Dots: Understanding Size-Dependent Stability. *Journal of the American Chemical Society* **2013**, *135*, 5278–5281.

[13] Choi, H.; Kwan Kim, J.; Hoon Song, J.; Kim, Y.; Jeong, S. Increased open-circuit voltage in a Schottky device using PbS quantum dots with extreme confinement. *Applied Physics Letters* **2013**, *102*, 193902.

[14] Yoon, W.; Boercker, J. E.; Lumb, M. P.; Placencia, D.; Foos, E. E.; Tischler, J. G. Enhanced Open-Circuit Voltage of PbS Nanocrystal Quantum Dot Solar Cells. *Scientific Reports* **2013**, *3*, 2225.

[15] Ip, A. H. et al. Hybrid Passivated Colloidal Quantum Dot Solids. *Nature Nanotechnology* **2012**, *7*, 577–582.

[16] Thon, S. M.; Ip, A. H.; Voznyy, O.; Levina, L.; Kemp, K. W.; Carey, G. H.; Masala, S.; Sargent, E. H. Role of Bond Adaptability in the Passivation of Colloidal Quantum Dot Solids. *ACS Nano* **2013**, *7*, 7680–7688.

[17] Zhang, J.; Gao, J.; Church, C. P.; Miller, E. M.; Luther, J. M.; Klimov, V. I.; Beard, M. C. PbSe Quantum Dot Solar Cells with More than 6% Efficiency Fabricated in Ambient Atmosphere. *Nano Letters* **2014**, *14*, 6010–6015.

[18] Ning, Z.; Dong, H.; Zhang, Q.; Voznyy, O.; Sargent, E. H. Solar Cells Based on Inks of n-Type Colloidal Quantum Dots. *ACS Nano* **2014**, *8*, 10321–10327.

[19] Liu, Y.; Gibbs, M.; Puthussery, J.; Gaik, S.; Ihly, R.; Hillhouse, H. W.; Law, M. Dependence of carrier mobility on nanocrystal size and ligand length in PbSe nanocrystal solids. *Nano letters* **2010**, *10*, 1960–9.

[20] Jean, J.; Chang, S.; Brown, P. R.; Cheng, J. J.; Rekemeyer, P. H.; Bawendi, M. G.; Gradečak, S.; Bulović, V. ZnO nanowire arrays for enhanced photocurrent in PbS quantum dot solar cells. *Advanced Materials* **2013**, *25*, 2790–6.

[21] Choi, J. J.; Wenger, W. N.; Hoffman, R. S.; Lim, Y.-F.; Luria, J.; Jasieniak, J.; Marohn, J. A.; Hanrath, T. Solution-Processed Nanocrystal Quantum Dot Tandem Solar Cells. *Advanced Materials* **2011**, *23*, 3144–3148.

[22] Wang, X.; Koleilat, G. I.; Tang, J.; Liu, H.; Kramer, I. J.; Debnath, R.; Brzozowski, L.; Barkhouse, D. A. R.; Levina, L.; Hoogland, S.; Sargent, E. H. Tandem colloidal quantum dot solar cells employing a graded recombination layer. *Nature Photonics* **2011**, *5*, 480–484.

[23] Chuang, C.-H. M.; Brown, P. R.; Bulović, V.; Bawendi, M. G. Improved performance and stability in quantum dot solar cells through band alignment engineering. *Nature Materials* **2014**, *13*, 796–801.

[24] Jun, S. In *Graphene-Based Energy Devices*; Yusoff, R. b. M., Ed.; Wiley: Weinheim, 2015; pp 1–48.

[25] Administration, U. S. E. I. *International Energy Outlook 2013*; 2013; Vol. DOE/EIA-04; p 1.

[26] Perez, R.; Perez, M. A fundamental look at energy reserves for the planet. *The IEA SHC Solar Update* **2009**, *50*, 2–3.

[27] United Nations DESA/Population, *World Populaiton Prospects 2017*; 2017.

[28] The World Bank, *GDP per capita 2017*; 2017.

[29] Survey, U. S. G. *Mineral Commodity Summaries: 2012*; Government Printing Office: Washington, D.C., 2012.

[30] Choy, K. L. Chemical vapour deposition of coatings. *Progress in materials science* **2003**, *48*, 63–64.

[31] Kramer, I. J.; Minor, J. C.; Moreno-Bautista, G.; Rollny, L.; Kanjanaboos, P.; Kopilovic, D.; Thon, S. M.; Carey, G. H.; Chou, K. W.; Zhitomirsky, D.; Amassian, A.; Sargent, E. H. Efficient spray-coated colloidal quantum dot solar cells. *Advanced Materials* **2015**, *27*, 116–121.

[32] Luther, J. M.; Law, M.; Beard, M. C.; Song, Q.; Reese, M. O.; Ellingson, R. J.; Nozik, A. J. Schottky Solar Cells Based on Colloidal Nanocrystal Films. *Nano Letters* **2008**, *8*, 3488–3492.

[33] Alivisatos, A. P. Semiconductor Clusters, Nanocrystals, and Quantum Dots. *Science* **1996**, *271*, 933–937.

[34] Tang, J.; Kemp, K. W.; Hoogland, S.; Jeong, K. S.; Liu, H.; Levina, L.; Furukawa, M.; Wang, X.; Debnath, R.; Cha, D.; Chou, K. W.; Fischer, A.; Amassian, A.; Asbury, J. B.; Sargent, E. H. Colloidal-quantum-dot Photovoltaics using Atomic-ligand Passivation. *Nature materials* **2011**, *10*, 765–71.

[35] Wang, Y.; Suna, A.; Mahler, W.; Kasowski, R. PbS in polymers. From molecules to bulk solids. *The Journal of chemical physics* **1987**, *87*, 7315–7322.

[36] Ekimov, A. I.; Efros, A. L.; Onushchenko, A. A. Quantum size effect in semiconductor microcrystals. *Solid State Communications* **1985**, *56*, 921–924.

[37] Yoffe, A. D. Low-dimensional systems: quantum size effects and electronic properties of semiconductor microcrystallites (zero-dimensional systems) and some quasi-two-dimensional systems. *Advances in Physics* **1993**, *42*, 173–262.

[38] Brus, L. Electronic wave functions in semiconductor clusters: experiment and theory. *The Journal of Physical Chemistry* **1986**, *90*, 2555–2560.

[39] Yu, W. W.; Qu, L.; Guo, W.; Peng, X. Experimental Determination of the Extinction Coefficient of CdTe, CdSe, and CdS Nanocrystals. *Chemistry of Materials* **2003**, *15*, 2854–2860.

[40] Moreels, I.; Lambert, K.; Smeets, D.; De Muynck, D.; Nollet, T.; Martins, J. C.; Vanhaecke, F.; Vantomme, A.; Delerue, C.; Allan, G.; Hens, Z. Size-dependent optical properties of colloidal PbS quantum dots. *ACS nano* **2009**, *3*, 3023–30.

[41] Murphy, J. E. PbTe Colloidal Nanocrystals: Synthesis, Characterization, and Multiple Exciton Generation. *J. Am. Chem. Soc.* **2006**, *128*, 3241–3247.

[42] Nozik, A. J. Multiple exciton generation in semiconductor quantum dots. *Chemical Physics Letters* **2008**, *457*, 3–11.

[43] Hillhouse, H. W.; Beard, M. C. Solar cells from colloidal nanocrystals: Fundamentals, materials, devices, and economics. *Current Opinion in Colloid & Interface Science* **2009**, *14*, 245–259.

[44] Nozik, A. Quantum dot solar cells. *Physica E: Low-dimensional Systems and Nanostructures* **2002**, *14*, 115–120.

[45] Nozik, A. J. Spectroscopy and Hot Electron Relaxation Dynamics in Semiconductor Quantum Wells and Quantum Dots. **2003**,

[46] Shabaev, A.; Efros, A. L.; Nozik, A. J. Multiexciton Generation by a Single Photon in Nanocrystals. *Nano Letters* **2006**, *6*, 2856–2863.

[47] Luther, J. M.; Law, M.; Song, Q.; Perkins, C. L.; Beard, M. C.; Nozik, A. J. Structural, Optical, and Electrical Properties of Self-assembled Films of PbSe Nanocrystals Treated with 1,2-ethanedithiol. *ACS nano* **2008**, *2*, 271–80.

[48] Luther, J. M.; Gao, J.; Lloyd, M. T.; Semonin, O. E.; Beard, M. C.; Nozik, A. J. Stability assessment on a 3% bilayer PbS/ZnO quantum dot heterojunction solar cell. *Advanced Materials* **2010**, *22*, 3704–7.

[49] Wood, V.; Panzer, M. J.; Chen, J.; Bradley, M. S.; Halpert, J. E.; Bawendi, M. G.; Bulović, V. Inkjet-Printed Quantum Dot-Polymer Composites for Full-Color AC-Driven Displays. *Advanced Materials* **2009**, *21*, 2151–2155.

[50] Haverinen, H. M.; Myllyla, R. A.; Jabbour, G. E. Inkjet printing of light emitting quantum dots. *Applied Physics Letters* **2009**, *94*, 073108.

[51] Singh, M.; Haverinen, H. M.; Dhagat, P.; Jabbour, G. E. Inkjet printing-process and its applications. *Advanced Materials* **2010**, *22*, 673–85.

[52] Murray, C. B.; Norris, D. J.; Bawendi, M. G. Synthesis and characterization of nearly monodisperse CdE (E = sulfur, selenium, tellurium) semiconductor nanocrystallites. *Journal of the American Chemical Society* **1993**, *115*, 8706–8715.

[53] Kumar, S.; Nann, T. Shape Control of IIVI Semiconductor Nanomaterials. *Small* **2006**, *2*, 316–329.

[54] Thanh, N. T. K.; Maclean, N.; Mahiddine, S. Mechanisms of nucleation and growth of nanoparticles in solution. *Chemical reviews* **2014**, *114*, 7610–30.

[55] Kwon, S. G.; Piao, Y.; Park, J.; Angappane, S.; Jo, Y.; Hwang, N.-M.; Park, J.-G.; Hyeon, T. Kinetics of monodisperse iron oxide nanocrystal formation by "heating-up" process. *Journal of the American Chemical Society* **2007**, *129*, 12571–84.

[56] Hines, M. A.; Scholes, G. D. Colloidal PbS nanocrystals with Size-Tunable Near-Infrared Emission: Observation of Post-Synthesis Self-Narrowing of the Particle Size Distribution. *Advanced Materials* **2003**, *15*, 1844–1849.

[57] Reiss, H. The Growth of Uniform Colloidal Dispersions. *The Journal of Chemical Physics* **1951**, *19*, 482.

[58] De Smet, Y.; Deriemaeker, L.; Finsy, R. A Simple Computer Simulation of Ostwald Ripening. *Langmuir* **1997**, *13*, 6884–6888.

[59] Yin, Y.; Alivisatos, A. P. Colloidal nanocrystal synthesis and the organic-inorganic interface. *Nature* **2005**, *437*, 664–70.

[60] van Embden, J.; Mulvaney, P. Nucleation and growth of CdSe nanocrystals in a binary ligand system. *Langmuir : the ACS journal of surfaces and colloids* **2005**, *21*, 10226–33.

[61] Remacle, F. On Electronic Properties of Assemblies of Quantum Nanodots. *The Journal of Physical Chemistry A* **2000**, *104*, 4739–4747.

[62] Zhang, J.; Gao, J.; Miller, E. M.; Luther, J. M.; Beard, M. C. Diffusion-controlled Synthesis of PbS and PbSe Quantum Dots with in situ Halide Passivation for Quantum Dot Solar Cells. *ACS Nano* **2014**, *8*, 614–622.

[63] Ip, A. H. et al. Hybrid Passivated Colloidal Quantum Dot Solids. *Nature Nanotechnology* **2012**, *7*, 577–582.

[64] Ning, Z.; Ren, Y.; Hoogland, S.; Voznyy, O.; Levina, L.; Stadler, P.; Lan, X.; Zhitomirsky, D.; Sargent, E. H. All-inorganic colloidal quantum dot photovoltaics employing solution-phase halide passivation. *Advanced Materials* **2012**, *24*, 6295–9.

[65] Ning, Z. et al. Air-stable n-type colloidal quantum dot solids. *Nature materials* **2014**, *13*, 822–8.

[66] Zhitomirsky, D.; Voznyy, O.; Hoogland, S.; Sargent, E. H. Measuring charge carrier diffusion in coupled colloidal quantum dot solids. *ACS nano* **2013**, *7*, 5282–90.

[67] Nagpal, P.; Klimov, V. I. Role of mid-gap states in charge transport and photoconductivity in semiconductor nanocrystal films. *Nature communications* **2011**, *2*, 486.

[68] Gao, J.; Johnson, J. C. Charge trapping in bright and dark states of coupled PbS quantum dot films. *ACS nano* **2012**, *6*, 3292–303.

[69] Bozyigit, D.; Volk, S.; Yarema, O.; Wood, V. Quantification of Deep Traps in Nanocrystal Solids, Their Electronic Properties, and Their Influence on Device Behavior. *Nano Letters* **2013**, *13*, 5284–5288.

[70] Koleilat, G. I.; Levina, L.; Shukla, H.; Myrskog, S. H.; Hinds, S.; Pattantyus-Abraham, A. G.; Sargent, E. H. Efficient, stable infrared photovoltaics based on solution-cast colloidal quantum dots. *ACS nano* **2008**, *2*, 833–840.

[71] Konstantatos, G.; Levina, L.; Fischer, A.; Sargent, E. H. Engineering the temporal response of photoconductive photodetectors via selective introduction of surface trap states. *Nano letters* **2008**, *8*, 1446–50.

[72] Jeong, K. S.; Tang, J.; Liu, H.; Kim, J.; Schaefer, A. W.; Kemp, K.; Levina, L.; Wang, X.; Hoogland, S.; Debnath, R.; Brzozowski, L.; Sargent, E. H.; Asbury, J. B. Enhanced Mobility-Lifetime Products in PbS Colloidal Quantum Dot Photovoltaics. *ACS Nano* **2012**, *6*, 89–99.

[73] Kovalenko, M. V.; Scheele, M.; Talapin, D. V. Colloidal nanocrystals with molecular metal chalcogenide surface ligands. *Science* **2009**, *324*, 1417–20.

[74] Talgorn, E.; Moysidou, E.; Abellon, R. D.; Savenije, T. J.; Goossens, A.; Houtepen, A. J.; Siebbeles, L. D. A. Highly Photoconductive CdSe Quantum-Dot Films: Influence of Capping Molecules and Film Preparation Procedure. *The Journal of Physical Chemistry C* **2010**, *114*, 3441–3447.

[75] Zhitomirsky, D.; Furukawa, M.; Tang, J.; Stadler, P.; Hoogland, S.; Voznyy, O.; Liu, H.; Sargent, E. H. N-type colloidal-quantum-dot solids for photovoltaics. *Advanced Materials* **2012**, *24*, 6181–5.

[76] Santra, P. K.; Palmstrom, A. F.; Tanskanen, J. T.; Yang, N.; Bent, S. F. Improving Performance in Colloidal Quantum Dot Solar Cells by Tuning Band Alignment through Surface Dipole Moments. *The Journal of Physical Chemistry C* **2015**, *119*, 2996–3005.

[77] Katsiev, K. et al. The complete in-gap electronic structure of colloidal quantum dot solids and its correlation with electronic transport and photovoltaic performance. *Advanced Materials* **2014**, *26*, 937–42.

[78] Pan, J.; El-Ballouli, A. O.; Rollny, L.; Voznyy, O.; Burlakov, V. M.; Goriely, A.; Sargent, E. H.; Bakr, O. M. Automated Synthesis of Photovoltaic-Quality Colloidal Quantum Dots Using Separate Nucleation and Growth Stages. *ACS Nano* **2013**, *7*, 10158–10166.

[79] Cademartiri, L.; Ozin, G. A. Emerging Strategies for the Synthesis of Highly Monodisperse Colloidal Nanostructures. *Philosophical Transactions of the Royal Society A: Mathematical, Physical and Engineering Sciences* **2010**, *368*, 4229–4248.

[80] Yuan, M.; Kemp, K. W.; Thon, S. M.; Kim, J. Y.; Chou, K. W.; Amassian, A.; Sargent, E. H. High-Performance Quantum-Dot Solids via Elemental Sulfur Synthesis. *Advanced Materials* **2014**, *26*, 3513–3519.

[81] Moreels, I.; Justo, Y.; De Geyter, B.; Haustraete, K.; Martins, J. C.; Hens, Z. Size-Tunable, Bright, and Stable PbS Quantum Dots: A Surface Chemistry Study. *ACS Nano* **2011**, *5*, 2004–2012.

[82] Chuang, C.-H. M.; Maurano, A.; Brandt, R. E.; Hwang, G. W.; Jean, J.; Buonassisi, T.; Bulović, V.; Bawendi, M. G. Open-Circuit Voltage Deficit, Radiative Sub-Bandgap States, and Prospects in Quantum Dot Solar Cells. *Nano Letters* **2015**, *15*, 3286–3294.

[83] Kim, S.-P.; Chew, H. B.; Chason, E.; Shenoy, V. B.; Kim, K.-S. Nanoscale mechanisms of surface stress and morphology evolution in FCC metals under noble-gas ion bombardments. *Proceedings of the Royal Society A: Mathematical, Physical and Engineering Sciences* **2012**, *468*, 2550–2573.

[84] Tang, J.; Brzozowski, L.; Barkhouse, D. A. R.; Wang, X.; Debnath, R.; Wolowiec, R.; Palmiano, E.; Levina, L.; Pattantyus-Abraham, A. G.; Jamakosmanovic, D.; Sargent, E. H. Quantum dot photovoltaics in the extreme quantum confinement regime: the surface-chemical origins of exceptional air- and light-stability. *ACS nano* **2010**, *4*, 869–78.

[85] Konstantatos, G.; Sargent, E. H. PbS colloidal quantum dot photoconductive photodetectors: Transport, traps, and gain. *Applied Physics Letters* **2007**, *91*, 173505.

[86] Sykora, M.; Koposov, A. Y.; McGuire, J. A.; Schulze, R. K.; Tretiak, O.; Pietryga, J. M.; Klimov, V. I. Effect of Air Exposure on Surface Properties, Electronic Structure, and Carrier Relaxation in PbSe Nanocrystals. *ACS Nano* **2010**, *4*, 2021–2034.

[87] Foos, E. E. The Complex Interaction of Spectroscopic Shifts and Electronic Properties in Semiconductor Nanocrystal Films. *The Journal of Physical Chemistry Letters* **2013**, *4*, 625–632.

[88] Crisp, R. W.; Kroupa, D. M.; Marshall, A. R.; Miller, E. M.; Zhang, J.; Beard, M. C.; Luther, J. M. Metal Halide Solid-State Surface Treatment for High Efficiency PbS and PbSe QD Solar Cells. *Scientific Reports* **2015**, *5*, 9945.

[89] Marshall, A. R.; Young, M. R.; Nozik, A. J.; Beard, M. C.; Luther, J. M. Exploration of Metal Chloride Uptake for Improved Performance Characteristics of PbSe Quantum Dot Solar Cells. *The Journal of Physical Chemistry Letters* **2015**, *6*, 2892–2899.

[90] Labelle, A. J.; Thon, S. M.; Masala, S.; Adachi, M. M.; Dong, H.; Farahani, M.; Ip, A. H.; Fratalocchi, A.; Sargent, E. H. Colloidal Quantum Dot Solar Cells Exploiting Hierarchical Structuring. *Nano Letters* **2015**, *15*, 1101–1108.

[91] Johnston, K. W.; Pattantyus-Abraham, A. G.; Clifford, J. P.; Myrskog, S. H.; MacNeil, D. D.; Levina, L.; Sargent, E. H. Schottky-quantum dot photovoltaics for efficient infrared power conversion. *Applied Physics Letters* **2008**, *92*, 151115.

[92] Fischer, A.; Rollny, L.; Pan, J.; Carey, G. H.; Thon, S. M.; Hoogland, S.; Voznyy, O.; Zhitomirsky, D.; Kim, J. Y.; Bakr, O. M.; Sargent, E. H. Directly Deposited Quantum Dot Solids Using a Colloidally Stable Nanoparticle Ink. *Advanced Materials* **2013**, *25*, 5742–5749.

[93] Talapin, D. V.; Murray, C. B. PbSe Nanocrystal Solids for n- and p-Channel Thin Film Field-Effect Transistors. *Science* **2005**, *310*, 86–89.

[94] Kovalenko, M. V.; Bodnarchuk, M. I.; Zaumseil, J.; Lee, J.-S.; Talapin, D. V. Expanding the Chemical Versatility of Colloidal Nanocrystals Capped with Molecu-

lar Metal Chalcogenide Ligands. *Journal of the American Chemical Society* **2010**, *132*, 10085–10092.

[95] Lee, J.-S.; Kovalenko, M. V.; Huang, J.; Chung, D. S.; Talapin, D. V. Band-like transport, high electron mobility and high photoconductivity in all-inorganic nanocrystal arrays. *Nature Nanotechnology* **2011**, *6*, 348–352.

[96] Yang, Z.; Janmohamed, A.; Lan, X.; García de Arquer, F. P.; Voznyy, O.; Yassitepe, E.; Kim, G.-H.; Ning, Z.; Gong, X.; Comin, R.; Sargent, E. H. Colloidal Quantum Dot Photovoltaics Enhanced by Perovskite Shelling. *Nano Letters* **2015**, *15*, 7539–7543.

[97] Liu, H.; Zhitomirsky, D.; Hoogland, S.; Tang, J.; Kramer, I. J.; Ning, Z.; Sargent, E. H. Systematic optimization of quantum junction colloidal quantum dot solar cells. *Applied Physics Letters* **2012**, *101*, 151112.

[98] Anderson, N. C.; Hendricks, M. P.; Choi, J. J.; Owen, J. S. Ligand Exchange and the Stoichiometry of Metal Chalcogenide Nanocrystals: Spectroscopic Observation of Facile Metal-Carboxylate Displacement and Binding. *Journal of the American Chemical Society* **2013**, *135*, 18536–18548.

[99] Oh, S. J.; Berry, N. E.; Choi, J.-H.; Gaulding, E. A.; Paik, T.; Hong, S.-H.; Murray, C. B.; Kagan, C. R. Stoichiometric Control of Lead Chalcogenide Nanocrystal Solids to Enhance Their Electronic and Optoelectronic Device Performance. *ACS Nano* **2013**, *7*, 2413–2421.

[100] Luther, J. M.; Pietryga, J. M. Stoichiometry control in quantum dots: a viable analog to impurity doping of bulk materials. *ACS nano* **2013**, *7*, 1845–9.

[101] Ning, Z.; Zhitomirsky, D.; Adinolfi, V.; Sutherland, B.; Xu, J.; Voznyy, O.; Maraghechi, P.; Lan, X.; Hoogland, S.; Ren, Y.; Sargent, E. H. Graded doping

for enhanced colloidal quantum dot photovoltaics. *Advanced Materials* **2013**, *25*, 1719–23.

[102] Tang, J.; Liu, H.; Zhitomirsky, D.; Hoogland, S.; Wang, X.; Furukawa, M.; Levina, L.; Sargent, E. H. Quantum Junction Solar Cells. *Nano Letters* **2012**, *12*, 4889–4894.

[103] Voznyy, O.; Zhitomirsky, D.; Stadler, P.; Ning, Z.; Hoogland, S.; Sargent, E. H. A Charge-Orbital Balance Picture of Doping in Colloidal Quantum Dot Solids. *ACS Nano* **2012**, *6*, 8448–8455.

[104] Choi, J. J.; Lim, Y.-F.; Santiago-Berrios, M. B. M. B.; Oh, M.; Hyun, B.-R.; Sun, L.; Bartnik, A. C.; Goedhart, A.; Malliaras, G. G.; Abruna, H. D.; Wise, F. W.; Hanrath, T.; Abruña, H. D.; Wise, F. W.; Hanrath, T. PbSe nanocrystal excitonic solar cells. *Nano letters* **2009**, *9*, 3749–55.

[105] Leschkies, K. S.; Beatty, T. J.; Kang, M. S.; Norris, D. J.; Aydil, E. S. Solar cells based on junctions between colloidal PbSe nanocrystals and thin ZnO films. *ACS nano* **2009**, *3*, 3638–48.

[106] Pattantyus-Abraham, A. G.; Kramer, I. J.; Barkhouse, A. R.; Wang, X.; Konstantatos, G.; Debnath, R.; Levina, L.; Raabe, I.; Nazeeruddin, M. K.; Grätzel, M.; Sargent, E. H. Depleted-heterojunction colloidal quantum dot solar cells. *ACS nano* **2010**, *4*, 3374–80.

[107] Brown, P. R.; Lunt, R. R.; Zhao, N.; Osedach, T. P.; Wanger, D. D.; Chang, L.-Y.; Bawendi, M. G.; Bulović, V. Improved current extraction from ZnO/PbS quantum dot heterojunction photovoltaics using a MoO_3 interfacial layer. *Nano letters* **2011**, *11*, 2955–61.

[108] Shaheen, S. E.; Brabec, C. J.; Sariciftci, N. S.; Padinger, F.; Fromherz, T.; Hummelen, J. C. 2.5% efficient organic plastic solar cells. *Applied Physics Letters* **2001**, *78*, 841.

[109] Barkhouse, D. A. R.; Debnath, R.; Kramer, I. J.; Zhitomirsky, D.; Pattantyus-Abraham, A. G.; Levina, L.; Etgar, L.; Grätzel, M.; Sargent, E. H. Depleted bulk heterojunction colloidal quantum dot photovoltaics. *Advanced Materials* **2011**, *23*, 3134–8.

[110] Kramer, I. J.; Zhitomirsky, D.; Bass, J. D.; Rice, P. M.; Topuria, T.; Krupp, L.; Thon, S. M.; Ip, A. H.; Debnath, R.; Kim, H.-C.; Sargent, E. H. Ordered Nanopillar Structured Electrodes for Depleted Bulk Heterojunction Colloidal Quantum Dot Solar Cells. *Advanced Materials* **2012**, *24*, 2315–2319.

[111] Cheng, C.; Lee, M. M.; Noel, N. K.; Hughes, G. M.; Ball, J. M.; Assender, H. E.; Snaith, H. J.; Watt, A. A. R. Polystyrene templated porous titania wells for quantum dot heterojunction solar cells. *ACS applied materials & interfaces* **2014**, *6*, 14247–14252.

[112] King, R. R.; Law, D. C.; Edmondson, K. M.; Fetzer, C. M.; Kinsey, G. S.; Yoon, H.; Sherif, R. A.; Karam, N. H. 40% efficient metamorphic GaInPGaInAsGe multijunction solar cells. *Applied Physics Letters* **2007**, *90*, 183516.

[113] Yakimov, A.; Forrest, S. R. High photovoltage multiple-heterojunction organic solar cells incorporating interfacial metallic nanoclusters. *Applied Physics Letters* **2002**, *80*, 1667–1669.

[114] Hadipour, A.; de Boer, B.; Wildeman, J.; Kooistra, F. B.; Hummelen, J. C.; Turbiez, M. G. R.; Wienk, M. M.; Janssen, R. A. J.; Blom, P. W. M. Solution-

Processed Organic Tandem Solar Cells. *Advanced Functional Materials* **2006**, *16*, 1897–1903.

[115] Yuan, M.; Zhitomirsky, D.; Adinolfi, V.; Voznyy, O.; Kemp, K. W.; Ning, Z.; Lan, X.; Xu, J.; Kim, J. Y.; Dong, H.; Sargent, E. H. Doping control via molecularly engineered surface ligand coordination. *Advanced Materials* **2013**, *25*, 5586–92.

[116] Ko, D.-K.; Brown, P. R.; Bawendi, M. G.; Bulović, V. p-i-n Heterojunction solar cells with a colloidal quantum-dot absorber layer. *Advanced Materials* **2014**, *26*, 4845–50.

[117] Geim, A. K. Graphene: status and prospects. *Science (New York, N.Y.)* **2009**, *324*, 1530–4.

[118] Avouris, P. Graphene: Electronic and Photonic Properties and Devices. *Nano Letters* **2010**, *10*, 4285–4294.

[119] Rao, C. N. R.; Maitra, U.; Ramakrishna Matte, H. S. S. In *Graphene: Synthesis, Properties, and Phenomena*; Rao, C. N. R., Sood, A. K., Eds.; Wiley: Weinheim, 2013; pp 1–48.

[120] Banhart, F.; Kotakoski, J.; Krasheninnikov, A. V. Structural Defects in Graphene. *ACS Nano* **2011**, *5*, 26–41.

[121] Fuhrer, M. S.; Lau, C. N.; MacDonald, A. H. Graphene: Materially Better Carbon. *MRS Bulletin* **2010**, *35*, 289–295.

[122] Emani, N. K.; Kildishev, A. V.; Shalaev, V. M.; Boltasseva, A. Graphene: A Dynamic Platform for Electrical Control of Plasmonic Resonance. *Nanophotonics* **2015**, *4*.

[123] Blake, P.; Brimicombe, P. D.; Nair, R. R.; Booth, T. J.; Jiang, D.; Schedin, F.; Ponomarenko, L. A.; Morozov, S. V.; Gleeson, H. F.; Hill, E. W.; Geim, A. K.; Novoselov, K. S. Graphene-Based Liquid Crystal Device. *Nano Letters* **2008**, *8*, 1704–1708.

[124] Wang, X.; Zhi, L.; Tsao, N.; Tomović, Ž.; Li, J.; Müllen, K. Transparent Carbon Films as Electrodes in Organic Solar Cells. *Angewandte Chemie International Edition* **2008**, *47*, 2990–2992.

[125] Liu, Q.; Liu, Z.; Zhang, X.; Yang, L.; Zhang, N.; Pan, G.; Yin, S.; Chen, Y.; Wei, J. Polymer Photovoltaic Cells Based on Solution-Processable Graphene and P3HT. *Advanced Functional Materials* **2009**, *19*, 894–904.

[126] Zhang, J.; Zhang, C.; Sha, J.; Fei, H.; Li, Y.; Tour, J. M. Efficient Water-Splitting Electrodes Based on Laser-Induced Graphene. *ACS Applied Materials & Interfaces* **2017**, *9*, 26840–26847.

[127] Nair, R. R.; Blake, P.; Grigorenko, A. N.; Novoselov, K. S.; Booth, T. J.; Stauber, T.; Peres, N. M. R.; Geim, A. K. Electromechanical Resonators from Graphene Sheets. *Science* **2008**, *315*, 490–493.

[128] Wang, F.; Zhang, Y.; Tian, C.; Girit, C.; Zettl, A.; Crommie, M.; Shen, Y. R. Gate-variable optical transitions in graphene. *Science (New York, N.Y.)* **2008**, *320*, 206–9.

[129] Xia, F.; Mueller, T.; Lin, Y.-m.; Valdes-Garcia, A.; Avouris, P. Ultrafast graphene photodetector. *Nature Nanotechnology* **2009**, *4*, 839–843.

[130] Generalov, A. A.; Andersson, M. A.; Yang, X.; Vorobiev, A.; Stake, J. A 400-GHz Graphene FET Detector. *IEEE Transactions on Terahertz Science and Technology* **2017**, *7*, 614–616.

[131] Ishida, S.; Anno, Y.; Takeuchi, M.; Matsuoka, M.; Takei, K.; Arie, T.; Akita, S. Highly photosensitive graphene field-effect transistor with optical memory function. *Scientific Reports* **2015**, *5*, 15491.

[132] Dresselhaus, M.; Dresselhaus, G.; Eklund, P. *Science of Fullerenes and Carbon Nanotubes*; Elsevier, 1996; pp 756–869.

[133] Dekker, C. Carbon Nanotubes as Molecular Quantum Wires. *Physics Today* **1999**, *52*, 22.

[134] Iijima, S.; Ichihashi, T. Single-shell carbon nanotubes of 1-nm diameter. *Nature* **1993**, *363*, 603–605.

[135] Bethune, D. S.; Klang, C. H.; de Vries, M. S.; Gorman, G.; Savoy, R.; Vazquez, J.; Beyers, R. Cobalt-catalysed growth of carbon nanotubes with single-atomic-layer walls. *Nature* **1993**, *363*, 605–607.

[136] McEuen, P. L.; Park, J.-Y. Electron Transport in Single-Walled Carbon Nanotubes. *MRS Bulletin* **2004**, *29*, 272–275.

[137] Ruoff, R. S.; Qian, D.; Liu, W. K. Mechanical properties of carbon nanotubes: theoretical predictions and experimental measurements. *Comptes Rendus Physique* **2003**, *4*, 993–1008.

[138] Tans, S. J.; Verschueren, A. R. M.; Dekker, C. Room-temperature transistor based on a single carbon nanotube. **1998**, *393*, 49–52.

[139] Dürkop, T.; Getty, S. A.; Cobas, E.; Fuhrer, M. S. Extraordinary Mobility in Semiconducting Carbon Nanotubes. *Nano Letters* **2004**, *4*, 35–39.

[140] Javey, A.; Guo, J.; Wang, Q.; Lundstrom, M.; Dai, H. Ballistic Carbon Nanotube Field-effect Transistors. *Nature* **2003**, *424*, 654–7.

[141] Pennington, G.; Goldsman, N. Low-field semiclassical carrier transport in semiconducting carbon nanotubes. *Physical Review B* **2005**, *71*, 205318.

[142] Anantram, M. P.; Léonard, F. Physics of carbon nanotube electronic devices. *Reports on Progress in Physics* **2006**, *69*, 507–561.

[143] Kymakis, E.; Amaratunga, G. A. J. Single-wall carbon nanotube/conjugated polymer photovoltaic devices. *Applied Physics Letters* **2002**, *80*, 112–114.

[144] Landi, B. J.; Raffaelle, R. P.; Castro, S. L.; Bailey, S. G. Single-wall carbon nanotube-polymer solar cells. *Progress in Photovoltaics: Research and Applications* **2005**, *13*, 165–172.

[145] Habisreutinger, S. N.; Leijtens, T.; Eperon, G. E.; Stranks, S. D.; Nicholas, R. J.; Snaith, H. J. Carbon nanotube/polymer composite as a highly stable charge collection layer in perovskite solar cells. *Nano letters* **2014**, *14*, 5561–5568.

[146] Habisreutinger, S. N.; Leijtens, T.; Eperon, G. E.; Stranks, S. D.; Nicholas, R. J.; Snaith, H. J. Carbon Nanotube/polymer Composites as a Highly Stable Hole Collection Layer in Perovskite Solar Cells. *Nano Letters* **2014**, *14*, 5561–5568.

[147] Habisreutinger, S. N.; Leijtens, T.; Eperon, G. E.; Stranks, S. D.; Nicholas, R. J.; Snaith, H. J. Enhanced Hole Extraction in Perovskite Solar Cells Through Carbon Nanotubes. *The Journal of Physical Chemistry Letters* **2014**, *5*, 4207–4212.

[148] Martel, R.; Schmidt, T.; Shea, H. R.; Hertel, T.; Avouris, P. Single- and multi-wall carbon nanotube field-effect transistors. *Applied Physics Letters* **1998**, *73*, 2447.

[149] Womelsdorf, H.-J.; Hoheisel, W.; Passing, G. Nanoparticulate, redispersible zinc oxide gels. 2000; https://patents.google.com/patent/US6710091B1/en.

[150] Schuettfort, T.; Snaith, H. J.; Nish, A.; Nicholas, R. J. Synthesis and spectroscopic characterization of solution processable highly ordered polythiophenecarbon nanotube nanohybrid structures. *Nanotechnology* **2010**, *21*, 025201.

[151] Willis, S. M.; Cheng, C.; Assender, H. E.; Watt, A. A. R. The Transitional Heterojunction Behavior of PbS/ZnO Colloidal Quantum Dot Solar Cells. *Nano Letters* **2012**, *12*, 1522–1526.

[152] Bi, D.; Yang, L.; Boschloo, G.; Hagfeldt, A.; Johansson, E. M. J. Effect of Different Hole Transport Materials on Recombination in $CH_3NH_3PbI_3$ Perovskite-Sensitized Mesoscopic Solar Cells. *Journal of Physical Chemistry Letters* **2013**, *4*, 1532–1536.

[153] Snaith, H. J. Perovskites: The Emergence of a New Era for Low-Cost, High-Efficiency Solar Cells. *The Journal of Physical Chemistry Letters* **2013**, *4*, 3623–3630.

[154] Lattante, S. Electron and Hole Transport Layers: Their Use in Inverted Bulk Heterojunction Polymer Solar Cells. *Electronics* **2014**, *3*, 132–164.

[155] National Renewable Energy Laboratory Research Cell Efficiency Records. http://www.nrel.gov/ncpv/images/efficiency_chart.jpg.

[156] Ehrler, B.; Musselman, K. P.; Böhm, M. L.; Morgenstern, F. S. F.; Vaynzof, Y.; Walker, B. J.; MacManus-Driscoll, J. L.; Greenham, N. C. Preventing Interfacial Recombination in Colloidal Quantum Dot Solar Cells by Doping the Metal Oxide. *ACS Nano* **2013**, *7*, 4210–4220.

[157] Roy, A.; Park, S. H.; Cowan, S.; Tong, M. H.; Cho, S.; Lee, K.; Heeger, A. J. Titanium suboxide as an optical spacer in polymer solar cells. *Applied Physics Letters* **2009**, *95*, 013302.

[158] Kim, J.; Kim, S.; Lee, H.-H.; Lee, K.; Ma, W.; Gong, X.; Heeger, A. New Architecture for High-Efficiency Polymer Photovoltaic Cells Using Solution-Based Titanium Oxide as an Optical Spacer. *Advanced Materials* **2006**, *18*, 572–576.

[159] Kim, H. T.; Kim, C.-D.; Pyo, M. S.; Park, C. Electrical and optical characteristics of Ar plasma generated by low-frequency (60Hz) power source. *Korean Journal of Chemical Engineering* **2014**, *31*, 1892–1897.

[160] Ajayan, P. M. Nanotubes from Carbon. *Chemical Reviews* **1999**, *99*, 1787–1800.

[161] Odom, T. W.; Huang, J.-L. L.; Kim, P.; Lieber, C. M. Atomic Structure and Electronic Properties of Single-walled Carbon Nanotubes. *Nature* **1998**, *391*, 62–64.

[162] Wilder, J. W. G.; Venema, L. C.; Rinzler, A. G.; Smalley, R. E.; Dekker, C. Electronic Structure of Atomically Resolved Carbon Nanotubes. *Nature* **1998**, *391*, 59–62.

[163] Dabera, G. D. M. R.; Jayawardena, K. D. G. I.; Prabhath, M. R. R.; Yahya, I.; Tan, Y. Y.; Nismy, N. A.; Shiozawa, H.; Sauer, M.; Ruiz-Soria, G.; Ayala, P.; Stolojan, V.; Adikaari, A. A. D. T.; Jarowski, P. D.; Pichler, T.; Silva, S. R. P. Hybrid Carbon Nanotube Networks as Efficient Hole Extraction Layers for Organic Photovoltaics. *ACS Nano* **2013**, *7*, 556–565.

[164] Habisreutinger, S. N.; Wenger, B.; Snaith, H. J.; Nicholas, R. J. Dopant-free Planar nip Perovskite Solar Cells with Steady-State Efficiencies Exceeding 18%. *ACS Energy Letters* **2017**, *2*, 622–628.

[165] Pacholski, C.; Kornowski, A.; Weller, H. Self-assembly of ZnO: From Nanodots to Nanorods. *Angewandte Chemie - International Edition* **2002**, *41*, 1188–1191.

[166] Silverstein, R. M.; Webster, F. X.; Kiemle, D. J. *Spectrometric Identification of Organic Compounds.*; Wiley, 2012.

[167] Ning, Z.; Dong, H.; Zhang, Q.; Voznyy, O.; Sargent, E. H. Solar Cells Based on Inks of n Type Colloidal Quantum Dots. **2014**,

[168] Ke, W.; Fang, G.; Wan, J.; Tao, H.; Liu, Q.; Xiong, L.; Qin, P.; Wang, J.; Lei, H.; Yang, G.; Qin, M.; Zhao, X.; Yan, Y. Efficient Hole-Blocking Layer-Free Planar Halide Perovskite Thin-Film Solar Cells. *Nature Communications* **2015**, *6*, 6700.

[169] Zhang, W. et al. Ultrasmooth OrganicInorganic Perovskite Thin-Film Formation and Crystallization for Efficient Planar Heterojunction Solar Cells. *Nature Communications* **2015**, *6*, 6142.

[170] Ono, L. K.; Raga, S. R.; Wang, S.; Kato, Y.; Qi, Y. Temperature-Dependent Hysteresis Effects in Perovskite-Based Solar Cells. *J. Mater. Chem. A* **2015**, *3*, 9074–9080.

[171] Haruyama, J.; Sodeyama, K.; Han, L.; Tateyama, Y. First-Principles Study of Ion Diffusion in Perovskite Solar Cell Sensitizers. *Journal of the American Chemical Society* **2015**, *137*, 10048–10051.

[172] Sanchez, R. S.; Gonzalez-Pedro, V.; Lee, J.-W.; Park, N.-G.; Kang, Y. S.; Mora-Sero, I.; Bisquert, J. Slow Dynamic Processes in Lead Halide Perovskite Solar Cells. Characteristic Times and Hysteresis. *The Journal of Physical Chemistry Letters* **2014**, *5*, 2357–2363.

[173] Würfel, P.; Würfel, U. *Physics of Solar Cells: From Basic Principles to Advanced Concepts*, 3rd ed.; John Wiley & Sons: Weinheim, 2016; Chapter 6, p 168.

[174] Neo, D. C. J.; Zhang, N.; Tazawa, Y.; Jiang, H.; Hughes, G. M.; Grovenor, C. R. M.; Assender, H. E.; Watt, A. A. R. Poly(3-hexylthiophene-2,5-diyl) as a Hole Transport Layer for Colloidal Quantum Dot Solar Cells. *ACS Applied Materials & Interfaces* **2016**, *8*, 12101–12108.

[175] Williams, K. J.; Tisdale, W. A.; Leschkies, K. S.; Haugstad, G.; Norris, D. J.; Aydil, E. S.; Zhu, X. Y. Strong electronic coupling in two-dimensional assemblies of colloidal PbSe quantum dots. *ACS Nano* **2009**, *3*, 1532–1538.

[176] Sah, C. T.; Noyce, R. N.; Shockley, W. Carrier Generation and Recombination in p-n Junctions and p-n Junction Characteristics. *Proceedings of the IRE* **1957**, *45*, 1228–1243.

[177] Mauer, R.; Howard, I. A.; Laquai, F. Effect of Nongeminate Recombination on Fill Factor in Polythiophene/Methanofullerene Organic Solar Cells. *J. Phys. Chem. Lett.* **2010**, *1*, 3500–3505.

[178] Jha, A. R. *Solar Cell Technology and Applications*; CRC Press: New York, 2009; p 94.

[179] Kyaw, A. K. K.; Wang, D. H.; Gupta, V.; Leong, W. L.; Ke, L.; Bazan, G. C.; Heeger, A. J. Intensity Dependence of CurrentVoltage Characteristics and Recombination in High-Efficiency Solution-Processed Small-Molecule Solar Cells. *ACS Nano* **2013**, *7*, 4569–4577.

[180] Wetzelaer, G. A. H.; Kuik, M.; Lenes, M.; Blom, P. W. M. Origin of the dark-current ideality factor in polymer:fullerene bulk heterojunction solar cells. *Applied Physics Letters* **2011**, *99*, 153506.

[181] Mandoc, M.; Veurman, W.; Koster, L.; deBoer, B.; Blom, P. Origin of the Reduced Fill Factor and Photocurrent in MDMO-PPV:PCNEPV All-Polymer Solar Cells. *Advanced Functional Materials* **2007**, *17*, 2167–2173.

[182] Padilha, L. A.; Stewart, J. T.; Sandberg, R. L.; Bae, W. K.; Koh, W.-K.; Pietryga, J. M.; Klimov, V. I. Carrier Multiplication in Semiconductor Nanocrystals: Influence of Size, Shape, and Composition. *Accounts of Chemical Research* **2013**, *46*, 1261–1269.

[183] Stewart, J. T.; Padilha, L. A.; Qazilbash, M. M.; Pietryga, J. M.; Midgett, A. G.; Luther, J. M.; Beard, M. C.; Nozik, A. J.; Klimov, V. I. Comparison of Carrier Multiplication Yields in PbS and PbSe Nanocrystals: The Role of Competing Energy-Loss Processes. *Nano Letters* **2012**, *12*, 622–628.

[184] Liu, W. C.; Liu, Y.; Jennings, J. R.; Huang, H.; Wang, Q. Low-cost and flexible poly(3,4-ethylenedioxythiophene) based counter electrodes for efficient energy conversion in dye-sensitized solar cells. *Journal of Materials Chemistry A* **2014**, *2*, 10938.

[185] Pockett, A.; Eperon, G. E.; Peltola, T.; Snaith, H. J.; Walker, A.; Peter, L. M.; Cameron, P. J. Characterization of Planar Lead Halide Perovskite Solar Cells by Impedance Spectroscopy, Open-Circuit Photovoltage Decay, and Intensity-Modulated Photovoltage/Photocurrent Spectroscopy. *The Journal of Physical Chemistry C* **2015**, *119*, 3456–3465.

[186] Gellert, M.; Gries, K. I.; Sann, J.; Pfeifer, E.; Volz, K.; Roling, B. Impedance spectroscopic study of the charge transfer resistance at the interface between a $LiNi_{0.5}Mn_{1.5}O_4$ high-voltage cathode film and a $LiNbO_3$ coating film. *Solid State Ionics* **2016**, *287*, 8–12.

[187] Kyaw, A. K. K.; Wang, D. H.; Wynands, D.; Zhang, J.; Nguyen, T.-Q.; Bazan, G. C.; Heeger, A. J. Improved Light Harvesting and Improved Efficiency by Insertion of an Optical Spacer (ZnO) in Solution-Processed Small-Molecule Solar Cells. *Nano Letters* **2013**, *13*, 3796–3801.

[188] Dkhil, S. B.; Duché, D.; Gaceur, M.; Thakur, A. K.; Aboura, F. B.; Escoubas, L.; Simon, J.-J.; Guerrero, A.; Bisquert, J.; Garcia-Belmonte, G.; Bao, Q.; Fahlman, M.; Videlot-Ackermann, C.; Margeat, O.; Ackermann, J.

Interplay of Optical, Morphological, and Electronic Effects of ZnO Optical Spacers in Highly Efficient Polymer Solar Cells. *Advanced Energy Materials* **2014**, *4*, 1400805.

[189] Schueppel, R.; Timmreck, R.; Allinger, N.; Mueller, T.; Furno, M.; Uhrich, C.; Leo, K.; Riede, M. Controlled current matching in small molecule organic tandem solar cells using doped spacer layers. *Journal of Applied Physics* **2010**, *107*, 044503.

[190] Burkhard, G. F.; Hoke, E. T.; McGehee, M. D. Accounting for Interference, Scattering, and Electrode Absorption to Make Accurate Internal Quantum Efficiency Measurements in Organic and Other Thin Solar Cells. *Advanced Materials* **2010**, *22*, 3293–3297.

[191] Reese, M. O. et al. Consensus stability testing protocols for organic photovoltaic materials and devices. *Solar Energy Materials and Solar Cells* **2011**, *95*, 1253–1267.

[192] Chang, J.; Kuga, Y.; Mora-Seró, I.; Toyoda, T.; Ogomi, Y.; Hayase, S.; Bisquert, J.; Shen, Q. High reduction of interfacial charge recombination in colloidal quantum dot solar cells by metal oxide surface passivation. *Nanoscale* **2015**, *7*, 5446–5456.

[193] Liu, H.; Pourret, A.; Guyot-Sionnest, P. Mott and Efros-Shklovskii variable range hopping in CdSe quantum dots films. *ACS Nano* **2010**, *4*, 5211–5216.

[194] Xu, F.; Benavides, J.; Ma, X.; Cloutier, S. G. Interconnected TiO_2 Nanowire Networks for PbS Quantum Dot Solar Cell Applications. *Journal of Nanotechnology* **2012**, *2012*, 1–6.

[195] Azmi, R.; Sinaga, S.; Aqoma, H.; Seo, G.; Ahn, T. K.; Park, M.; Ju, S.-Y.; Lee, J.-W.; Kim, T.-W.; Oh, S.-H.; Jang, S.-Y. Highly efficient air-stable colloidal

quantum dot solar cells by improved surface trap passivation. *Nano Energy* **2017**, *39*, 86–94.

[196] Wang, Y. et al. In Situ Passivation for Efficient PbS Quantum Dot Solar Cells by Precursor Engineering. *Advanced Materials* **2018**, *30*, 1704871.

[197] Wang, X.; Chen, Y. P.; Nolte, D. D. Strong anomalous optical dispersion of graphene: complex refractive index measured by Picometrology. *Optics Express* **2008**, *16*, 22105–20112.

[198] Johnson, P. B.; Christy, R. W. Optical constants of the noble metals. *Physical Review B* **1972**, *6*, 4370–4379.

[199] Li, P.; Xue, W. Selective deposition and alignment of single-walled carbon nanotubes assisted by dielectrophoresis: from thin films to individual nanotubes. *Nanoscale research letters* **2010**, *5*, 1072–8.

[200] Tsuda, K.; Sakka, Y. Simultaneous alignment and micropatterning of carbon nanotubes using modulated magnetic field. *Science and technology of advanced materials* **2009**, *10*, 014603.

[201] Tanaka, S.; Mielczarek, K.; Ovalle-Robles, R.; Wang, B.; Hsu, D.; Zakhidov, A. A. Monolithic parallel tandem organic photovoltaic cell with transparent carbon nanotube interlayer. *Applied Physics Letters* **2009**, *94*, 113506.

[202] Araújo, A.; Barros, R.; Mateus, T.; Gaspar, D.; Neves, N.; Vicente, A.; Filonovich, S. A.; Barquinha, P.; Fortunato, E.; Ferraria, A. M.; Botelho do Rego, A. M.; Bicho, A.; Águas, H.; Martins, R. Role of a disperse carbon interlayer on the performances of tandem a-Si solar cells. *Science and technology of advanced materials* **2013**, *14*, 045009.